8-2018

Formation Studies of Ca12Al14O33

John Robert Salasin
University of Tennessee, jsalasin@vols.utk.edu

To the Graduate Council:

I am submitting herewith a dissertation written by John Robert Salasin entitled "Formation Studies of $Ca_{12}Al_{14}O_{33}$." I have examined the final electronic copy of this dissertation for form and content and recommend that it be accepted in partial fulfillment of the requirements for the degree of Doctor of Philosophy, with a major in Materials Science and Engineering.

Claudia J. Rawn, Major Professor

We have read this dissertation and recommend its acceptance:

Brett G. Compton, David J. Keffer, David G. Mandrus, Kurt E. Sickafus

Accepted for the Council:

Dixie L. Thompson

Vice Provost and Dean of the Graduate School

(Original signatures are on file with official student records.)

Formation Studies of $Ca_{12}Al_{14}O_{33}$

A Dissertation Presented for the
Doctor of Philosophy
Degree
The University of Tennessee, Knoxville

John Robert Salasin
August 2018

DEDICATION

I dedicate this to my love and Elizabeth Ann whose support and friendship these last four years have kept me focused and motivated. I look forward to the future we create together.

ACKNOWLEDGEMENTS

I would like to acknowledge:

My fiancé Elizabeth Ann for supporting me and taking the burden of my stress when the sunshine goes away and rough times rear their head. It was fate crossing paths when we did. The relationship and friendship we developed during this chapter of my life is a foundation which I cannot wait to build upon for the duration of our book. It takes two to tango; thank you for being my partner.

My parents and sisters for encouraging me to ask the question why and supporting my pursuit and passion for the unknown. Without this support from the very beginning, completing a bachelors, masters, and PhD in eight years would have been an uphill battle.

My new Floyd/DiStephano family for being my family away from home and entertaining my high level scientific discussions when I needed a soundboard. The distraction you provided from the day to day stress allowed for the development of my creative process and ultimate success.

My coworkers and fellow doctoral students who accompanied me on this journey and provided a wonderful outlet for mutual complaining, collaboration, and escape. More specifically Curt and Alex who have been a part of this journey from our first days in qualifier classes and proved instrumental in reaching candidacy.

Dr. David Keffer for his eagerness to jump in with both feet to define and brighten the light at the end of the tunnel. Your fingerprints are all over my development. Your selflessness and passion for teaching and learning is an inspiration.

Dr. Claudia Rawn for advising me and supporting me as I forged a new path forward into unfamiliar and new techniques and science. I understand and appreciate how lucky I was to have the full support and freedom you provided me. Without this and the other non-degree opportunities you provided me I would not have developed into the researcher that I am.

To those I most definitely unintentionally excluded; Thank you.

ABSTRACT

$Ca_{12}Al_{14}O_{33}$, also known as mayenite or C12A7, is a functional material with many applications; most uniquely is the ability to form a conductive oxide. The performance of the material is altered with the addition of dopants, both cationic and anionic, as well as with the control of sample microstructure. Obtaining further performance increases requires a robust, rapid, and low temperature synthesis method for doped C12A7, an understanding of the kinetics of formation to control microstructure, and development of direct electronic material synthesis method.

Conventional synthesis of ceramic materials follows the solid-state synthesis method which homogenizes a heterogenous mixture of reactants with high temperatures and long process times. Sol-gel synthesis methods utilizing atomically homogenous reactants lead to a decrease in process time and temperature yielding a controllable microstructure. A polymer assisted sol-gel method is developed which overcomes chemical constraints of the amorphous citrate sol-gel method and allows for robust, rapid, and low-temperature synthesis for large cationic systems.

Elucidation of the kinetics behind12A7 synthesis and formation traditionally adopts a thermodynamic approach that characterizes the end-point and provides little understanding of the journey to that thermodynamic equilibrium. In-situ X-ray diffraction is employed to study the kinetics of formation as a function of reactant homogeneity and atmosphere to elucidate the kinetic pathways in real time. The polymer-assisted reactants lead to a 30% decrease in formation temperature, order of magnitude reduction in formation time, and two orders of magnitude reduction in grain size.

The current process to form electrically conducting C12A7 requires the synthesis, consolidation, and then reduction of oxy-C12A7. This consists of multiple long duration high temperature processing steps prohibiting microstructural control. Herein a direct electride synthesis technique is developed and a theory behind the kinetics of formation is presented. Consolidated semi-conducting C12A7 is directly synthesized in under 12 h with room for process refinement to further reduce this time.

The refinement of a robust homogenous reactant synthesis method, elucidation of the kinetic pathways of formation, and the development of a direct electride synthesis method allows for the formation of doped C12A7 electronic materials with a controlled microstructure leading to an increase in performance of a functional material with nearly endless applications.

TABLE OF CONTENTS

LIST OF TABLES

LIST OF FIGURES

INTRODUCTION

The rise of the information age and smart technology has brought the application and need for high technology materials into every home, car, and pocket. A drive to understand and improve bulk property characteristics has led the collective materials science and engineering field to characterize and engineer materials not only on the continuum bulk scale, but also on the micrometer (10^{-6} m), nanometer (10^{-9}), and atomic scale (10^{-10} m). Understanding the atomic structure, microstructure, and physical property relationships and characterizing these relationships as function of processing parameters and chemical composition allows improvements in functionality and additional applications.

The compositional space for $Ca_{12}Al_{14}O_{33}$ (C12A7) cationic doping is large and to date the research into cation-doped C12A7 has been focused on the insulating stoichiometric, oxy-C12A7, compound and not the electrically conductive, electride-C12A7, compound. This is surprising since cationic dopants are predicted to lead to changes in both the electronic and atomic structure; This scientific void is tied to the barrier of entry in creating electride-C12A7 materials [1]. Conventional electride formation starts with synthesis of the oxy-C12A7 after which the powder is consolidated into a dense form such as a single crystal or thin film to probe the electronic structure. This consolidated product is then put through a reduction process to convert it to the conductive oxide, electride-C12A7. This multi-step process requires characterization, analysis, expertise, and process refinement at all processing steps. Development of a reliable one-step synthesis, consolidation, and reduction process to obtain the electride-C12A7 can drastically reduce the time and variables present in the current electride formation methods. This direct synthesis would allow for high throughput of doped electride-C12A7 materials for characterization of structure property relationships. The focus of this dissertation seeks to demonstrate a direct electride synthesis method through the carbonaceous reduction process from standard C12A7 reactants in both solid state and wet-chemistry synthesis techniques; this requires engineering of synthesis routes, revealing the kinetics of C12A7 phase formation, and developing an understanding of the basic principles behind the carbonaceous reduction process.

The standard process to obtain a C12A7 electride starts with synthesis of the stoichiometric compound through traditional solid-state synthesis (SSS) or sol-gel wet chemistry techniques. The former process involves temperatures above 1200 °C and processing times up to 24 h. SSS has the advantage of throughput scalability and historical bias, but has fundamental issues insuring a homogeneous distribution of dopants, controlling powder morphology, and low conformability to diverse cationic landscape. These intrinsic limitations can be overcome through the application of wet chemistry techniques that utilizes atomic level homogeneity to eliminate irregular distribution of dopants and reduce diffusion pathways leading to rapid formation of the desired phase. The level of complexity does increase as the number of cations increases, and chemical engineering and process refinement is necessary for each cationic system. Conventionally the amorphous citrate sol-gel process is utilized, but

significant process engineering is required whenever the cationic system is changed. This investigation details the proper steps to take to ensure the final product from the amorphous citrate technique is the desired doped phase, but goes further in developing a novel C12A7 polymeric sol-gel synthesis route with polyvinyl alcohol. This polymer assisted sol-gel method leads to a cationically homogenous precursor with low carbonaceous residue and a low organic to cation mass ratio; the desired final phase formation is robust to synthesis variables allowing for easy expansion to other cationic systems and black box use by researchers who do not wish to investigation solution chemistry.

The next section of this investigation deals with the kinetic investigation in the formation of C12A7. The C12A7 systems has been previously characterized by thermodynamic investigations. Thermodynamic studies probe the thermodynamic phase equilibria and elucidate the final lowest energy state destination but are void of information about kinetic pathways to that lowest energy state. In-situ non-ambient high-temperature X-ray diffraction (HTXRD) allows for the rapid probing of phase formations and atomic details during heating to characterize the pathways to the thermodynamic equilibrium. The direct synthesis of C12A7 must occur in a non-oxidizing environment and there is a lack of investigations, both thermodynamic and kinetic, focused on non-oxidizing environments. In this investigation the kinetic pathways and thermodynamic equilibrium are characterized as a function of reactant homogeneity and process atmosphere. These studies show a deviation from the pathways predicted by thermodynamic studies and define a new understanding that atmospheric anions are not necessary for C12A7 phase formation; For the first time electride-C12A7 formation has been observed in a vacuum environment.

With a development of reactant mixtures and characterization of kinetic formation pathways the groundwork for understanding and developing a direct synthesis method through the carbonaceous reduction process is set. First, a characterization of the carbonaceous reduction processes ability to convert as-synthesized oxy-C12A7 to electride-C12A7 is conducted. A structural investigation into how the oxy-C12A7 structure converts to the electride-C12A7 structure as a function of process duration yields insight into the mechanisms responsible for conversion. Structural investigation and characterization of the end products reveals that the process is dependent on carbonaceous species and successful conversion of oxy-C12A7 to a semi-conducting electride-C12A7 occurs through recrystallization of decomposed C12A7 products. The process of synthesizing oxy-C12A7, processing it so it decomposes, and then reforming the C12A7 structure is circular and demonstrates the possibility for direct electride synthesis. Direct synthesis studies are conducted utilizing a low homogeneous SSS reactant mixture and a high homogeneous polymer assisted sol-gel reactant. Electride-C12A7 formation was observed in both cases with the formation of C12A7 occurring at a faster rate with the polymer assisted reactants; this is the first demonstration of direct electride synthesis from solid state and polymer assisted reactants and a new theory for electride conversion is presented.

Through the development of a robust sol-gel synthesis technique, characterization of the kinetic formation of C12A7, and elucidation of the processes underlying the carbonaceous reduction process a direct electride synthesis has been demonstrated for heterogenous and homogenous reactants. This process allows for a substantial reduction in time and application knowledge to synthesize a consolidated electride material, thereby, lowering the barrier of entry to studying doped electride-C12A7. Characterization of the doped compounds will lead to a better understanding of the electronic properties tunability for application. Doped electride-C12A7 is a vast and uninvestigated compositional space which this research has developed a foundation for future scientific studies. Building on this foundation, engineering at the atomic and microstructure levels to improve material functionality, properties, and application of electride C12A7 can commence.

This is a multi-part dissertation with four main chapters:

Chapter 1 The first chapter is a comprehensive review of the electride C12A7 phase space. The review thoroughly documents the electride C12A7 structure-electronic property relationships, electride formation principles and techniques, and the C12A7 dopant phase space from almost 200 published journal articles.

Chapter 2 The second chapter discusses the fundamentals to solid state synthesis and wet chemistry synthesis. The proper implementation of the amorphous citrate sol-gel route is presented as a reference for future use of this method, but a polymer assisted sol-gel route is developed to replace the amorphous citrate process due to the robustness and lack of chemical engineering needed to ensure desired final product.

Chapter 3 The third chapter characterizes the kinetic formation pathways of C12A7 as a function of reactant homogeneity and process atmosphere. The investigation replaces the theories of kinetic pathways developed by thermodynamic studies and demonstrates, for the first time, the formation of C12A7 in a carbonless vacuum environment.

Chapter 4 The fourth, and final chapter, culminates the project by developing a new theory for the carbonaceous reduction process. Direct electride synthesis is observed for the first time from solid state and polymer assisted reactants through the carbonaceous process and a new theory on the formation of the electride is presented.

CHAPTER 1
Comprehensive Review on the Electride Structure property Relationships, electride Formation Processes, and Doping of C12A7

A version of this chapter was originally published by John Robert Salasin and Dr. Claudia Rawn:

Salasin, J. R., & Rawn, C. J. (2017). Structure Property Relationships and Cationic Doping in [Ca24Al28O64]4+ Framework: A Review. *Crystals*, *7*(143), 1–25. http://doi.org/10.3390/cryst7050143

Changes to the conclusion have been made; the rest is unchanged. John Robert Salasin performed the experiments; John Robert Salasin and Claudia Rawn analyzed the data; and John Robert Salasin and Claudia Rawn wrote the paper.

1.1 Abstract

$Ca_{12}Al_{14}O_{33}$ (C12A7, 12CaO·7Al2O3, or $[Ca_{12}Al_{14}O_{32}]^{2+}:O^{2-}$) is a material with a clathrate cage framework, positively charged and stabilized by anions occluded within 17% of the cages. The occluded anion is modular and can be elemental, polyatomic, and electronic in nature. This review focuses on the electride C12A7 ($[Ca_{24}Al_{28}O_{64}]^{4+}:(4*\partial)e^{-}(2-\partial)O^{2-}$), where O^{2-} anions are replaced with electrons, and compliments previous structural and electronic property reviews to illuminate the structure–property relationships. Electride formation is updated with new findings in carbonaceous reduction methods. Most importantly, an extensive compilation of cationic doped C12A7 isostructural compounds is presented as motivation to study doped C12A7 electrides. Cationic dopants have profound impacts on the electronic properties due to changes in the density of states, localized electron behavior, and structural distortions.

1.2 Introduction

$Ca_{12}Al_{14}O_{33}$ (C12A7), the mineral mayenite, appears in early cement literature and is the first inorganic electride stable at room temperature. C12A7 crystallizes in the cubic space group $I\bar{4}3d\ (no.220)$, with Z (formula units) = 2 and a lattice parameter ~12 Å. The unit cell contains 118 atoms and two of the O^{2-} atoms, in the stoichiometric case, nucleate a clathrate cage consisting of tetrahedrally coordinated trivalent Al and octahedrally coordinated divalent Ca cations. The unit cell contains 12 interconnected cages each with a diameter of ~5 Å [2–4]. The clathrate cage framework $[Ca_{24}Al_{28}O_{64}]^{4+}$ has a net positive charge balanced by anions occluded in the interior of the cage. In the stoichiometric case, $[Ca_{24}Al_{28}O_{64}]^{4+}:2O^{2-}$, O^{2-} is the template ion responsible for nucleating the framework. The bonding between the framework and the occluded anions leads to a contraction of the cage, introducing structural disorder (Figure 1), which is discussed later.

The C12A7 framework is stabilized with a range of host of oxyanions: O^{2-} [5,6], OH^- [2,7–10], O^- [9,11–15], O_2^- [9,11–17], O_2^{2-} [9,15,17,18] as well as H^- [19–22], F^- [5,9,10,23–25], Cl^- [5,10,23,26], CN^- [10,27,28], S^{2-} [5,10], N^{3-} [10,29], NO_2^- [28], C_2^{2-} [3,30–32], NH_2^- [29,33], hydrazine [28] and Au^- [34]. The interconnectivity of the cages allows high ionic diffusion. Research in the last decade has been heavily focused on the ability for electrons to migrate into the cage framework to satisfy the electrostatic imbalances resulting from anion vacancies, $[Ca_{24}Al_{28}O_{64}]^{4+}:(4*\partial)e^-(2-\partial)O^{2-}$. As stabilizing anions are removed, electrons migrate into the cages where, when $\partial < 1$, they have a 1s like nature similar to Farbe color centers, leading to the F^+-like notation used in the literature for metal salts and oxides [1,35]. The ability for these electrons to remain in the cages at room temperature results in $[Ca_{24}Al_{28}O_{64}]^{4+}:(4*\partial)e^-(2-\partial)O^{2-}$ being the first room temperature inorganic electride.

Dye from Michigan State University has pioneered the synthesis of crystalline organic electrides and defines an electride as "…a stoichiometric ionic crystal in which electrons are trapped in cavities and serve as the counter anions to an equal number of positive charges in a regular crystalline lattice [36]." The electrons are delocalized from their parent atoms and migrate through the positive crystalline frameworks to ensure charge neutrality. This idea of quantum confinement is not new and the reports of localized electrons, e.g., alkali ammonia solutions, ionic solids, and Farbe color centers, predate the 20th century [36]. Dye's group has successfully synthesized many crystalline organic electrides, where the majority contain cavities 4–6 Å in diameter with 7–9 Å between cage centers [36]. Hosono et al. discovered C12A7 as the first inorganic structure to meet the formal definition of an electride defined by Dye and C12A7 draws similar parallels to the organic structures from the size of the crystalline voids to the observed character of the localized electron [37]. Hosono's group has since discovered the inorganic electrides including $Ca_2N:e^-$ and $Y_2C:2e^-$ and used crystal structure databases and ab initio calculations to find the first magnetic electrides at ambient temperatures [38–40]. The development of stable electrides with a low work function leads to possible applications in electron emission applications, n-doped electronic applications, and catalysis and reduction processes [36,41].

C12A7 research has prompted reviews spanning thermodynamics and synthesis [42], single crystal and thin film growth and the associated electrical properties [3,43], structural disorder and compositional analogs based on the mineral mayenite supergroup [44], and applications in display devices [45]. The goal of this review is to consolidate the structure–physical property relationships, illuminate discrepancies due to the complicated nature of the compound, suggest areas for future research, and investigate the effects of cation doping into the C12A7 clathrate cage framework.

1.3 Electride Structure-Physical Property Relationships

As the O^{2-} anions are removed in $[Ca_{24}Al_{28}O_{64}]^{4+}:(4*\partial)e^-(2-\partial)O^{2-}$, the cage framework remains with electrons injected into the center of the cage to ensure charge

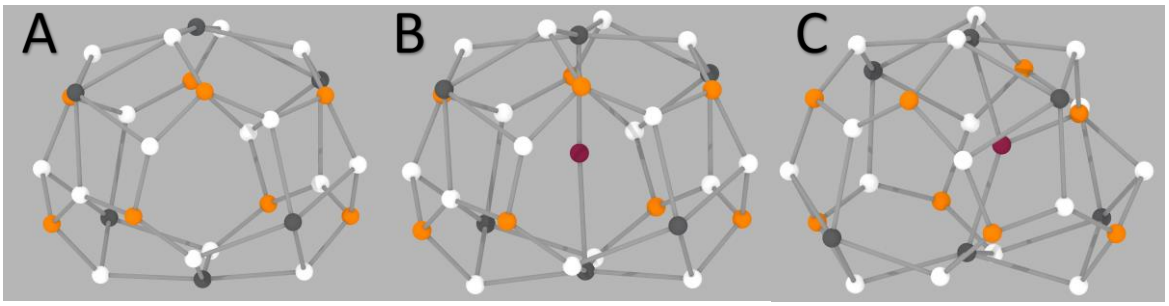

Figure 1 Three main cage types in $[Ca_{24}Al_{28}O_{64}]^{4+}$ framework where Ca atoms are gray, Al atoms are orange, O atoms are white, and the occluded anion is maroon: (A) the unoccupied cage showing no distortion; (B) the 12a occupied cage observed in OH^- and e^- occupied cages showing distortion in the axial, S_4 ,direction; and (C) the 48e off center O^{2-} occupied cage showing a destruction of the framework due to bonding between the framework Ca and Al and the occluded anion.

neutrality. The electron is trapped in a potential well created by the positively charged framework, similar to a particle in a box, and exhibits interactions with framework cations [1,4]. When all anions are removed ($\partial = 2$), the theoretical maximum electron concentration is 2.33×10^{21} cm^{-3} [1]. As ∂ is increased, changes in physical properties are tied to the nature of injected electrons and the resulting structure of the cage framework. This discussion is segmented into three parts; A discussion on insulating stoichiometric C12A7 ($\partial = 0$), semiconducting low and medium electron concentration ($\partial < 1$), and metallic conducting high electron concentration ($\partial > 1$).

1.3.1 Insulating Stoichiometric ($\partial = 0$)

To fully reveal the atomic structure and the resulting electrical properties as electron concentration increases, neutron and synchrotron x-ray diffraction studies are vital to characterize the underlying crystallographic changes. An accurate model of the starting stoichiometric structure is needed to fully appreciate the transition to an electride structure. Several groups, including Palacios et al. and Sakakura et al., started with the stoichiometric system with the intention to move towards the electride system with varying degrees of electron concentration [46–48]. An in-depth historical synopsis and $[Ca_{24}Al_{28}O_{64}]^{4+}:2O^{2-}$ analysis is summarized by Gfellar in his review of mayenite as both a synthetic oxide and mineral [44].

$[Ca_{24}Al_{28}O_{64}]^{4+}:2O^{2-}$ is a highly disordered crystal structure. Synchrotron single-crystal x-ray diffraction (SSXRD) conducted by Palacios et al. and Sakakura et al. revealed that the structure of the cage framework ($[Ca_{24}Al_{28}O_{64}]^{4+}$) is a superposition of three cage types; unoccupied, occupied, and adjacent to an occupied cage [46–48]. The disorder arises from the presence of occluded anions needed to nucleate the cage framework. In O^{2-} occupied cages, the occluded anion is located at an off center 48e special position and is bonded with two framework Ca and a single framework Al. This

leads to contraction of the cage due to bonding between the framework Ca cations and occluded anions. Crystallographically, the contraction moves the Ca cations towards the center from one 24d site, Ca1, to two equally partially occupied 24d sites denoted Ca1a and Ca1b. Studies by Sakakura et al. suggest that the Ca1a site is moved slightly off the S_4 axis to a 48e site. These two sites arise due to the symmetry of the cage and are needed for similar bond lengths between Ca1a/Ca1b and the occluded anion O3 [46,47]. This trimodal split Ca position was previously reported by Nomura et al., however, no split Al position was reported, possibly due to correlating refinement parameters with the site occupancy factor resulting in large uncertainties, especially when the occupation is small [49]. Bonding between Al1-O3 leads to a new Al position, Al1a, causing a destruction of a framework tetrahedron due to a breaking of the framework Al1-O1 bond in favor of the Al1a-O3 bond Figure 2 [46]. This results in a relaxation of the local structure around this framework tetrahedron and new split positions of both O1 and O2 sites. Further local disorder becomes apparent in adjacent cages where the loss of the attractive force of the Al1 atom results in a distortion of the Ca1 site to 48e Ca1c site resulting in the third cage type adjacent to the occupied cages [46]. For a complete listing of crystallographic information, see Table 1 reproduced with modification from Gfellar [44].

One discrepancy between the two reports of Palacios et al. and Sakakura et al. concerns another occluded anion position on a 12a site directly at the center of the cage [46,47]. $[\mathrm{Ca_{24}Al_{28}O_{64}}]^{4+}:2\mathrm{O}^{2-}$ is known to be hygroscopic at ambient humidity [7,23]. In his review Gfellar hypothesized, and both Boysen et al. and Palacios et al. previously hinted, that the presence of the 12a occluded site density was due to a hydrolysis reaction between the occluded O and moisture in the atmosphere leading to the reaction $\mathrm{O^{2-}_{(Cage)}} + \mathrm{H_2O_{(g)}} \rightarrow 2\mathrm{OH^-_{(cage)}}$ [2,44,47]. Ensuing hydration and diffraction experiments found that stoichiometric samples, when exposed to an atmosphere with a high moisture content, led to a reduction in occupation of the 48e O3 special position in favor of occupation of the center of the cage 12a site [44]. This 12a site was previously experimentally reported by Boysen et al. in samples with larger than the stoichiometric expected occluded anion occupancy, $[\mathrm{Ca_{24}Al_{28}O_{64}}]^{4+}:2\mathrm{OH^-O^{2-}}$, and by Nomura et al. [49]. ith monovalent occluded species, an increase in occupied cages is expected to be driven by the need to charge balance the positive framework. Upon heating, older reports cite hydroxides (1.3–1.4 wt %) remain in the C12A7 structure up to 1100 °C, however, structural studies by Boysen et al. suggests that at 700 °C the occupation of the 12*a* site disappears [2,23]. This is consistent with an irreversible loss of the weakly bonded hydroxide. Both the Ca1b and Ca1a sites are present when bonding to O^{2-} but when most other species occupy the cages only the Ca1a site is present due to the location of anions at the 12*a*, center of the cage, site. Further structural studies of anion substitutions showed that this 12*a* site is favored by a large number of possible anions that do not have an affinity towards the framework Al, leading to the off center 48*e* site [50]. The 12*a* site, along with its hygroscopic nature, further complicates the disorder in the non-stoichiometric $[\mathrm{Ca_{24}Al_{28}O_{64}}]^{4+}$ framework leading to an additional cage type,12*a*

Table 1 Comparison of structural models for disordered $I\bar{4}3d$ $[Ca_{24}Al_{28}O_{64}]^{4+}:2O^{2-}$. Reproduced with modifications from [44]. Occupancies are reported based on the occupancy of the off center and center anion positions to allow for modular structural occupancies based on the degree of OH^- and O^{2-} content.

Name [Occup.]	Wycoff Site		Boysen [2]	Nomura [49]	Palacios [47]	Sakakura [46]
Ca1	24d	*x*	0.1432 (3)	0.1401 (7)	0.13831 (2)	0.13933 (2)
[1 − (X + 4Y)]		*y*	0	0	0	0
		z	0.25	0.25	0.25	0.25
Ca1a	24d	*x*	0.1867	0.1771 (5)	0.17451	-
[X + 2Y]		*y*	0	0	0	-
		z	0.25	0.25	0.25	-
Ca1a	48e	*x*	-	-	-	0.1693 (2)
		y	-	-	-	0.0067 (3)
		z	-	-	-	0.2503 (3)
Ca1b	24d	*x*	-	0.1977 (5)	0.2065	0.2069 (1)
[2Y]		*y*	-	0	0	0
		z	-	0.25	0.25	0.25
Ca1c	48e	*x*	-	-	-	0.1353 (2)
[Y]		*y*	-	-	-	0.0043 (3)
		z	-	-	-	0.2354 (2)
Al1 [1 − 3Y]	16c	*x*	0.0188 (1)	0.0189	0.01867 (2)	0.01861 (9)
Al1a	48e	*x*	-	-	0.30520 (9)	0.3041 (2)
[Y]		*y*	-	-	0.19510 (9)	0.1984 (2)
		z	-	-	0.26090 (9)	0.2619 (2)
Al2	12b	*x*	0.875	0.8750	0.875	0.875
[1]		*y*	0	0	0	0
		z	0.25	0.25	0.25	0.25
O1	48e	*x*	0.0367 (1)	0.0381 (1)	0.03612 (4)	0.03605 (4)
[1 − 2Y]		*y*	0.4429 (1)	0.44290 (8)	0.44231 (4)	0.44234 (3)
		z	0.15054 (9)	0.1510 (1)	0.15049 (4)	0.15052 (3)
O1a	48e	*x*	-	-	-	0.1302 (3)
[Y]		*y*	-	-	-	0.0603 (3)
		z	-	-	-	0.4328 (3)
O1b	48e	*x*	-	-	-	0.1718 (5)
[Y]		*y*	-	-	-	0.0312 (4)
		z	-	-	-	0.4352 (5)
O2 [1 − 3Y]	16c	*x*	0.18519(9)	0.1865(1)	0.18526(3)	0.18510 (4)
O2a	48e	*x*	-	-	-	0.1996 (6)
[Y]		*y*	-	-	-	0.1750 (7)
		z	-	-	-	0.1893 (6)
O3	12a	*x*	0.375	0.375	0.375	-
(center)		*y*	0	0	0	-
[X]		*z*	0.25	0.25	0.25	-
O3	48e	*x*	-	0.344 (2)	0.3588 (2)	0.3559 (6)
(off cen.)		*y*	-	0.036 (2)	0.0616 (2)	0.0614 (7)
[Y]		*z*	-	0.243 (5)	0.2479 (2)	0.2506 (7)

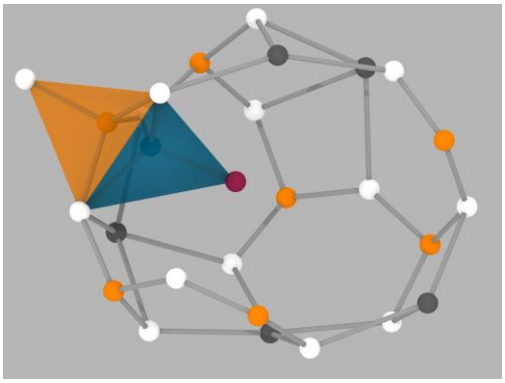

Figure 2 Destruction of framework tetrahedron (orange) due to bonding between occluded O^{2-}, maroon, and framework Al forming a new tetrahedron (blue) in $[Ca_{24}Al_{28}O_{64}]^{4+}:2O^{2-}$. The front of the cage has been removed for clarity.

occupied cages. Electron paramagnetic resonance (EPR) has been used for probing the concentration of extra framework paramagnetic species in C12A7 [12,15,37].

The structural disorder in the stoichiometric case results in a complicated band structure calculated through density functional theory (DFT). Theoretical calculations of the band structure corresponding to $[Ca_{24}Al_{28}O_{64}]^{4+}:(4*\partial)e^{-}(2-\partial)O^{2-}$ with various levels of ∂ have proven difficult due to the conversion of the system from an insulating to a metallic state, however, similar trends are observed from a variety of different functionals [1,4,51,52]. Sushko et al. performed band structure calculations from the stoichiometric insulating state to the electride state using two different density functionals; B3LYP works well with insulating systems and LDA works well with metallic systems [4]. $[Ca_{24}Al_{28}O_{64}]^{4+}:2O^{2-}$ has a large bandgap, E_g = 6–7 eV, making it electrically insulating. Many interstitial electronic states reside in the band gap (Figure 3a), and form two general groups, 1–2 eV above the valence band (VB) and 0.5–2 eV below the conduction band. The grouping of ten states below the conduction band corresponds to the ten unoccupied cages, deemed the cage conduction band (CCB). The presence of this conduction band makes C12A7 a system where two conduction bands are observed; the states associated with framework cations and those corresponding to the cage potential well. The states above the valence band correspond to two different features. The eight states between −4.0 and −5.0 eV correspond to O 2p states split off from the valence band due to disorder associated with the bonding between framework Al and occluded O^{2-}; this is due to the presence the presence of oxygen splits positions in the 48e occupied cage type. The two states above −4.0 eV correspond to O^{2-} occupied CCB states [4]. The contraction of the cage due to interactions with occluded species move occupied CCB states to lower energies. Other band structure calculations only exhibit the two occupied CCB states near the valence band. Sushko et al. reported that if the off-center O^{2-} position was discarded in favor of a metastable center of the cage position, historically reported in diffraction

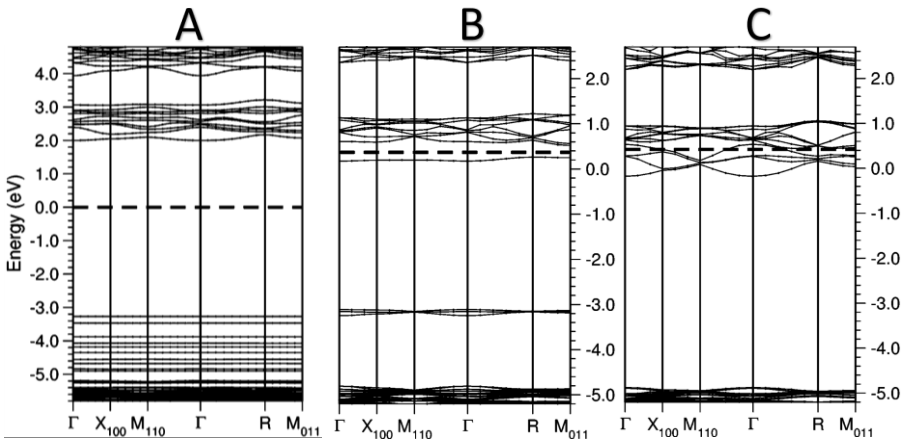

Figure 3 Band structure of: (a) $[\mathbf{Ca_{24}Al_{28}O_{64}}]^{\mathbf{4+}}:\mathbf{2O^{2-}}$; (b) partially reduced $[\mathbf{Ca_{24}Al_{28}O_{64}}]^{\mathbf{4+}}:(\boldsymbol{\alpha})\mathbf{e^{-}}(\mathbf{4}-\boldsymbol{\alpha})\mathbf{H^{-}}$; and (c) fully reduced $[\mathbf{Ca_{24}Al_{28}O_{64}}]^{\mathbf{4+}}:\mathbf{4e^{-}}$ calculated using B3LYP and LDA functionals. "3 × 3 × 3 k mesh was used in both cases, the Fermi level is shown as a thick dash line, and only spin up states are shown." Adapted with permission from [4]. Copyright 2007 American Chemical Society.

studies, the 2p states associated with the framework did not split from the valence band and only two bands, corresponding to the two O^{2-} occupied cages, are observed [4]. This is understandable, without the off-center O^{2-} position there will be higher homogeneity in the O's contained in the framework. These 12 states of the CCB account for all 12, unoccupied and occupied, cages in the unit cell of C12A7, and the structure of the cage correlates to the energy of these states giving rise to the interesting electrical properties.

Due to the large band gap, C12A7 single crystals exhibit >90% optical transparency in the visible range, and at low electron concentration C12A7 combines optical transparency with electrical conductivity leading to potential applications as a transparent conductive oxide that is both inexpensive and earth abundant [53–55].

1.3.2 Semiconducting Low/Medium Electron Concentration $(\boldsymbol{\partial < 1},\ \boldsymbol{n_e < 1\times 10^{21}})$

At low and medium electron concentration, C12A7 transfers into a semiconducting state. The introduction of electrons into the cages results in a color change from clear to green, which is characteristic of F^{+} centers.

The structure is now more disordered with a new electron occupied cage type in addition to the previous cage types. Palacios et al. performed SSXRD looking at low electron loadings and determined that, as electron loading increased from $[Ca_{24}Al_{28}O_{64}]^{4+}:0.6e^{-}1.7O^{2-}$ to $[Ca_{24}Al_{28}O_{64}]^{4+}:1.8e^{-}1.1O^{2-}$, the lattice parameter increased by 0.05% and 0.21%, respectively [47,48]. This is consistent with the relaxation of the occupied cage type toward an unoccupied cage type due to weakened interaction between the localized electron and the framework. A decrease in both the Ca1a and Ca1b site occupancies with increased electron loading further substantiates this theory.

It was reported that there was a small increase in the Ca1a-Ca1b (occupied cage diameter) while Ca1-Ca1 (unoccupied cage diameter) did not change [47]. The occupied cage diameter is contracted with respect to the unoccupied cage diameter due to the bonding between framework Ca and the O^{2-}. As the occupancy of O^{2-} is reduced, there should be no change in the bonding behavior leading to a relaxation in Ca1a/Ca1b positions. The observed change in contracted cage diameter could be attributed to the averaging of all the cage types. There are two likely possibilities; As the O3 and Ca1a/Ca1b occupancy decreases and the Ca1 occupancy increases, the refinement may be compromised due to difficulties distinguishing between the heavily correlated Ca1 and split positions, leading to inaccuracy in the atomic coordinates, and the second being a weak interaction between the localized electron and the framework Ca leading to a split Ca position in between Ca1 and Ca1a/Ca1b. As the electron occupied cage type increases in relevance the averaging of the split Ca position, corresponding to e^- occupied cages and Ca1a/Ca1b would lead to a larger contracted cage diameter. This evidence points to a contraction of the cage due to interaction with occluded electrons. Palacios et al. found that electron scattering density, at the 12a center of the cage position in reduced compositions, increased as electron loading increased [47]. This, experimentally, suggests that the electron is localized in the cage and the localized electron is located at the 12a center of the cage position as predicted by theoretical models [1,56]. However, since it is likely that the stoichiometric samples Palacios et al. studied were exposed to moisture, it is possible, since electron doping has not reached a maximum, that moisture caused the formation of hydroxide species leading to the observed electron density on the 12a position in reduced samples. The experimental observations from SSXRD are corroborated by band structure calculations.

Band structure calculations corresponding to low e^- occupation results in occupied CCB states 0.4–1 eV below the CCB and the small dispersion of this state indicates high localization of the electron [4]. It should be noted that these band structures were calculated through modeling of $[Ca_{24}Al_{28}O_{64}]^{4+}:(\alpha)e^-(4-\alpha)H^-$ and not $[Ca_{24}Al_{28}O_{64}]^{4+}:(4*\partial)e^-(2-\partial)O^{2-}$. This allows for calculations to be performed at lower electron concentration and both B3LYP and LDA functionals give similar band structures for the low electron loaded models. The calculated occupied cage diameter associated with the localized electron increases from 4.39 Å in O^{2-} occupied cages to 5.07 Å, which is, however, still significantly less than the unoccupied cage diameter of 5.6 Å. The average of these two cage diameters corroborates the diffraction observations associated with the expansion in average occupied cage diameter suggesting that localized electrons are polarons and induce cage framework contractions. This reduction in contracted cage diameter raises the energy of e^- occupied CCB states towards the unoccupied CCB, and the gap between the occupied and unoccupied CCB states gives rise to a semiconducting state [4].

The optical absorption spectra displays two peaks centered near 2.8 and 0.4 eV [30,57]. The absorption of these two peaks are assigned to the 1s to 2p excitation of a localized electron in a single cage, consistent with F^+ color centers, and to the transition

of localized electrons between cages, respectively [3,22,57]. Optical reflectance data show sharp phonon lines in the infrared regime as well as absorption in the visible and ultraviolet range typical of insulators. Limited Drude response is observed and contributions to the reflectance pattern can be fit with a Lorentzian model further indicating the dominate carrier type is localized opposed to free carriers [51,55]. Temperature dependent DC conductivity measurements when $\partial < 0.5$ reveal a temperature dependence of log(σ) of T^{-1} suggesting that at low concentrations the electrons conduct as polarons [37]. This indicates a strong lattice-electron coupling as previously observed in diffraction experiments and in DFT calculations and the activation energy (0.1 eV) and mobility (0.1 $cm^2 \cdot (Vs)^-$) are consistent with polaron theory [37,51,58]. As ∂ increases to 1, electrons form bipolarons due to neighboring cages being occupied, limiting polaron type conduction, and a change in the temperature dependence to $T^{-1/4}$ is consistent with thermally activated variable range hopping (VRH) conduction [3,37,51,59]. In the semiconducting state a room temperature electrical conductivity (σ_{RT}) below 100 $S \cdot cm^{-1}$ is obtained [3].

The presence of bipolarons is confirmed through analysis of EPR trends. Localized electrons act as F^+-like centers in a paramagnetic spin state [43]. This paramagnetic nature allows for the concentration of localized electrons to be determined by EPR. However, it was observed by Matsuishi et al. and corroborated by Kim et al. that the EPR signal saturates at approximately 8×10^{19} electrons [37,60]. This is only 1% of the theoretical maximum electron concentration and further statistical analysis determined that at peak electron loading there is a 99% chance of a neighboring cages being occupied. This suggests that, as electron concentration increases, neighboring electrons alter the paramagnetic state of the localized electron. Matsuishi et al. [37], further confirmed by Kim et al. [3], proposed that these neighboring electrons would form an EPR invisible bipolaron. Due to this fact, EPR should not be used to determine electron concentration unless ∂ is small, but can be used to identify the presence of F^+ paramagnetic centers characteristic of localized electrons at all levels of electron concentration.

1.3.3 Metallic High Electron Concentration $(\boldsymbol{\partial > 1,\ n_e > 1 \times 10^{21}})$

In the semiconducting state electrons are localized in the cages due to electron framework interactions leading to a large degree of inhomogeneity of cage types. As electron concentration increases past 1×10^{21} samples demonstrate a loss of optical transparency and a color change to black corresponding to absorption in the full visible range. DC conductivity measurements show a negative trend of log(σ) with respect to temperature, and metallic like conduction of approximately 1500 $S \cdot cm^{-1}$ with an increase in carrier mobility to 4.0 $cm^2 \cdot (Vs)^-$ is observed [59].

As electron concentration is increased, the degree of disorder associated with O^{2-} occupied cages is reduced due to the limited concentration of stabilizing anions. Kim et al. conducted synchrotron powder XRD (SPXRD) on $[Ca_{24}Al_{28}O_{64}]^{4+}: 4e^-$ and analyzed the data combining maximum entropy method (MEM) and Rietveld refinement

techniques. No split positions were reported for $[Ca_{24}Al_{28}O_{64}]^{4+}:4e^{-}$ and no electron scattering density was observed at the center of the cage, in contrast to reports in the semiconducting state by Palacios et al., suggesting a full relaxation of the contraction associated with electron occupied cages and loss of localized electrons which leads to a homogeneity among cage types [58].

Band structure calculations when $\partial = 2$, maximum electron concentration, show four occupied CCB states corresponding to the e^{-} occupied cages as well eight states corresponding to the unoccupied cages. B3LYP predicted a semiconducting system while LDA, displays no observable bandgap between the occupied CCB and unoccupied CCB [4]. A closer look reveals that one of the occupied CCB states is at a higher energy than the unoccupied CCB creating a metallic system matching the observed DC conductivity results. Further, a higher dispersion of these states suggests that an increase in carrier density leads to the formation of delocalized free carriers [4,58]. The calculated cage diameter of electron occupied cages has increased to ~5.4 Å, which is only slightly (~0.2 Å) smaller than the unoccupied cage diameter and explains why no split positions were observed in powder diffraction experiments.

Seebeck coefficient measurements reveal a decrease in Seebeck coefficient with increased carrier concentration and a change in sign concurrent with the transition from a semiconducting to a metallic state. This provides insight into the density of states (DOS) around the Fermi energy as electron concentration is increased indicating valleys in the DOS, confirmed through band structure calculations (Figure 4 (left)). The DOS around the lower CCB corresponds to Ca s-projected contribution and the higher CCB states have a Ca d-projected contribution [61]. With increased electron concentration, the occluded electrons that are initially localized is a s-like F^{+} state change to the sd-hybridized state of Ca (Figure 4 (right)). This hybridized state plays a role in the observed superconducting transition at ~0.2 K due to the increased ability for Cooper pairs to form [59,61].

Optical reflectance studies find that as electron concentration is increased a Drude peak and broadening of phonon peaks in the IR region, characteristic of free electron carriers, is observed in conjunction with the characteristic Lorentzian transitions associated with localized carriers [51,55]. The dominant conductivity type changes from VRH conduction to band conduction, but the Lorentzian features suggests both forms of conduction occur concurrently [51,55]. Lobo et al. identified an increase in asymmetry of phonon peaks with increased carrier concentration in the metallic regime [55]. This is characteristic of the Fano effect and indicates a large lattice-electron coupling. The observance of an increased Fano effect with carrier concentration confirms that localized and delocalized carriers are observed in the metallic state and the increase in carrier concentration favors the formation of polarons. There have only been EPR studies conducted just up to the metal transition, and paramagnetic electron species are still observed [37]. These experimental results along with the theoretical calculations point to the presence of localized and delocalized electrons existing in the C12A7 leading to concurrent and cooperative types of electrical conduction [43,53].

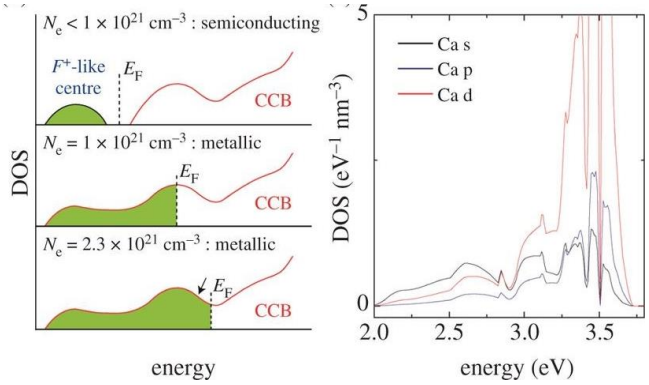

Figure 4 (left) Schematic illustration of DOS around the Fermi level as unoccupied and occupied CCB merge with increasing electron concentration. (right) Partial DOS of the CCB corresponding to the Ca s, d, and p DOS. Modified from Hosono et al. [61].

1.3.4 Summary

C12A7 exhibits an insulator to metal transition heavily correlated to structural changes. As anions are removed, and electrons are injected into the structure, the initial insulating disordered system relaxes to a less disordered metallic system due to a loss of off centered O^{2-} occupied cages. A weaker interaction between localized electrons, occupying the center of the cage, and framework Ca leads to a relaxation of the occupied cage diameter toward the unoccupied cage diameter resulting in an increase in homogeneity of the cages. This relaxation of the system is observed in theoretical band structure calculations and results in the occupied CCB states rising in energy until they overlap with the unoccupied CCB states leading to delocalization of electrons over all cages and metallic conduction. Electrical conductivity and optical reflectance measurements support the insulator to semiconductor to metallic conductor transition observed in band structure calculations. However, since the occupied cages do not fully relax back to the unoccupied state there is still some degree of electron localization. Structural, experimental, and theoretical studies conclusively point to the same trends in C12A7.

The diffraction studies by Kim et al. raise some important questions on the contraction of electron occupied cages. Does SPXRD have enough resolution to deconvolute the heavily correlated split positions and reveal small scattering due to localized electrons in the cage? There are inconsistencies between diffraction studies and possibly disagreement between diffraction studies and theoretical calculations in the metallic regime. Due to the hygroscopic nature of stoichiometric C12A7 it is important that all samples are handled consistently to avoid contamination. A systematic study across all electron concentrations, from insulating to metallic, with careful contamination control is needed to compliment physical property studies by Lobo et al. and Matsuishi et al. Neutron diffraction studies probe the nuclear density, making it invisible to the localized electrons, while synchrotron diffraction studies probe the

localized electrons and induced electrostatic distortions in electron clouds. Combined, they paint two different pictures of the same system and single crystal diffraction experiments at high electron concentration are needed.

Convoluted cooperative electronic conduction, observed at peak electron loading, is complicated. However, the current theory for the conversion from localized carrier to free carriers does not explain the increase in phonon electronic coupling observed through the Fano effect. While it may be related to the sd-hybridization proposed by Hosono et al. research to understand the behavior of polarons and free carrier conduction at peak electron loading can illuminate the mechanism behind the Fano effect observed by Lobo et al.

1.4 Electride Formation Processes

1.4.1 C12A7 Synthesis

C12A7 melts congruently and single crystals can be grown through many techniques including float zone (FZ), Czochralski (CZ), and melt forming techniques [3,47,57,62,63]. C12A7 is an intermediate compound in the CaO and Al_2O_3 binary system sandwiched between the two-phase regions consisting of C12A7 and either secondary phases denoted CA ($CaAl_2O_3$) and C3A ($Ca_3Al_2O_6$) (Figure 5). These two secondary phases are the formation products of C12A7 at higher temperatures (≥1200 °C),

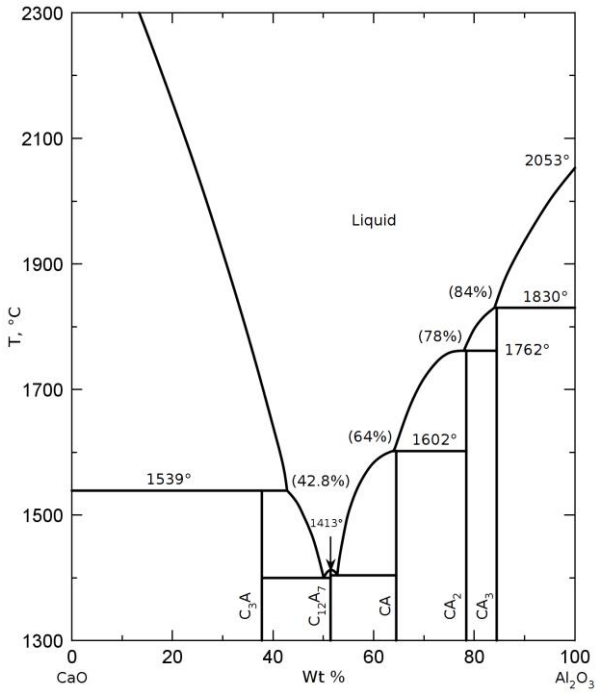

Figure 5 Binary CaO-Al2O3 phase diagram with Ca12Al14O33 at ~54 wt. % Al2O3 [64].

normally through solid-state synthesis, and decomposition products when no anions are present to stabilize the cage framework at high temperatures [65,66].

Wet chemistry processes can be used to synthesize C12A7 below 900 °C. It is suspected that the formation reaction proceeds through a secondary phase which is metastable, C5A3 ($Ca_5Al_6O_{14}$) [65–67]. There is a small stoichiometric difference between the C12A7 and C5A3, $9\ Ca_5Al_6O_{14} + Ca_3Al_2O_6 \rightarrow 2\ [Ca_{24}Al_{28}O_{64}]^{4+}: 2O^{2-}$. C5A3 consists of layered octahedrally coordinated Ca and tetrahedrally coordinated Al cations similar to the C12A7 cage framework (Figure 6). When the extra oxygen is available, it nucleates the clathrate cage framework. C5A3 and C3A are decomposition products, observed by Palacios et al. and our own investigations (discussed below), at 1100 °C under dry vacuum conditions [4,48].

Exploiting the affinity of weakly bonded occluded anions to form more stable bonds and high ionic diffusion afforded by the clathrate cage framework is the foundation of currently developed $[Ca_{24}Al_{28}O_{64}]^{4+}: (4 * \partial)e^{-}(2 - \partial)O^{2-}$ electride formation processes. The electride formation processes can be divided into two groups with varied processing parameters: processes that extract the occluded anion species and those replacing occluded species.

1.4.2 Extraction Formation Processes

The occluded O^{2-}anions exhibit a high affinity to form more stable bonds, the basis of many reduction processes, and C12A7 electride formation extraction processes

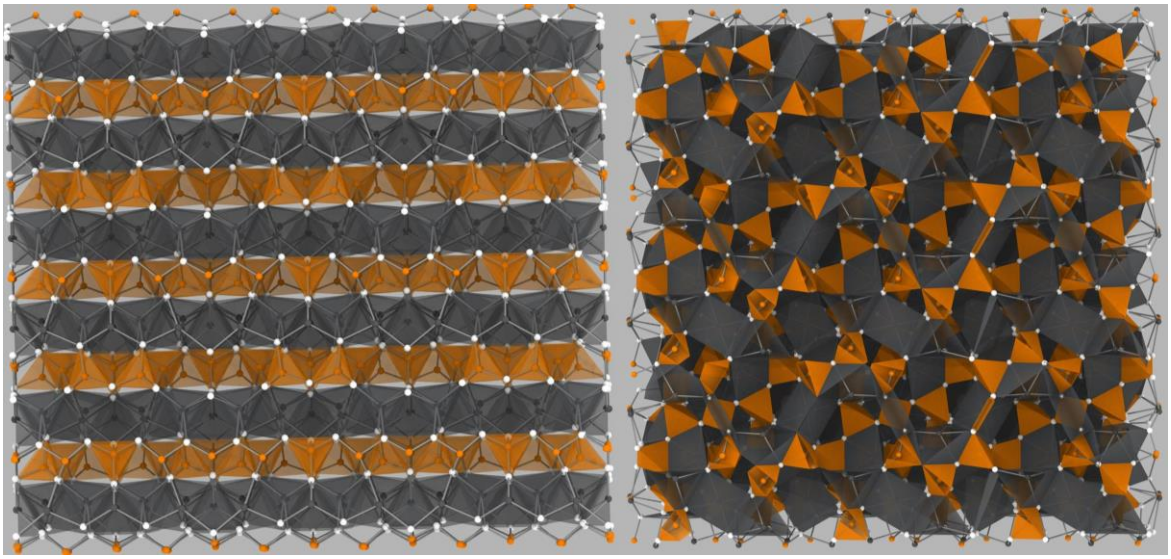

Figure 6 Comparison of layer C5A3 structure on the left and the C12A7 cage structure on the right. Ca atoms and oxygen coordination polyhedral is shown in gray, Al in orange, and Oxy

focus on using bulk metals and C as reducing agents.

1.4.2.1 Metal Reduction Processes

Metal extraction methods involve reacting the occluded O^{2-} anions with metals to form metal oxides. Ca metal is unstable and readily reacts with O_2 and H_2O in ambient atmosphere to form H_2 gas. Matsuishi et al. exploits this instability to form electride float-zone (FZ) single crystals, sealed in an evacuated (10^{-4} Pa) quartz ampule with Ca metal shot at a reduction temperature of 700 °C [37]. As process duration is increased, the initially clear single-crystals demonstrate the characteristic color change through green to black. After 240 h the carrier density (n_e) and electrical conductivity at room temperature (σ_{RT}) saturate at 2×10^{21}, which is close to the theoretical 2.33×10^{21} if all occluded $O^{2-}$is removed, and 100 S•cm^{-1}, respectively [37,47]. O^{2-} diffuses to the surface where it reacts with Ca in the vapor phase, $O^{2-}_{(cage)} + Ca_{(g)} \rightarrow CaO_{(surface)} + 2e^{-}_{(cage)}$.

After the process, the samples are encased in CaO layer that must be mechanically removed. This layer has negative processing impacts as it limits the processing temperature to 700 °C due to the increase in Ca stoichiometry, derived from the CaO layer, which moves the phase equilibria into a two phase C12A7 and C3A region. Further this CaO layer limits the application of this process to thin high surface area samples due to the oxygen inability to diffuse through this CaO layer to react with metallic Ca, thereby turning off the electride formation process.

Matsuishi et al. exploit the formation of the CaO phase by starting the system off equilibrium to use the CaO to directly synthesize $[Ca_{24}Al_{28}O_{64}]^{4+}:4e^{-}$powder [68]. The process involves reacting a C12A7 and CA mixture with Ca shot at 700 °C for 15 h in an evacuated (10^{-4}) sealed quartz tube. Subsequent grinding, resealing, and firing at 1100° C for 2 h led to the formation of the black C12A7 electride powder. This process was also carried out utilizing CaH_2 at 600–700 °C for 15 h, and found that dehydration of OH^{-} occupied cages to O^{2-} before reduction increased electron concentration suggesting that OH^{-} cannot be extracted by Ca oxidation [69]. Understanding that anions are needed to nucleate the clathrate framework, in this study, where there are no obvious template anions, suggests that direct C12A7 electride can be accomplished when the electride phase already exists. This same idea was observed when FZ single crystals were grown from a polycrystalline C12A7 feed rod and single crystal electride seed. When the electride seed was attached to a non-electride feed rod, it resulted in the formation of the electride phase [3,70]. Future experiments should explore different bulk metals in a hope of directly synthesizing doped C12A7 electrides and further investigate direct electride formation processes.

Kim et al. improved the Ca metal shot process by changing the reactive metal shot to Ti powder [2,58]. The resulting metal oxide film has the compositionTi_xO_{2-x}, where $1 \leq x \leq 2$, a non-stoichiometric oxide [71]. This allows for continual oxygen diffusion through the metal oxide layer allowing the process to be employed for single crystals of any size. The Ti extraction method also allows for the processing

temperature to be raised up to 1300 °C due to the stability of the C12A7-Ti_xO_{2-x} system [72]. This increase in processing temperature leads to an increase in O^{2-} diffusion in C12A7 resulting in shorter processing times [3]. Czochralski (CZ) grown single crystals (5 × 5 × 15 mm^3) were fired at 1100 °C in an evacuated (10^{-1} Pa) sealed quartz tube, and reached a n_e of 2.3×10^{21} and σ_{RT} of 1500 S•cm^{-1} after a reduction process time of 24 h compared to 240 h in the Ca method [58]. The increase in σ_{RT} is contributed to an increase in n_e and carrier mobility (μ_e) associated with metallic band conduction [3]. Ali et al. found that ideal reduction time and temperature was 48–60 h at 1100 °C and an increase in temperature to 1200 °C led to a decomposition of the C12A7 phase and an increase in duration led to a brittle sample and a large reduction in conductivity [73].

Palacios et al. applied a similar process with a different form of Ti and single crystal geometry [47]. Melt formed crystals are wrapped in a Ti foil and sealed in an evacuated (10^{-2} Pa) quartz tube and fired at 1000 °C. After a processing time of 48 h, the specimen showed a color change from clear to green and n_e was estimated, through analysis of SSXRD data, refining on the occluded anion site occupancy factor (sof), to be approximately 1.0×10^{21}. An increase in processing time to 144 h yielded black samples with a n_e of approximately 2.3×10^{21} [47]. The increase in process duration could be due to a smaller surface area associated with the Ti foil leading to less vapor transport as well as a decrease in temperature leading to a decrease in O^{2-} diffusion. The foil process needs further investigation as there was no mention of having to mechanically remove a TiO_2 layer in the reports by Palacios et al., and the size and irregular geometry of the melt formed crystals would make mechanical removal of this oxide layer difficult. Palacios et al. [48] also report using V foil and even a V sample container for neutron powder diffraction (NPD) experiments to reduce powder and melt formed single crystal samples. In the V foil process powder samples are fired at 1000 °C surrounded by the V foil in an evacuated (1.3×10^2 Pa) sealed quartz tube and in the V container process powder samples are sealed in an evacuated (10^{-3}) V-can and fired at 1100 °C for 8 h. In the V-can reduction process, electride formation was observed in the temperature range of 700 to 1100 °C, however, during the 8 h dwell at 1100 °C C12A7 decomposed to C5A3 and C3A.

Metal extraction techniques are ideal on single crystals where high process temperatures and times and post processing techniques are not an issue. Stable metal foil extraction methods show promise for processing of polycrystalline samples, and if metal oxides are formed in the process a direct synthesis route to doped $[Ca_{24}Al_{28}O_{64}]^{4+}:(4*\partial)e^-(2-\partial)O^{2-}$ may be easily realized.

The metal extraction technique cannot be applied to thin films; however, Miyakawa et al. developed a technique, similar in principle to the metal reduction method, utilizing a oxygen deficient C12A7 layer to reduce the previously deposited thin film below [74]. The oxygen deficient C12A7 replaces the metal as the reducing agent with a high affinity toward oxygen. C12A7 thin films were grown using pulsed laser deposition (PLD) where an amorphous C12A7 was deposited at room temperature and then crystallized in air at 1100 °C. The thin film was placed back into the PLD system

where another amorphous C12A7 layer was deposited under vacuum conditions at 700 °C. This top layer would be oxygen deficient and act as a reduction agent for the polycrystalline C12A7 thin film previously deposited. After mechanical removal of the top layer the resultant thin film displayed electrical conductivity as high as 800 S•cm^{-1}. This process has been repeated on $Sr_{12}Al_{14}O_{33}$ (S12A7) thin films and S12A7/C12A7 layered thin films, which is discussed later [75].

1.4.2.2 Carbonaceous Atmosphere Process

The second extraction method, CO/CO_2 reducing atmosphere, is fundamentally different than the previous reactive metal shot techniques. Kim et al. developed the process which can be performed on any starting form, including polycrystalline powder, thin films, or single crystals [60]. The advantage over the metal shot technique is the reduction reaction occurs in the gas phase, allowing for sample surfaces to remain unaffected during the process. Samples are placed in a graphite crucible, with a lid, under flowing inert gas. It is suspected that inside the crucible a strong carbon monoxide reducing atmosphere is formed reacting with the occluded O^{2-} to form CO/CO_2 gas, $O^{2-}_{(\mathrm{cage})} + \mathrm{CO}_{(\mathrm{g})} \rightarrow \mathrm{CO}_{2(\mathrm{g})} + 2e^{-}_{(\mathrm{cage})}$. A FZ single crystal sample fired at 1200 °C for 0.5 h produced a σ_{RT} of 4 S•cm^{-1}. EPR was used to determine carrier concentration, which can only identify carriers in the paramagnetic state. Therefore, actual carrier density is unable to be confirmed, and higher degrees of reduction may result by increased process times and/or temperatures. If this proposed reduction reaction occurs, the graphite crucible can be removed, and the entire process can be conducted with flowing CO gas allowing for quick batch processing. This is confirmed by electrical conductivity measurements on Fe-doped C12A7 FZ single crystals where electrical conductivity increased after processing in a CO/CO_2 atmosphere at 800, 900, and 1000 °C [76].

The CO/CO_2 reduction technique is versatile and can be applied to all sample types and geometries leading to electron loading at moderate process temperatures. However, the degree of maximum electron concentration needs to be investigated and long process durations may be needed to achieve a high degree of electron loading.

1.4.3 Replacement Formation Processes

Replacement reduction techniques work by replacing the occluded species and subsequently altering the replacement anion for localized electron generation. Currently, two main processes replacing the stoichiometric occluded anion O^{2-} have been developed with H^- and C_2^{2-}.

1.4.3.1 H^- Replacement and Photoionization Process

A H_2 gas reduction process allows for low levels of electron loading due to replacement $\mathrm{of}\ O^{2-}$and subsequent ionization of hydrogenous species. Hayashi et al. first published the light-induced insulator to conductor conversion of C12A7 [22]. FZ single

crystal samples underwent a firing process at 1300 °C in a flowing H_2 reducing atmosphere consisting of 20% H_2 and 80% N_2. After the samples were processed at 1300 °C for 2 h the single crystals were quenched to room temperature where no color change was observed and the σ_{RT} was low (insulating). Spectroscopy analysis showed the single crystals had a large concentration of H^- anions confirming that the anion replacement process had succeeded through the following chemical reaction, $O^{2-}_{(cage)} + H_{2\,(g)} \rightarrow OH^-_{(cage)} + H^-_{(cage)}$ [22]. Theoretical calculations by Sushko et al. suggest that the H_2 gas decomposes to an H^+ and H^- pair in the C12A7 framework [77]. The H^- anion is localized in the center of the cage stabilizing the clathrate framework. The H^+ ion diffuses through the sample until it bonds to an occluded O^{2-} anion, creating an occluded OH^- anion, or until it bonds to an oxygen in the clathrate framework [77]. After subsequent processing via UV light irradiation, with a flux of approximately 10^{20} photons•cm^{-2}, the sample demonstrated the characteristic green color change associated with localized electrons and a σ_{RT} of 0.3 S•cm^{-1} [22]. The UV irradiation forms C12A7 electride by ionizing the H^- ion forming elemental H and an electron, $H^-_{(cage)} \rightarrow H^0_{(cage)} + e^-_{(cage)}$. Theoretical calculations find that the elemental H is unstable and will thermally release another electron ionizing to an H^+anion. This anion then diffuses through the system until in bonds with framework or occluded O anions as previously discussed. The leads to the following reaction after the complete ionization process: $H^-_{(cage)} + O^{2-}_{(cage)} + \text{vacancy}_{(cage)} \xrightarrow{UV\,\lambda} OH^-_{(cage)} + 2e^-_{(cage)}$ [77,78]. This ionization is stable after irradiation has stopped, however at 320 °C the oxygen bonded protons and electrons recombine to form a H_2 molecule in a cage and the characteristic properties of the localized electrons are lost. Upon further heating to 550 °C H_2 gas is released from the sample and subsequent UV irradiation results in no formation of localized electrons [22].

Bertoni et al. conducted a similar process on polycrystalline samples where after processing sintered pellets, in a 4% H_2/96% N_2 forming gas at 1300 °C for 2 h, subsequent irradiation, using a Hg lamp (275–650 nm) for approximately 1 h, yielded electride C12A7 with a conductivity on the same order of magnitude as the single crystal [79]. These polycrystalline samples showed a decrease in decomposition temperature from 300 to 135 °C, the origin of which is unclear. The H_2 gas reduction process results in a lower electrical conductivity and carrier concentration associated with limited replacement between the O^{2-}occluded anions with H^- anions.

Sushko et al. [77] proposes treating $[Ca_{24}Al_{28}O_{64}]^{4+}:4e^-$, formed through another reduction process, to obtain the fully H^- replaced compound. Hayashi builds on this idea by employing a CaH_2 reduction process to obtain the highest concentration of $[Ca_{24}Al_{28}O_{64}]^{4+}:4H^-$ [21]. Stoichiometric FZ grown single crystals and electride single crystals were processed at 800 °C for various process times in sealed and evacuated quartz ampules and these samples were compared to FZ single crystals fired at 1300 °C for 6 h at 0.2 atm H_2. He found that reproducibility was poor and process duration

had no clear dependence on H^- inclusion. Improvement was found when the CaH_2 and samples were wrapped in Pt foil due to increased contact area between the reduction agent and the samples as well as the reduction of O species diffusion through or supplied by the silica tube. The samples were then ground to remove a containment layer on the outside of the single crystals. After 240 h, the H^- concentration was estimated to be ~2 × 10^{21}, corresponding to the highest replacement $[Ca_{24}Al_{28}O_{64}]^{4+}$: $4H^-$ and the lattice parameter was determined to be approximately 11.97 Å, smaller than stoichiometric C12A7 and similar to other fully monovalent balance C12A7 [78]. It was found that after ionization, samples with only half of the theoretical maximum H^- produced the highest electron concentrations and electron concentration decreased with decreasing O^{2-} content [78]. This verifies the ionization mechanisms and determines that the increasing H^- towards the maximum does not increase electron generation. "...the theoretical maximum number of photo generated electrons per unit cell is determine by the smaller value of either 2[H^-] or 2[O^{2-}] [78]." This process is similar to that conducted in the synthesis of powder electride C12A7 by Inoue et al., however, in their results no evidence due to H^- was observed in the absorption spectrum [69]. One explanation could be tied to the short processing time in comparison to the process conducted by Hayashi.

1.4.3.2 Carbide Replacement Process

The second replacement reduction technique involves the replacement of O^{2-} with C_2^{2-} that is suggested as a high temperature anion with the ability to stabilize the clathrate framework. The carbide anion has the same valence and similar ionic radii as O^{2-}, 1.2 Å and 1.4 Å, respectively [30]. It is believed that the carbide ion stabilizes the crystallization of the clathrate framework at high temperatures and then decomposes to 2C or 2CO on cooling [30]. This replacement reaction was first found by Kim et al. while trying to directly synthesize reduced C12A7 single crystals from a high temperature melt under a reducing atmosphere [30]. C12A7 stoichiometric powder was loaded into a graphite crucible with a lid and a melt was formed at 1600 °C in a strongly reducing CO/CO_2 atmosphere similar to the extraction method described in the previous section. When the melt was cooled, it crystallized in the C12A7 decomposition products, C3A and CA, as is expected when no template anions can nucleate crystallization of the cage framework. However, after repeating the process, the melt crystallized into the C12A7 electride suggesting that an anion must be present to nucleate the crystallization of the clathrate framework [30,57]. Raman spectra of the C3A and CA intermediary products revealed an absorption band matched to the reference for CaC_2, however, after the second processing step this absorption band is absent. This is consistent with the notion that the carbide ion decomposes out of the clathrate framework, however, it does not explain why the C12A7 decomposition occurs after the first processing step. Kim et al. report that the electride would seldom form after the initial firing process and is fully reproducible after the second. It is assumed that after the second firing process the carbide ion concentration is high enough to nucleate the full crystallization of the C12A7

electride phase. While this process can be used to directly fabricate melt formed electride single crystals, Kim et al. also show how a glass ceramic can be created by quenching the melt. The quenched melt is transparent and exhibits photochromism as a color change to gray is observed during UV irradiation [10]. The C12A7 crystallization temperature of the glass ceramic was determined to be 900 °C by differential thermal analysis (DTA). After quenching the glass ceramic is sealed in an evacuated quartz tube and fired at 1000 °C for 0.5 h it demonstrated the characteristic green color change and electronic conductivity similar to the melt cooled single crystals.

Recently reduction techniques in an intrinsic carbonaceous environment have been reported. Volodin et al. have developed and extensively studied the functionality of C coatings around TiO_2, MgO, Al_2O_3, and C12A7 nanoparticles [32]. These carbon coatings insulate the nanoparticles from surrounding particles allowing for phase and chemical reactions to occur on the individual particle level through the gas permeable carbon shell at high temperatures while preventing sintering of the nanostructure material. The C coated samples were placed in a graphite crucible sealed in an inert gas purged alumina ampoule and fired at various temperatures between 1250 and 1450 °C for 6 h. Electride formation was observed in all samples. This process closely replicates the CO/CO_2 exchange, albeit at temperatures above the decomposition temperature of 1200 °C observed by Palacios et al. under dry reducing conditions [48]. If the exchange reaction removes the occluded O^{2-} an additional anion would be needed to stabilize the C12A7 framework at these elevated temperatures. Due to this understanding, C_2^{2-} anions must have diffused into the structure from the C coatings, leading to the stability of the clathrate framework at high temperatures.

Chung et al. show that electride formation is possible during spark plasma sintering (SPS) due to the carbonaceous environment [31]. The high localized temperatures, electric field, and plasma all work together to promote diffusion of C species into the C12A7 framework. Graphite dies, which are filled with powdered C12A7, are loaded into an evacuated (1.3×10^{-4} Pa) chamber. The graphite die is necessary to conduct the large amounts of current needed to achieve a ramp rate of 100 °C/min to approximately 1000 °C while having the uniaxial strength to concurrently apply 40 MPa of pressure [31]. The fast ramp rate and short processing time, reported as 0.16 h, leads to fully dense samples with limited sintering [31]. At 900 °C no electride formation occurred, but as the processing temperature was raised to 1000 and 1100 °C electride formation occurred with a higher concentration of localized electrons at 1100 °C [31]. Samples processed at 900 °C were insulating at room temperature while those processed at 1000 °C were still resistive but saw an increase in electrical conductivity with σ_{RT} and n_e of 3.8×10^{-3} S•cm^{-1} and 3.2×10^{17}, respectively. At a processing temperature of 1100 °C the σ_{RT} and n_e increased to 5.88 S•cm^{-1} and 5.3×10^{19}, respectively. XRD, of samples processed at 900 and 1000 °C, showed partial decomposition of the C12A7 phase into C3A and CA. Raman spectra of these two samples also show an absorption band corresponding the C_2^{2-} anion. The concentration of the C_2^{2-} vibrational mode decreases as temperature increases as does the presence

of secondary phases. This suggests that the C_2^{2-} vibrational mode is correlated to the decomposition of C12A7 phase. The authors present the hypothesis that these secondary phases recrystallize into C12A7 with C_2^{2-} as the anion responsible for nucleating the clathrate framework. From this point they follow the same argument that the anion is only metastable and decomposes into 2C solid or it reacts with remaining occluded $O^{2-}$to produce 2CO gas.

These studies, especially the peculiar nature of the crystallization from the high temperature melt, suggest that a carbonaceous species are able to nucleate the C12A7 structure from the decomposition products of C12A7. What is not clear is if this process only occurs from the decomposition products or if the carbide anion can stabilize the already formed framework structure without decomposition.

O^{2-}, C_2^{2-}, and H^- are primarily the anions reported to form$[Ca_{24}Al_{28}O_{64}]^{4+}: 4e^-$. Other reports of electride formation are contributed to induced anion vacancies, however, these vacancies were reported to be small and large-scale extraction is not reported. Polfus et al. found an increase in electrical conductivity tied to occluded position and framework vacancies created by outgassing of NH^{2-} and N^{3-} under reducing conditions at 700 °C [29]. Dong et al. reported that, after SPS of isostructural $[Sr_{24}Al_{28}O_{64}]^{4+}: 4Cl^-$ (discussed later), a color change to brown and observed EPR signal are characteristic of localized F^+ centers [80]. Future research should determine if electride formation is possible through the removal of the numerous other anions.

1.5 Cationic Doping of $[Ca_{24}Al_{28}O_{64}]^{4+}: (4 * \partial)e^-(2 - \partial)O^{2-}$

The mineral mayenite forms a supergroup of minerals containing both isostructural oxides and silicates. Gfellar in his review goes in-depth into the different types and synthesis of various group members, especially Cl-mayenite structures, where the cation frameworks, consisting of Mg, Al, Si, Fe, and Ca, are stabilized by Cl^- anions occluded in the cages [44,81]. Research into other doped isostructural compounds has focused on increasing occluded anion occupancy, ion conduction, and luminescent properties. These studies have synthesized a wide variety of stoichiometric structures with aliovalent and isovalent dopants on cationic sites. Known synthetic doped-C12A7 compounds are summarized in Table 2.

The amount of research into the electride properties of doped-C12A7 is lacking in comparison to research on oxygen conduction and luminescence. Electride investigations of S12A7, an isostructural compound with 100% substitution of Sr for the Ca, was performed by Hosono's group who evaluated S12A7 thin films to see if they exhibited the same electride features as C12A7. Electride formation was confirmed through two reduction processes, H^- ion implantation and oxygen deficient amorphous C12A7. After UV irradiation, the implanted thin films exhibited similar conductivities, activation energy, temperature dependence, and absorption behavior as electride C12A7. The oxygen deficient reduction process led to a conductivity of approximately 270 S•cm^{-1} and an electron concentration of 1.3 × 10^{21}. Physical property

measurements coupled with a Drude effect in the optical absorption spectra confirms that S12A7 exhibits similar conductivity mode changes associated with the metal to insulator transition (MIT) of C12A7 [75]. Further studies of layered C12A7/S12A7 thin films found an increase in carrier mobility possibly associated with accumulation of charge carriers at the interface between the two films [82].

Bertoni et al. studied the possibility of $[Ca_{24}Al_{20}Si_8O_{64}]^{12+}$ being a transparent conductive oxide and induced electride formation through the H^- replacement reduction process [54]. Hydrogarnet was calcined at 800 °C to form the C12A7 compound, however, it is reported that samples decomposed at elevated temperatures and hydrogen incorporation by the conventional route was not possible. Instead H^- replacement was conducted at 300 °C through ion implantation. They found that the electrical conductivity double and tripled with increasing Si doping. Further it was found that a slight increase in Seebeck coefficient was observed with increasing dopant concentration and the sign remained negative as expected when below the MIT. Bertoni el al. stress that the increase in conductivity is primarily due to an increase in available hopping centers and not due to the gradual increase in electron concentrations associated with an increase in H^- [54]. Only low electron concentration electrides were formed and due to the metastability of the phase there is currently no process to fully reduce $[Ca_{24}Al_{20}Si_8O_{64}]^{12+}$ to the metallic regime. Bertoni et al. also studied $[Ca_{23.76}Mg_{0.24}Al_{28}O_{64}]^{4+}$ electride reduced by H^- replacement process and found that conductivity decreased with increasing Mg concentration due to Mg acting as a blocking agent for hopping conductivity [79]. These two studies illuminate that in the semiconducting regime hopping sites and not carrier concentration limits electrical conductivity.

Palacios et al. studied the electride formation of $[Ca_{24}Al_{26}Gd_2O_{64}]^{4+}$. The lattice parameter increased to 11.99734(6) Å. The samples were then reduced by firing pellets in an alumina crucible buried in graphite powder at 1350 °C for 6 h. The resultant gray pellet was multiphase with C3A phase in high concentrations. Structural refinements revealed that the lattice parameter of the reduced sample was close to 11.989 Å, close to the lattice parameter of undoped stoichiometric C12A7, and the Ga site occupancy refined to zero. Further X-ray photoelectron spectroscopy (XPS) revealed that the Ga^{3+} reduced to Ga metal and the conclusion was drawn that this metal must be nanodispersed on the C12A7 surface [83]. This study raises concern of the stability of doped C12A7 under reducing conditions, especially when considering transition metals that may change oxidations states under reducing conditions.

Ali et al. performed the Ti reduction process on blue colored 0.1 mol % Nd aliovalent doped C12A7 FZ single crystals [73]. Maximum electrical conductivity values were lower than those reported by Kim et al. and carrier mobility and concentration were measured via Hall measurements yielding large errors [58]. Ali et al. found that carrier mobility increases with annealing time while carrier concentration is independent of annealing time between 36 and 60 h. Further, when compared to undoped C12A7 at the same annealing time and temperature Ali et al. found an increase in carrier

Table 2 Isostructural synthesized C12A7 with dopant ionic radii, coordination number (CN), ionic radii (IR), observed dopant concentrations, available lattice parameters, and electride references (ER).

Dopant + (Co-Dopants) (valence/CN/IR) Al (3+/4/0.39) Ca (2+/6/1.00)	**Formula** Representing the dopant site and change in cage charge with aliovalent doping. The occluded species is not corrected for an increase in cage charge.	**References** Doped/co-doped C12A7 synthesis	**Sub. Site** Substitutional site for dopant normally determined by ionic radii	**Max *x*/*y*** Maximum stoichio-metric value reported	***a* [Å]**	**ER**
Sr (2+/6/1.18)	$[Sr_{24}Al_{28}O_{64}]^{4+}:2O^{2-}$ $[Sr_{24}Al_{28}O_{64}]^{4+}:4Cl^{-}$ $[Ca_xSr_{24-x}Al_{28}O_{64}]^{4+}:2O^{2-}$	[84]—SG [1] [85]—SS [2] [86]—HSS [3] [80]—SS [80]—SPS [4] [87]	Ca^{2+} **	0.24	12.33: (O^{2-}) [86] 12.346 (2): (Cl_2^-) [80]	[75] [82]
Fe (2+/4/0.63) (2+/6/0.78) (3+/4/0.49) (3+/6/0.645)	$[Ca_{24}Al_{28-x}Fe_xO_{64}]^{4+}:2O^{2-}$	[16]—SS [76]—FZ [5] [88]—FZ [89]—SG	Al^{3+} **	0.28	11.9904 (4) [76]	[76]
Cu (1+/4/0.6) (1+/6 /0.77) (2+/4/0.57) (2+/6/0.73)	$[Ca_{124-x}Cu_xAl_{28}O_{64}]^{4+}:2O^{2-}$	[90]—SS [89]—SG	Ca^{2+} **	1	11.974	N/A
Nb (3+/6/0.72) (4+/6/0.68) (5+/4/0.48) (5+/6/0.64)	$[Ca_{24}Al_{28-x}Nb_xO_{64}]^{4+2x+}:2O^{2-}$	[89]—SG	Al^{3+}	0.24	12.0049(3)	N/A
Ta (3+/6/0.72) (4+/6 /0.68) (5+/6/0.64)	$[Ca_{24-x}Ta_xAl_{28}O_{64}]^{4+?x+}:2O^{2-}$	[89]—SG	Ca^{2+}	0.24	N/A	N/A
Co (2+/4/0.58) (2+/6/~0.7) (3+/6/~ 0.58) (4+/4/0.4)	$[Ca_{24}Al_{28}O_{64}Co_x]^{4+}:2O^{2-}$	[89]—SG	unknown	0.24	N/A	N/A
V (2+/6/0.79) (3+/6/0.64) (4+/6/0.58) (5+/4/0.46) (5+/6/0.54)	$[Ca_{24}Al_{28-x}V_xO_{64}]^{4+2x+}:2O^{2-}$	[89]—SG	Al^{3+}	0.72-1.2	N/A	N/A
Ni (2+/4/0.55) (2+/6/0.69) (3+/6/~0.58) (4+/6/0.48)	$[Ca_{24}Al_{28-x}Ni_xO_{64}]^{4-x+}:2O^{2-}$	[88]—FZ [89]—SG	Al^{3+} **	0.28	N/A	N/A
Mg (2+/4/0.57) (2+/6/0.72)	$[Ca_{24-x}Mg_xAl_{28}O_{64}]^{4+}:2O^{2-}$	[79]—SS [89]—SG	Ca^{2+}	2	N/A	[79]

Table 2 Continued.

Dopant + (Co-Dopants) (valence/CN/IR)	Formula	References	Sub. Site	Max *x*/*y*	*a* [Å]	ER
Mn (2+/4/0.66) (2+/6/~0.75) (3+/6/0.65) (4+/4/0.39) (4+/6/0.53) (5+/4/0.33) (6+/4/0.25)	$[Ca_{24-x}Mn_xA_{28}O_{64}]^{4+}: 2O^{2-}$ $[Ca_{24-x}Mn_xAl_{28}O_{64}]^{4+}: 4Cl^{-}$	[91]—SS [16]—SS	Ca^{2+} possibly Al^{3+}	0.28	N/A	N/A
Ga (3+/4/0.47) (3+/6/0.62)	$[Ca_{24}Al_{28-x}Ga_xO_{64}]^{4+}: 2O^{2-}$	[83]—SS [89]—SG	Al^{3+} **	2	11.99734(6)	[83]
Zn + P (2+/4/0.6) (2+/6/0.74)	$[Ca_{24}Al_{28-x}Zn_xO_{64}]^{4-x+}: 2O^{2-}$	[92]—SS [89]—SG	Al^{3+}	1.3	11.993(2)	N/A
P (3+/6/0.44) (5+/4/0.17) (5+/6/0.38)	$[Ca_{24}Al_{28-x}P_xO_{64}]^{4+2x+}: 2O^{2-}$	[92]—SS	Al^{3+}	0.66	11.981(2)	N/A
Eu + (Mn, Yb, Nb) (2+/6/1.17) (3+/6/~0.947)	$[Ca_{24-x}Eu_xAl_{14}O_{64}]^{4+}: 2O^{2-}$	[91]—SS [93]—PLD [6] [94]—SS [95]—SS [96]	Ca^{2+}	0.04	N/A	N/A
Er (3+/6/0.89)	$[Ca_{24-x}Er_xAl_{28}O_{64}]^{4+x+}: 2O^{2-}$	[97]—CP [7] [95]—SS [96] [98]—CP	Ca^{2+}	0.12 0.72 [95] 2.4 [98]	N/A	N/A
Ce (3+/6/1.01) (4+/6/0.87)	$[Ca_{24-x}Ce_xAl_{28}O_{64}]^{4+x+}: 2O^{2-}$	[99]—SS [99]—SG [100]—SS [96] [101]—SS	Ca^{2+}	0.24	N/A	N/A
Dy + (Ce) (3+/6/1.07) (4+/6/0.912)	$[Ca_{24-x}Dy_xAl_{28}O_{32}]^{4+x+}: 2O^{2-}$	[102]—CP [103]	Ca^{2+}	0.48	N/A	N/A
Gd + (Sr) (3+/6/0.938)	$[Ca_{24-x}Gd_xAl_{28}O_{64}]^{4+x+}: 2O^{2-}$	[104]—SS [96]	Ca^{2+}	0.024	N/A	[104]
Tb + (Ce) (3+/6/0.923) (4+/6 /0.76)	$[Ca_{24-x}Te_xAl_{28}O_{64}]^{4+x+}: 2O^{2-}$	[100]—SS	Ca^{2+}	0.24	N/A	N/A
Nd (3+/6/0.983)	$[Ca_{24-x}Nd_xAl_{28}O_{64}]^{4+x+}: 2O^{2-}$	[94]—SS [73]—FZ	Ca^{2+}	0.2	N/A	N/A
Yb (2+/6 /1.02) (3+/6/0.868)	$[Ca_{24-x}Yb_xAl_{28}O_{64}]^{4+x+}: 2O^{2-}$	[95]—SS	Ca^{2+}	2.4	N/A	N/A
Ho (3+/6/0.901)	$[Ca_{24-x}Ho_xAl_{28}O_{64}]^{4+x+}: 2O^{2-}$	[105]—CP [98]—CP	Ca^{2+}	1.2	N/A	N/A
Pr (3+/6/0.99) (4+/6/0.85)	$[Ca_{24-x}Pr_xAl_{28}O_{64}]^{4+x+}: 2O^{2-}$	[106]—SS	Ca^{2+}	0.192	12.007	N/A
Sm (3+/6/0.958)	$[Ca_{24-x}Sm_xAl_{28}O_{64}]^{4+x+}: 2O^{2-}$	[107]—SG	Ca^{2+}	0.48	N/A	[107]

Table 2 Continued.

Dopant + (Co-Dopants) (valence/CN/IR)	Formula	References	Sub. Site	Max *x*/*y*	*a* [Å]	ER
Silicates						
Si (4+/4/0.26) (4+/6/0.4)	$[Ca_{24}Al_{20}Si_8O_{64}]^{12+}:6O^{2-}$	[17]—HT [8] [54]—HT [108]—HT	Al^{3+} **	-	11.9748 (15) [17]	[54]
Fe + Si	$[Ca_{24}Fe_{20}Si_8O_{64}]^{12+}:12Cl^{-}$	[109]—SS	Al^{3+} **	-	12.2158 (8)	N/A
Si + (Co, Ni, Cr, Cu, Fe)	$[Ca_{24-y}X_yAl_{20}Si_8O_{64}]^{12+}:6O^{2-}$	[110]—HT [108]—HT [111]—HT(Co)	Ca^{2+}	Cu (1.2) Cr (1.7) Co (0.82) Ni (2.4) Fe (0.96)	N/A	N/A

** Empirical confirmation; [1] SG—Sol-Gel synthesis; [2] SS—solid state synthesis; [3] HSS—High pressure solid state synthesis; [4] SPS—Spark Plasma Synthesis; [5] FZ—Float Zone Single Crystal synthesis;
[6] PLD—Pulsed Laser Deposition synthesis; [7] CP—Co-Precipitation synthesis; [8] HT—Hydrothermal synthesis; Highlighted ionic radii information is the observed or expected coordination of dopant. All Ionic radii information is from [112].

concentration with similar carrier mobility, and low temperature carrier mobility was higher in the doped case [73]. This is the first electride investigation of aliovalent doped C12A7 and shows an increase in carrier density and mobility from the undoped C12A7.

Since the CCB is responsible for electrical conductivity in C12A7, modifications to the chemical species in cage framework can have profound impacts on the landscape of DOS around the Fermi energy, leading to changes in electron localization, electrical conductivity, and Seebeck coefficient. Huang et al. performed DFT and electron localization function (ELF) calculations to investigate the change in DOS of the CCB and the change in attractive anionic species with various cation dopants. They modeled the stoichiometric and fully reduced electride structures doped with ~0.86 mol % of Cu, Sr, Fe, Ir, P, and V [1]. Lattice parameter had a linear trend with ionic radii validating the qualitative assessment of dopant substitution and substitutional site normally employed by experimental investigation. Cu, Fe, and Ir are exceptions to this rule suggesting an increase in cage distortion with respect to other studied dopants. As the electride is formed the lattice parameter increases by approximately 0.03 Å for all dopants except for Fe, where the lattice parameter only increases about 0.01 Å [1].

Density of state calculations confirm the assumption that small changes in the cage framework can drastically alter the density of states around the Fermi level, shown in Figure 7. Transition metal dopants lead to an increase in interstitial states in the stoichiometric case, which disappear as the electride is formed. At maximum electron loading Ir and Cu lead to occupied states at the Fermi level contrasted to the valley observed in the stoichiometric case, shown in Figure 4, and other dopant cases. In Cu-doped C12A7 the DOS of the CCB decreases from the stochiometric to the electride case further suggesting a distortion of the cage framework.

Electron localization function calculations are used to analyze chemical bonds and the localization of anionic species in C12A7. Huang et al. found the character of the

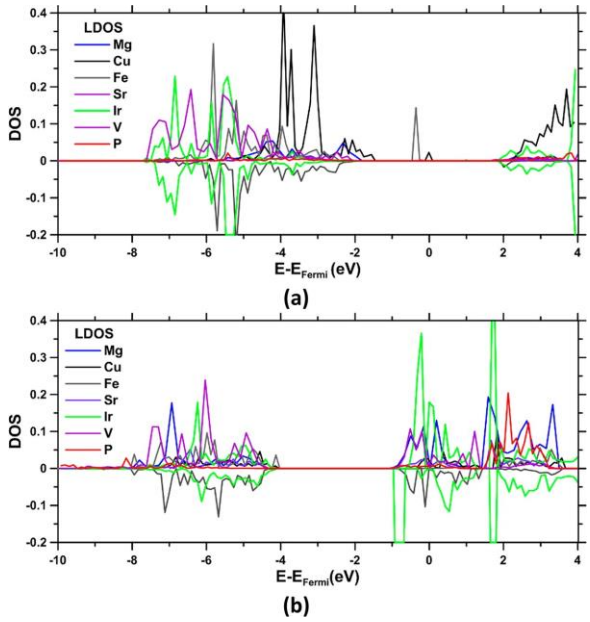

Figure 7 Local DOS with respect to dopant in (a) C12A7 and (b) C12A7 electride. Reprinted with permission from [1] . Copyright 2015 American Chemical Society.

occluded species, localization of the electron, and distortion of the C12A7 framework varies based on dopant. If the presence of a localize F+ like center electron indicates semiconducting hopping conduction and the absence of this localized attractor is characteristic of delocalized band conduction then Mg, Sr, P, and V exhibit a semiconducting state while Cu, Ir, and Fe exhibit band conduction at max electron concentration. This assumption is unclear as undoped-C12A7 shows a strong F^+ attractor, however previous investigations have shown that the dominant conduction carrier is a free carrier when fully reduced. The presence of localized attractors in the ELF calculations does align with the observation by Lobo et al. where increasing carrier concentration ultimately leads to an increase in lattice electron coupling observed in undoped C12A7. Will the increase in Fano effect be observed for Cu, Ir, and Fe doped systems? Does the distortion to the framework negate the formation of polarons at high electron loading like in other systems? For Mg doping a stronger attraction to the F^+ center than in undoped C12A7 confirms the theoretical and experimental results found by Bertoni et al. that Mg acts as a blocking agent in the hopping conduction regime [79].

Cationic dopants are theoretically predicted to have profound impacts on the structure and electrical properties of $[Ca_{24}Al_{28}O_{64}]^{4+}:4e^-$. Investigations into the effects of these dopants are few and research should proceed to quantify and confirm the effects dopants will have on the Seebeck coefficient, electrical conductivity, and superconducting transition. What is unclear is the experimental stability of the cation doped framework both during the process to extract or replace the occluded anions and in the final electride state.

1.6 Conclusions

$[Ca_{24}Al_{28}O_{64}]^{4+}:(4*\partial)e^{-}(2-\partial)O^{2-}$ consists of a clathrate cage framework whose complicated crystallographic structure results in interesting properties with potential applications in both the stoichiometric and electride states. The convertibility from a wide band gap insulator to semiconductor to metallic conductor is performed through processing without the need for acceptor and donator dopants as with traditional semiconductors. The strong atomic structure to physical property relationship is responsible for this transition and modifying this structure leads to a transformation of the electronic density of states. The intricacies of the mayenite structure are far from solved and future research is still needed. Some areas for future investigations are:

1. Determining what is responsible for the increase in the Fano effect with increased carrier concentration and what is the relationship between free carriers and polarons.
2. Synthesis of new doped-isostructural compounds with precise control of microstructure and characterize the atomic structure and electronic property changes that occur with doping.
3. Evaluate the kinetic formation behavior of C12A7 and evaluate the role of C5A3 in the calcium aluminate phase space.
4. Development of direct electride synthesis to circumvent cyclical synthesis procedures.

CHAPTER 2
Enhanced Sol-Gel synthesis of C12A7

2.1 Abstract

As the use of technical ceramics increases, the need for a controllable microstructure limits the application of conventional solid-state synthesis in favor of wet chemistry synthesis techniques. This chapter deals with the synthesis of Cu-doped C12A7 through the amorphous citrate and polymer assisted sol-gel techniques. The former is widely used in the literature without the necessary proper consideration for solution chemistry while the latter was developed and implemented for C12A7 in this report and proves robust for use without careful consideration for solution chemistry. In the amorphous citrate section, conventional the solution pH and solvent extraction technique were altered leading to successful Cu-C12A7 formation with a grain size of ~60 nm; the change in solution pH was predicted by theoretical complex diagrams and if the change in pH does not occur Cu precipitates were observed on the pure C12A7 microstructure. The PVA process utilizes cross linked polymers to overcome the intrinsic limitations of the amorphous citrate technique and proves robust to process variables making it better suited for black box adoption; The result is a fine-grained Cu-C12A7 product comparable to that formed by the amorphous citrate technique without the need to consider solution chemistry or process refinement.

2.2 Introduction

Basic ceramic technologies have been transformed into advanced technical ceramics with applications in energy conversion, aerospace, catalysis, medicine, armor and weapons, and electronics. The properties of these advanced material applications rely on tailoring and control of microstructural, structural, and continuum phase concentration properties [113]. The almost universal industrial synthesis method involves solid state synthesis where reactants, normally individual cation oxides or carbonates, are combined in stoichiometric ratios and fired at high temperatures. This synthesis process is controlled by arriving at a thermodynamically favorable state due to diffusion between the reactant phases. Diffusion pathways are characteristically long leading to areas of unreacted reactants and off-stoichiometric phases due to the gradient in local reactant stoichiometry. Reaction times can vary from hours to days depending on powder preparation techniques. In order to reduce this time samples can be ground, repelletized, and refired to disrupt the evolved non-ideal stoichiometric gradients and create shorter diffusion pathways to equilibrium. While some control is gained by reducing the particle size of the starting reactants the high process temperatures and long times leads to little control over microstructure. Solid State-Synthesis is widely adopted due to the well-established furnace industry and low level of technology and science leading to easy application, but lack of control and high process temperatures and times are characteristic of the process due to the unavoidable nano-micron level inhomogeneity of the starting mixture [114,115].

SSS techniques are inherently limited by the long diffusion pathways needed to reach desired stoichiometric homogeneity. As the cationic system increases in size, as would be the case with the study of doped C12A7 materials, the intrinsic disadvantages

of solid state synthesis become amplified. To ensure compositional homogeneity and obtain a controlled microstructure a transition to wet chemistry synthesis techniques is unavoidable. Wet-chemistry synthesis techniques overcome the disadvantages of solid state synthesis by fundamentally changing the source of the cations. To minimize the energy of the system the soluble species in solution will diffuse until there is a constant concentration gradient throughout the solution. If the proper stoichiometric ratio of soluble cationic complexes is prepared in solution, then the system is already stoichiometrically homogenous on an atomic level. The next challenge is converting this soluble homogeneity into the final product. The two main methods for converting solution homogeneity involve precipitation of metal complexes from the solution (Co-precipitation techniques) or evaporation of the solvent to form a stoichiometric gel/resin (sol-gel techniques) which can then be calcined to the desired oxide phase. Successful conversion of solution atomic level homogeneity leads to short diffusion pathways and high nucleation of the desired phase. This leads to a decrease in process temperature, a decrease in process time, and a controlled fine-grained, frequently below 100nm, microstructure.

The co-precipitation method relies on the precipitation of small grain individual cationic complexes. The diffusion pathways are much shorter than in the solid-state synthesis technique, but process engineering becomes difficult as the kinetics of precipitation can vary between cationic species [115]. Some systems may result in a mixed cationic precipitate, which if in the correct stoichiometric ratio, would be highly desirable, but as the cationic system increases it becomes unlikely to obtain a stoichiometric mixed metal precipitate. The precipitation method relies on the removal of cationic solutes from the solution; the kinetics of which are hard to control [115].

The sol-gel methods are the inverse of the precipitation method. They involve removal of the solvent resulting in a gel or thermoplastic resin. There are four main classes of gel/resins; the metal-oxane polymer, Metal small molecule, In-situ polymerization, and polymer assisted gels/resins. A comprehensive review highlighting the evolution of ‘sol-gel’ synthesis is presented by Danks et al. [114].

The metal-oxane polymer gel technique, also known as alkoxide-based sols, led to the advent of sol-gel synthesis and preserved the homogeneity of the solution by forming a polymer network consisting of M-OH-M or M-O-M chains. This process is limited by the availability and stability of metal alkoxies [114]. The compositional space for these alkoxides is small and the cost leads poor economic viability.

The metal small molecule resin retains the homogeneity of the solutions by forming chains of weakly interacting metal ligand chelates (ML) which are then concentrated into a thermoplastic like resin precursor during solvent evaporation. The most commonly used method, known as the amorphous citrate method, utilizes citric acid (CA) as the chelating ligand. Process engineering is required as the formation of metal chelates is necessary to transfer the homogeneous solution state to a solid state. Control of process pH, metal to ligand ratio, and solvent evaporation may be necessary

to ensure formation of desired metal complexes and prevent precipitation of unwanted complexes such as nitrates, hydroxides, or even higher order ML complexes. The use of other ligands such as ethylene diamine tetra-acetic acid (EDTA) to ensure metal complexation is frequently documented in the literature for cations which do not have an affinity for coordination with citrate. Metal chelation is fundamental to the process and the metal complex process is particularly suited to complex cationic systems since the organic resin remains until combustion occurs at 300-400 °C. The fact that the ML complexes must form for all cations in the system under the same synthesis conditions is an inherent limitation of the technique. Further, the ML complexes are only weakly interacting with each other and differences in decomposition temperature of these complexes can result in the segregation of cationic species; this leads to heterogenous metal oxide or metal clusters during calcination and firing eliminating the atomic level homogeneity.

The In-situ polymer complex process (IPC), primarily referred to as the Pechini process, attempts to avoid heterogeneity during ML complex decomposition by trapping the ML complexes in a polymer network which will not decompose until higher temperatures. The Pechini process revolves around the reaction of α-hydroxy carboxylic acid, traditionally citric acid, with a polyhydroxy alcohol such as ethylene glycol (EG) during solvent evaporation. The polymer network that is formed in this reaction prevents diffusion of decomposed citrate complexes due to the low mobility of metal cations in a heavily branched polymeric net [115]. Only after the decomposition of all ML complexes does the polymeric network decompose retaining homogeneity through the decomposition phase [115]. While this is an improvement over the metal complex process an increase in the pH leads limits polyesterification and the increase in the pH is conventionally required for the successful formation of metal citrate complexes. This limits the ideal application to systems where pH does not need be controlled. This process involves a large wt. % of organic species (~70-80%) leading to a low yield of the desired oxide powder and an increase in cost making in inherently inefficient.

The polymer complex gel technique follows a similar idea of the In-situ polymer complex gel and seeks to restrict the diffusion of metal cations in a polymer net. Poly-vinyl alcohol (PVA) is often used as the polymer source. This process is fundamentally different as the metal cations homogeneity is controlled both by the bonding to acetic or hydroxide substituents and steric entrapment. The PVA matrix decomposes gradually over a larger temperature range than the metal complex techniques and remains until a higher temperature further prolonging atomic homogeneity [114–117]. The polymer complex process also results in a lower wt.% of organic species (~50%) leading to a higher yield of the desired oxide powder, and the low cost and high industrial availability of PVA makes for an economically viable synthesis process [118].

C12A7 is conventionally synthesized through solid state synthesis techniques which will prove to limit the control during direct synthesis of the doped electride phase. In this chapter the amorphous citrate and the PVA polymer assisted processes are engineered for Cu-C12A7 synthesis. Cu-doped C12A7 is chosen due its ability to

increase performance of the catalytic activity of oxy-C12A7 and predicted effects on electronic structure in the electride. It also represents a 'hard use' case due to the polyvalent nature and large, 30%, difference in ionic radii with reference to Ca [112]. The application of these synthesis methods extends past the niche scope of this dissertation and the process engineering presented herein should be used as a reference for implementation of further C12A7 synthesis. As will be revealed if the amorphous citrate synthesis method is used without consideration of synthesis conditions the resultant material will be heterogenous with Cu as a secondary phase and not in the C12A7 structure. For general black box use I present the polymer assisted method which proves robust without the need for process engineering considerations.

2.3 The Effect of Process pH on the Amorphous Citrate Sol-gel Synthesis of Cu-doped $Ca_{12}Al_{14}O_{33}$

2.3.1 Introduction

The amorphous citrate sol-gel technique is commonly used for synthesis of nominally doped oxides such as C12A7.[84,99,107,114,115] The first step is to transfer the homogeneity of the solution to a transparent thermoplastic resin, commonly referred to as a gel, free from precipitation. Precipitation of a cationic phase will degrade the atomic level of homogeneity intrinsic to a solution and lead to regions with differing stoichiometry. The ligand concentration, the ratio between citric acid and metal cations (ligand (L):metal (M)), and the pH of the initial solution must be controlled to prevent precipitation of cationic species and promote chelation of cationic citrate complexes. To assess the influence of pH and ligand concentration, complex diagrams are calculated based on thermodynamic stability or formation constants. The formation constants were largely reported over 30 years ago and only for dilute ionic strengths.[119,120] The constructed diagrams are only as accurate as the underlying measurements of stability constants but serve as a good foundation on which to start experimentation. The pH normally needs to be raised to prevent the formation and precipitation of metal nitrates (e.g., $BaNO_3$ in $YBa_2Cu_3O_7$-d oxide synthesis). Raising the pH too high can result in the precipitation of hydroxides.[115] Precipitation of higher-order ML species such as $[Ca_3(C_6H_5O_7)_2]$, $[Cu_2(C_6H_5O_7)(OH)]$, $[Mg_3(C_6H_5O_7)_2]$, and $Pb_3(C_6H_5O_7)_2$ are possible, but increasing the L:M ratio or altering solvent removal can prevent the precipitation of these species while ensuring full citrate complexation.[121–124]

The second step in producing a homogeneous oxide via a sol-gel synthesis is controlling the decomposition process to ensure that homogeneity is maintained until the desired phase(s) can nucleate. There are four broad stages of decomposition for the citric acid resins, but the underlying chemical reactions are complex and numerous. The four broad stages are shown in Figure 8 and include:

1) **Solvent Evaporation (<160 °C):** At lower temperatures, organic species are stable and solvent and volatile evaporation is the main source of weight loss.

2) **Decarboxylation, Dehydroxylation, and Decomposition (160-275 °C):** During this stage, nitrates will decompose through combustion with remaining uncomplexed citric acid, leading to an intense weight loss event. Complexed citric acid will decompose through the release of CO_2 and H_2O to trans-aconitic acid, trans-aconitic anhydride, and finally citraconic anhydride[125]. While this step will occur without oxygen through thermal degradation, the presence of oxygen will allow for oxidative decomposition that can lead to a more intense weight loss.[126] This combustion leads to a temporary local reducing environment and can cause a change in valence of polyvalent cations and, ultimately, segregation of the homogeneous resin.[127]

3) **Decomposition of Metal Citrates (275-380 °C):** This is the stage where the metal citrate complexes will decompose, yielding metal oxides. The decomposition of different metal complexes will happen at different temperatures, which can lead to segregation and nucleation of individual metal oxide phases.[128]

4) **Organic Species Combustion (380+ °C):** This is the final weight-loss event and involves the combustion of all remaining organic species, primarily N containing species, through oxidative decomposition. This decomposition will not occur when performed in an inert environment, and nucleation of the oxide will occur in a carbonaceous matrix, yielding a carbon ceramic composite.[126]

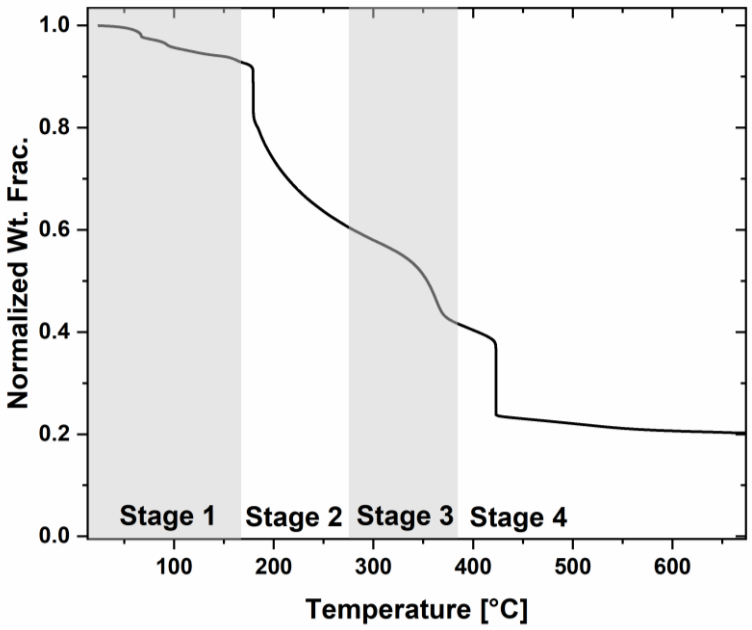

Figure 8 Characteristic decomposition steps in amorphous citrate sol-gel calcination. Magnitude and onset temperature of various decompositions will vary system to system and depend on data collection parameters.

The final step of the synthesis process involves the nucleation and crystallization of the desired phases and is the step where the least amount of control is available. Even if homogeneity is maintained through the first two steps, oxide formation may not follow the thermodynamically favorable state due to sluggish cationic diffusion at lower temperatures. Disordered phases with fast nucleation kinetics generally form first due to short diffusion paths. Such is the case in the Pb perovskite synthesis where a pyrochlore forms first due to the disordered structure. In this case, the pyrochlore phase was avoided by quickly heating to elevated temperatures where thermodynamics has a stronger role and the perovskite phase will form.[129]

The synthesis of pure C12A7 via the amorphous citrate route has been documented by Ude et al., and a reduction in synthesis temperature and time was observed, as would be expected when moving from solid state synthesis to a wet chemistry technique.[130] It was identified that $CaCO_3$ formation and subsequent decomposition hindered phase-pure synthesis below 900 °C. While this was inhibited by altering the processing atmosphere, careful control over the resin formation variables will prove to be a more viable option.

This section develops a standard process for engineering the synthesis of doped C12A7 through the amorphous citrate method. The technique is often used without proper consideration of the underlying controlling factors and as will be seen taking a ground up approach to the synthesis ensures the desired outcome. The effects of altering solution pH and solvent extraction on the synthesis of Cu-doped C12A7 are elucidated by characterizing resin homogeneity, decomposition homogeneity, and the kinetics of phase formation.

2.3.2 Theoretical Complex Diagrams

In order to determine the optimal solution pH for pure and Cu-C12A7 synthesis, theoretical complex diagrams need to be calculated. The amorphous citrate process is reliant on achieving a citrate resin to retain homogeneity. If metal citrate complexes are not thermodynamically favorable to form, then other metal complexes such as hydrates, nitrate, hydroxides, etc., will dominate and prevent the formation of a homogeneous resin. The thermodynamics of complex formation were published decades ago in the form of equilibrium or stability constants. An equilibrium constant is related to the Gibbs free energy of the system and corresponds to the ratio between the concentration of products and reactants, $K = [Products]/[Reactants]$. As this number increases above one, products are more likely to form; conversely, reactants are more likely to be present as this number decreases below one. A model to produce complex diagrams for a specified pH is possible by determining all possible chemical reactions and K values for a given cationic citrate solution.[115,131,132] Table 3 through Table 7 document all possible cationic complexes between Ca^{2+}, Al^{3+}, Cu^{2+}, NO_3^-, OH^-, $citrate^{3-}$, and H_2O. The possible complexes can all be related in terms of the concentration of free citrate, nitrate, aluminum, copper, and calcium ions. These five independent unknowns can be uniquely solved with the five mass balance equations shown in Table 7, and they can

then be used to calculate the concentration of each complex present in the solutions. For the calculation of pure complex diagrams Cu-containing phases and Cu mass balance equation is not included in the simulation, but all other equations remain the same. The calculation an implementation of these diagrams involves the assumption that:

1) Thermodynamic data taken at equilibrium and near room temperature can be used to predict behavior in a non-equilibrium system at temperatures up to 90 °C.
2) The solution is assumed to be ideal.
3) The concentration of the complexes does not change as temperature is increased.

In order to solve the system of non-linear equations with five unknowns, the multivariate Newton-Raphson (NR) method is employed. The NR method is an iterative root-finding algorithm that solves a system of *n* non-linear algebraic equations for *n* unknowns. The formation of complex diagrams has been implemented in other cationic systems, and we have reproduced the results from Lee and Fang to validate the Newton Raphson method. [131]

Lee and Fang calculated the complex diagrams for an Fe-Ba system and characterized the change in pH to formation of the final product.[131] A comparison between the complex diagrams calculated by Lee and Fang and those calculated through the Newton-Raphson (NR) method in the present research is shown in Figure 9.[131] Lee and Fang reported all equations and constants used, allowing this to be a proof that the NR method is accurate in determining the roots to the unknown mass balance equations. The results are nearly identical, but the efficiency of the NR method allows the number of calculated points to increase by two orders of magnitude, thereby increasing the resolution of the curve. This becomes especially advantageous in areas of large concentration changes. For example, Lee and Fang's $Fe(H_2O)$ complex concentration shows a continual decrease, whereas the $Fe(H_2O)$ complex concentration curve created with the NR method slightly increases at low pH before decreasing.

Table 3 Dissociation of citric acid through the three different protonated states

Reaction	Equilibrium Ratio	Equilibrium Constant	Ref.
$H_3Cit \leftrightarrow H_2Cit^- + H^+$	$k_1 = \frac{[\mathrm{H_2Cit^-}][\mathrm{H^+}]}{[\mathrm{H_3Cit}]}$	$k_1 = 1.34 * 10^{-3}$	[133]
$H_2Cit^- \leftrightarrow HCit^{2-} + H^+$	$k_2 = \frac{[\mathrm{H\,Cit^{2-}}][\mathrm{H^+}]}{[\mathrm{H_2Cit^-}]}$	$k_2 = 5.77 * 10^{-4}$	[133]
$HCit^{2-} \leftrightarrow Cit^{3-} + H^+$	$k_3 = \frac{[\mathrm{Cit^{3-}}][\mathrm{H^+}]}{[\mathrm{H\,Cit^{-2}}]}$	$k_3 = 2.4 * 10^{-6}$	[133]

Table 4 Possible Ca complexes and equilibrium constants

Reaction	Equilibrium Ratio	Equilibrium Constant	Ref.
$Cit^{-3} + Ca^{2+} \leftrightarrow Ca(Cit)^{-}$	$k_4 = \frac{[Ca(Cit)^{-}]}{[\mathrm{Cit}^{3-}][\mathrm{Ca}^{2+}]}$	$k_4 = 4.79 * 10^4$	133
$\mathrm{H\,Cit}^{2-} + Ca^{2+} \leftrightarrow Ca(HCit)$	$k_5 = \frac{[\mathrm{Ca(HCit)}\,]}{[\mathrm{H\,Cit}^{2-}][\mathrm{Ca}^{2+}]}$	$k_5 = 1.23 * 10^3$	133
$H_2Cit^{-} + Ca^{2+} \leftrightarrow Ca(H_2Cit)^{+}$	$k_6 = \frac{[\mathrm{Ca(H_2Cit)}^{+}]}{[\mathrm{H_2Cit}^{-}][\mathrm{Ca}^{2+}]}$	$k_6 = 12.6$	133
$OH^{-} + Ca^{2+} \leftrightarrow Ca(OH)^{+}$	$k_7 = \frac{[Ca(OH)^{+}]}{[OH^{-}][\mathrm{Ca}^{2+}]}$	$k_7 = 19.95$	134
$2\,OH^{-} + Ca^{2+} \leftrightarrow Ca(OH)_2$	$k_8 = \frac{[\mathrm{Ca(OH)_2}\,]}{[OH^{-}]^2[\mathrm{Ca}^{2+}]}$	$k_8 = 1.55 * 10^5$	134
$NO_3^{-} + Ca^{2+} \leftrightarrow Ca(NO_3)^{+}$	$k_9 = \frac{[Ca(NO_3)^{+}\,]}{[NO_3^{-}]\,[\mathrm{Ca}^{2+}]}$	$k_9 = 5.01$	134
$2\,NO_3^{-} + Ca^{2+} \leftrightarrow Ca(NO_3)_2$	$k_{16} = \frac{[\mathrm{Ca(NO_3)_2}\,]}{[NO_3^{-}]^{\,2}[\mathrm{Ca}^{2+}]}$	$k_{16} = 3.98$	134

Table 5 Possible Al complexes and equilibrium constants

Reaction	Equilibrium Ratio	Equilibrium Constant	Ref.
$OH^{-} + Al^{3+} \leftrightarrow Al(OH)^{2+}$	$k_{10} = \frac{[Al(OH)^{2+}]}{[OH^{-}]\,[\mathrm{Al}^{3+}]}$	$k_{10} = 1.02 * 10^9$	134
$2\,OH^{-} + Al^{3+} \leftrightarrow Al(OH)_2^{+}$	$k_{11} = \frac{[Al(OH)_2^{+}\,]}{[OH^{-}]^{\,2}[\mathrm{Al}^{3+}]}$	$k_{11} = 5.01 * 10^{18}$	134
$3\,OH^{-} + Al^{3+} \leftrightarrow Al(OH)_3$	$k_{12} = \frac{[Al(OH)_3\,]}{[OH^{-}]^{\,3}[\mathrm{Al}^{3+}]}$	$k_{12} = 1 * 10^{27}$	134
$4\,OH^{-} + Al^{3+} \leftrightarrow Al(OH)_4^{-}$	$k_{13} = \frac{[Al(OH)_4\,]}{[OH^{-}]^{\,4}[\mathrm{Al}^{3+}]}$	$k_{13} = 1 * 10^{33}$	134
$Cit^{3-} + Al^{3+} \leftrightarrow Al(Cit)$	$k_{14} = \frac{[Al(Cit)]}{[\mathrm{Cit}^{3-}][\mathrm{Al}^{3+}]}$	$k_{14} = 1 * 10^8$	135136
$HCit^{2-} + Al^{3+} \leftrightarrow Al(HCit)^{+}$	$k_{15} = \frac{[Al(HCit)^{+}\,]}{[\mathrm{HCit}^{2-}][\mathrm{Al}^{3+}]}$	$k_{15} = 5.01 * 10^4$	135136
$Al(Cit) \leftrightarrow Al(H_{-1}Cit)^{-} + \mathrm{H}^{+}$	$k_{17} = \frac{[Al(H_{-1}Cit)^{-}][\mathrm{H}^{+}]}{[AlCit\,]}$	$k_{17} = 3.98 * 10^{-4}$	135

Table 6 Possible Cu complexes and equilibrium constants

Reaction	Equilibrium Ratio	Equilibrium Constant	Ref.
$Cit^{3-} + Cu^{2+} \leftrightarrow Cu(Cit)^{-}$	$k_{18} = \frac{[Cu(Cit)^{-}]}{[\mathrm{Cit^{3-}}][\mathrm{Cu^{2+}}]}$	$k_{18} = 7.94 * 10^{5}$	133
$HCit^{2-} + Cu^{2+} \leftrightarrow Cu(HCit)$	$k_{19} = \frac{[Cu(HCit)]}{[\mathrm{HCit^{2-}}][\mathrm{Cu^{2+}}]}$	$k_{19} = 2.63 * 10^{3}$	133
$H_2Cit^{-} + Cu^{2+} \leftrightarrow Cu(H_2Cit)^{+}$	$k_{20} = \frac{[Cu(H_2Cit)^{+}]}{[\mathrm{H2Cit^{2-}}][\mathrm{Cu^{2+}}]}$	$k_{20} = 1.82 * 10^{2}$	133
$Cu(Cit)^{-} + Cu^{2+} \leftrightarrow Cu_2(Cit)^{+}$	$k_{21} = \frac{[Cu_2(Cit)^{+}]}{[\mathrm{CuCit}][\mathrm{Cu^{2+}}]}$	$k_{21} = 1.58 * 10^{2}$	133
$2\ Cit^{3-} + 2\ Cu^{2+} \leftrightarrow Cu_2(Cit)_2^{-2}$	$k_{22} = \frac{[Cu_2(Cit)_2^{-2}]}{[\mathrm{Cit^{3-}}]^2[\mathrm{Cu^{2+}}]^2}$	$k_{22} = 1.58 * 10^{13}$	133
$OH^{-} + Cu^{2+} \leftrightarrow Cu(OH)^{+}$	$k_{23} = \frac{[Cu(OH)^{+}]}{[OH^{-}]\,[\mathrm{Cu^{2+}}]}$	$k_{23} = 1.99 * 10^{6}$	133
$2\ OH^{-} + Cu^{2+} \leftrightarrow Cu(OH)_2$	$k_{24} = \frac{[Cu(OH)_2]}{[OH^{-}]^2\,[\mathrm{Cu^{2+}}]}$	$k_{24} = 6.31 * 10^{12}$	133
$3\ OH^{-} + Cu^{2+} \leftrightarrow Cu(OH)_3^{-}$	$k_{25} = \frac{[Cu(OH)_3^{-}]}{[OH^{-}]^3\,[\mathrm{Cu^{2+}}]}$	$k_{25} = 3.16 * 10^{14}$	133
$4\ OH^{-} + Cu^{2+} \leftrightarrow Cu(OH)_4^{2-}$	$k_{26} = \frac{[Cu(OH)_4^{2-}]}{[OH^{-}]^4\,[\mathrm{Cu^{2+}}]}$	$k_{26} = 3.98 * 10^{15}$	133
$NO_3^{-} + Cu^{2+} \leftrightarrow Cu(NO_3)^{+}$	$k_{27} = \frac{[Cu(NO_3)^{+}]}{[NO_3]^1\,[\mathrm{Cu^{2+}}]}$	$k_{27} = 7.94 * 10^{-1}$	133
$2\ NO_3^{-} + Cu^{2+} \leftrightarrow Cu(NO_3)_2$	$k_{28} = \frac{[Cu(NO_3)_2]}{[NO_3]^2\,[\mathrm{Cu^{2+}}]}$	$k_{8} = 2.51 * 10^{-1}$	133

Table 7 Mass balance equations

Mass Balance Equations
$[\boldsymbol{Citrate}]_{\boldsymbol{T}} = [H_3Cit] + [H_2Cit^{-}] + [HCit^{2-}] + [Ca(HCit)^{+}] + [CaCit^{-}] + [Ca(H_2Cit)^{+}] + [Al(Cit)] + [Al(HCit)^{+}] + [Al(H_{-1}Cit)^{-}] + [Cu(Cit)^{-}] + [Cu(HCit)] + [Cu(H_2Cit)^{+}] + [Cu_2(Cit)^{+}] + [Cu_2(Cit)_2^{-2}]$
$[\boldsymbol{Ca^{2+}}]_{\boldsymbol{T}} = [Ca(NO_3)_2] + [Ca(NO_3)^{-}] + [Ca(OH)_2] + [Ca(OH)^{-}] + [Ca(H_2Cit)^{+}] + [Ca(HCit)] + [CaCit^{-}] + [Ca^{2+}]$
$[\boldsymbol{Al^{3+}}]_{\boldsymbol{T}} = [Al(OH)^{2+}] + [Al(OH)_2^{+}] + [Al(OH)_3] + [Al(OH)_4^{-}] + [Al(Cit)] + [Al(HCit)^{+}] + [Al(H_{-1}Cit)^{-}] + [Al^{3+}]$
$[\boldsymbol{Cu^{2+}}]_{\boldsymbol{T}} = [Cu(Cit)^{-}] + [Cu(HCit)] + [Cu(H_2Cit)^{+}] + [Cu_2(Cit)^{+}] + [Cu_2(Cit)_2^{-2}] + [Cu(OH)^{+}] + [Cu(OH)_2] + [Cu(OH)_3^{-}] + [Cu(OH)_4^{2-}] + [Cu(NO_3)^{+}] + [Cu(NO_3)_2]$
$[\boldsymbol{NO_3^{-}}]_{\boldsymbol{T}} = [Cu(NO_3)^{+}] + [Cu(NO_3)_2] + [Ca(NO_3)_2] + [Ca(NO_3)^{-}]$

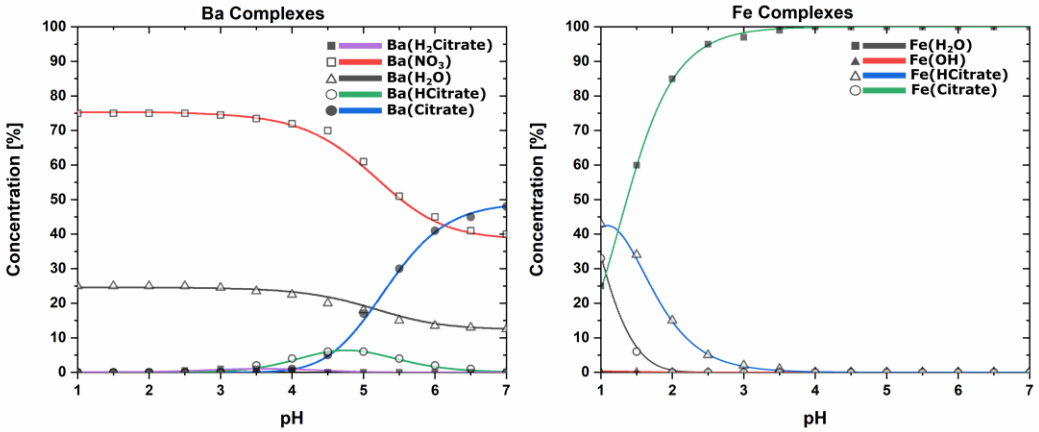

Figure 9 Comparison of the complex diagram published by Lee and Fang for the Fe-Ba-citrate system and the complex diagram produced with identical equations and constants through the Newton-Raphson method [131]. Reference data points are shown as symbols and estimated from their figures.

Citric acid is a weak triprotic acid, and nitrate-citrate solution is naturally acidic (pH < 1) due to the deprotonation of $H_3citrate$. In this acidic solution the metal cations will generally be coordinated with H_2O at low pH values. As the pH of the solution is increased, various deprotonated versions of the citrate molecule such as ML, MHL, or MH_2L (M = metal L = citrate) will form. Citrate complexes are desired and will lead to a homogeneous citrate resin. The window where citrate complexes occur varies as a function of pH, cation concentration, and citrate concentration.

The complex diagrams for the Cu-Ca-Al and Ca-Al nitrate citrate solutions were calculated with the NR method while parameter-stepping through every thousandth of a pH from 1 to 9. The specified molarities correspond to the synthesis of doped $Ca_{12}Al_{14}O_{33}$. These molarities are 0.0501 for Al, 0.039 for Ca, 0.004 for Cu, and the equivalent corresponding concentration of nitrate for the synthesis of Cu-C12A7 and 0.0501 for Al and 0.043 for Ca for the synthesis of pure-C12A7. All calculations converged to an average relative tolerance of 10^{-8} in the five unknowns. The calculations were repeated with increases in the citric acid concentration corresponding to an increase in the ratio of L:M from the theoretical minimum 1:1 to 2:1 and 10:1.

The diagrams in Figure 10 show that Al and Cu readily form citrate complexes at low pH at the cost of delaying the formation of Ca complexes. As the citrate-to-metal-ion ratio is increased, the formation of citrate complexes is pushed to lower pH values, lowering the concentration of hydrate and nitrate species, while the formation of hydroxides is pushed to higher pH values. The largest change occurs with the increase of L:M ratio to 2:1 with small improvements in the concentration of the higher ordered citrate species when the ratio is raised to 10:1. An increase in pH of the nitrate citrate

solution in the range of 4 to 6 leads to only citrate metal complexes, resulting in a homogeneous resin of atomically mixed cations.

The complex diagrams in Figure 11 characterize the cationic complex behavior in an undoped C12A7 cationic system where Ca and Al are the only cationic species. The behavior is similar to that as in the case with Cu with; a higher affinity for Ca(NO3)2 species is observed at lower pH values due to the lack of competition with Cu, and the range of acceptable pH values decreases from 4-6 to 3-6 without the limitation of having to form Cu complexes

As a result of the theoretical analysis, it is determined that the optimal pH for the synthesis of homogeneous Cu-C12A7 is in the range of 4 to 6 and a pH range for 3 to 6 for pure-C12A7. Synthesis at a lower pH will result in a heterogenous citrate resin due to a lack of full citrate complexation. From a synthesis point of view, the pH must be modified from its natural value of less than 1 through the addition of another component that does not impact the synthesis. This is counter to what is currently reported in the literature for the amorphous citrate synthesis of C12A7 that, as an invariant compound, is sensitive to local changes in stoichiometry. This loss of citrate resin homogeneity is

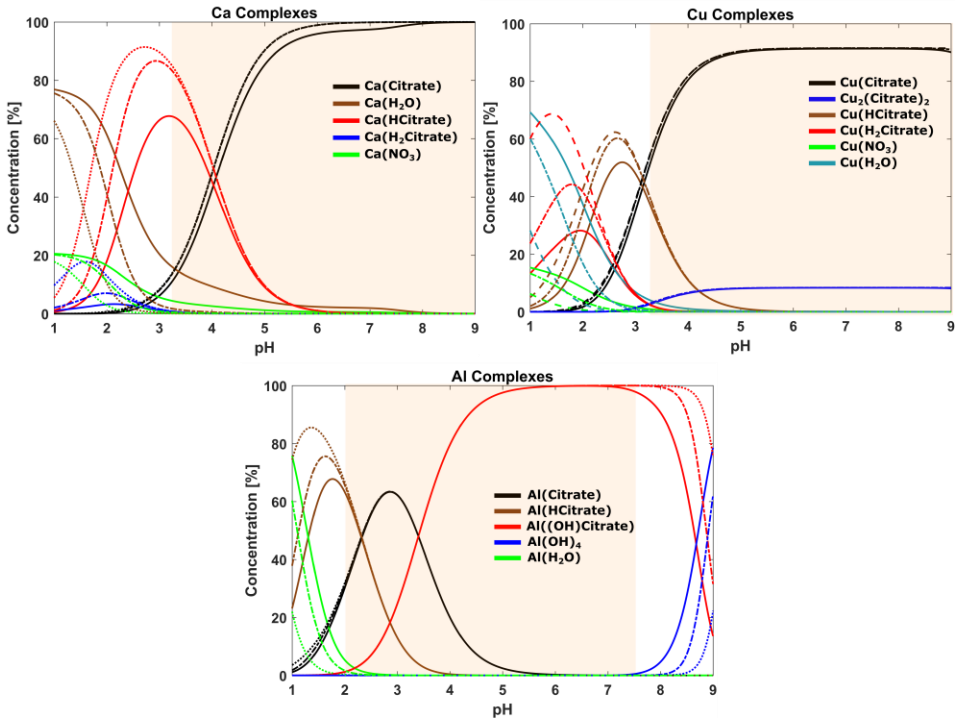

Figure 10 Complex vs. pH diagrams for Ca, Al, and Cu complexes in the amorphous citrate sol-gel synthesis solution of Cu-C12A7. The solid, dash-dotted, and dashed lines represent a 1:1, 2:1, and 10:1 citrate to metal ion ratio, respectively. The highlighted sections identify the range of pH where only cationic citrate species are observed with a 2:1 citrate to cation ratio.

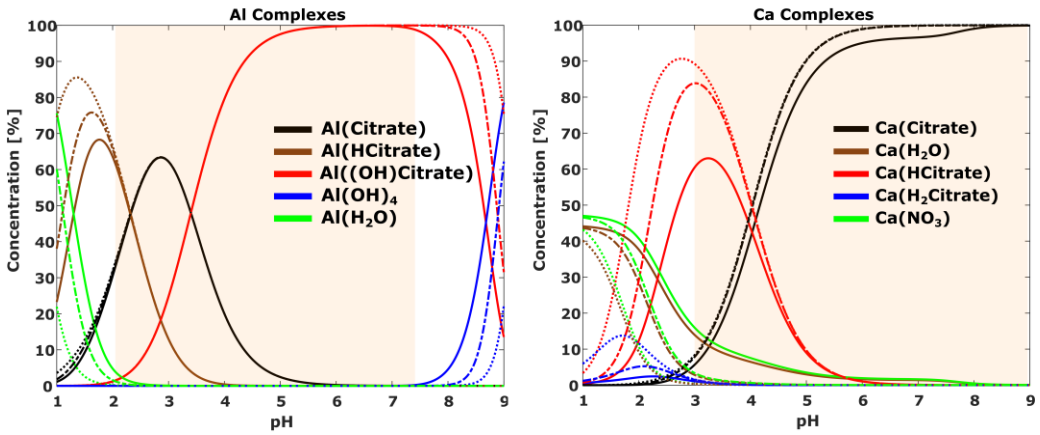

Figure 11 Complex vs. pH diagrams for Ca and Al complexes in the amorphous citrate sol-gel synthesis solution of pure C12A7. The solid, dash-dotted, and dashed lines represent a 1:1, 2:1, and 10:1 citrate to metal ion ratio, respectively. The highlighted sections identify the range of pH where only cationic citrate species are observed with a 2:1 citrate to cation ratio.

likely what causes the non-stoichiometric phases at low temperatures to need higher temperature to allow for cationic diffusion and correcting of the system stoichiometry, resulting in phase purity. The difference in pH range highlights the importance of considering sol-gel chemistry when altering the cationic landscape of the nitrate citrate solution; as the cationic system grows the limitation of individual cationic species limits the cationic system as a whole.

2.3.3 Experimental

In order to assess the effect of pH and solvent evaporation methods for the amorphous citrate method Cu-doped C12A7 will be synthesized by forming a citrate resin precursor at various pH values. The starting materials for the citrate sol-gel technique included $Ca(NO_3)_2 * 4H_2O$, $Al(NO_3)_3 * 9H_2O$, $Cu(NO_3)_2 * xH_2O$, and citric acid ($C_6H_8O_7$). Stock nitrate solutions were created, and the molarity of cations in solution was determined with inductively coupled plasma (ICP) atomic emission spectroscopy. Stochiometric Cu-C12A7 (Al:Ca:Cu) solutions with a Cu content of 1 mol % were combined from the stock solutions into a wide-mouth beaker and heated in an oil bath to 60 °C. Citric acid was added to 50 mL of deionized water with a citric-acid-to-total-cation-molarity ratio of 2:1. Once fully dissolved, the citric acid solution was combined with the nitrate solution. In separate syntheses, the solution pH was either not modified, yielding a natural value <1, or modified to 2 with the aid of ethylene diamine. After an equilibration period, the temperature was raised to 85-90 °C under vigorous stirring to bring about evaporation of the solvent. Once a viscous resin that coated the sides of the beaker formed, the beaker was removed from the oil bath and placed in a 130 °C drying oven overnight (~12 h). Extensive volume expansion was observed due to the evolution

of gaseous species during drying, leading to a porous cake that was subsequently ground into a fine powder.

To raise the pH to 4, the standard slow solvent evaporation procedure could not be conducted due to precipitation. Instead, the solution was prepared identically as above; however, instead of raising the temperature to 85-90 °C, the solution was dripped onto a 250-300 °C petri dish for rapid solvent evaporation. This procedure follows that reported by Narendar and Messing and uses the rapid evaporation to circumvent the kinetics of precipitation.[121] The evaporated brown/black solid was scraped off the petri dish between drops and was dried at 130 °C overnight (~12 h), resulting in little to no observed volume expansion. The resultant powder was ground, forming an analog to the amorphous citrate resin from the previous method. The processes of citrate resin formation are diagrammed in Figure 12.

High-resolution thermogravimetric analysis (TGA) was performed utilizing a Thermal Analysis (TA) Q500 instrument. Characterization of the amorphous citrate resin for Cu-C12A7 and for individual Cu, Ca, and Al cationic citrate resins with solution pH values <1, 2, and 4 was performed. Experimental conditions consisted of ~20 ± 2 mg of pressed powder in 100 mL Pt sample pans under flowing compressed air. Individual cationic resins were synthesized in the exact same procedure as the Cu-C12A7 resins. High resolution analysis utilizing a dynamic ramp rate was performed with a mid-range sensitivity and resolution to gain better insight into the onset temperatures of all four stages of citrate resin decomposition.

In-situ non-ambient high-temperature X-ray diffraction (HTXRD) was performed on a Malvern PANalytical Empyrean diffractometer utilizing an Anton Paar HTK 1200N high temperature furnace sample stage and a PIXcel^{3D} area detector with 255 active channels with ~ 3 °2θ of coverage. Samples were heated to 1000 °C with a ramp rate of 150 °C/h under flowing compressed air (~120 ppm H_2O). Because the purpose of this process was to evaluate kinetic behavior, the data were collected both rapidly at 104 seconds per pattern and continuously during the furnace ramp. A small 2θ range of 28.8-36 °2θ was utilized as it captures the amorphous hump, high-intensity peaks for common secondary phases $Ca_5Al_6O_{14}$ (C5A3), $C_3Al_2O_6$ (C3A), $CaAl_2O_4$ (CA), $CaCO_3$, Al_2O_3, CaO, and Cu oxides, and has three characteristic peaks of C12A7. Reported temperature is the sample temperature and not the set temperature. Instrumental setup and collection specifics are summarized in Table 8 and were optimized for intensity over resolution. The amorphous citrate resin, being predominantly organic, will have a large weight loss during calcination, leading to severe pellet cracking and shrinkage. To avoid this during data collection, the precursor was pressed into a 30 mm pellet and fired to 600 °C with no dwell. By this temperature, the organics have combusted, and a homogeneous amorphous cationic powder remains. The calcined powders were then ground and pressed into 13 mm pellets for HTXRD data collection.

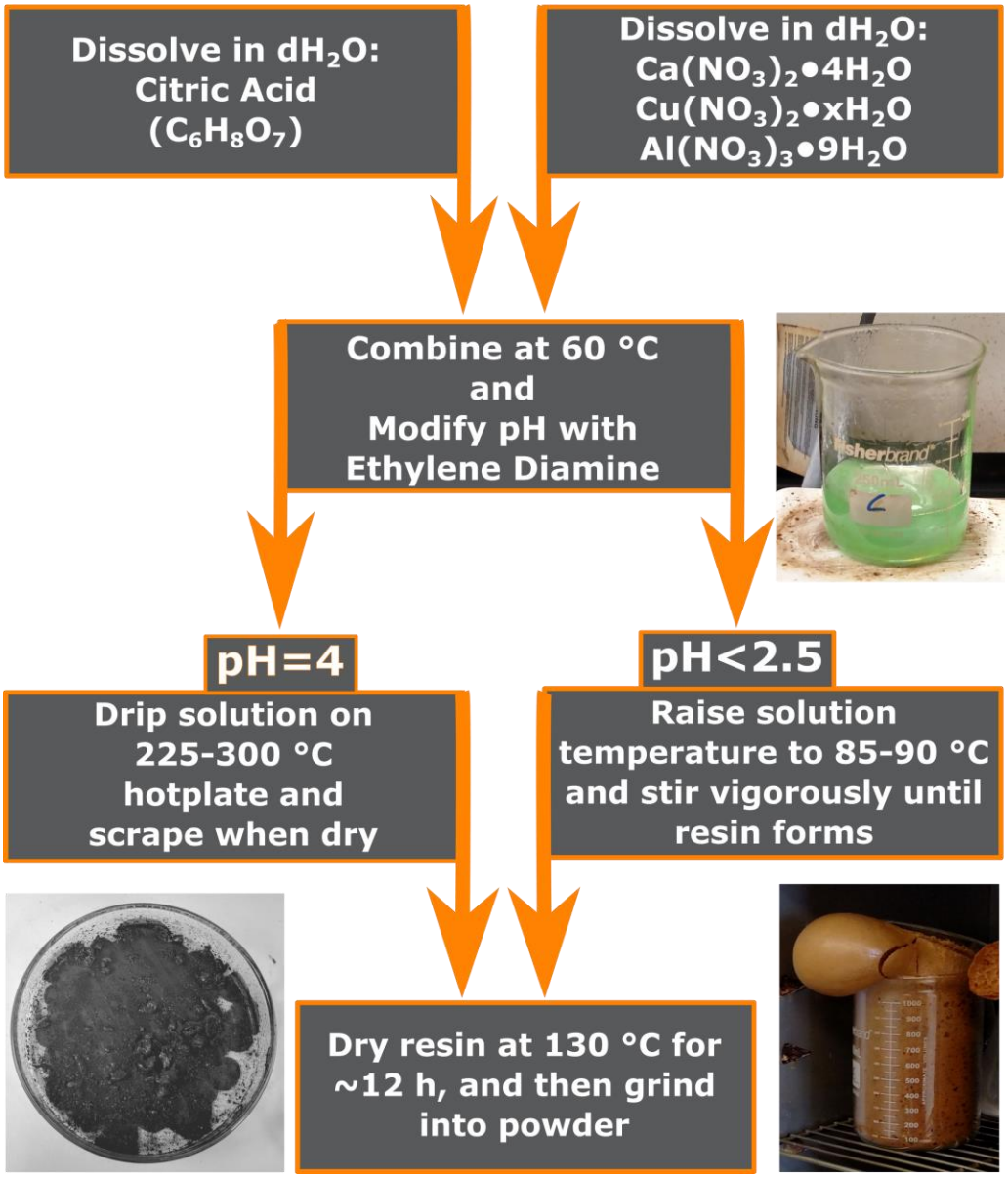

Figure 12 Amorphous citrate resin synthesis flow diagram. Inset images represent the solution during solvent extraction and below the expanded dried resin cake.

Table 8 Instrumental setup and parameters for HTXRD data collection

Instrument Parameters		
Instrument	PANalytical Empyrean	
Source	Cu $K\alpha_1/K\alpha_2$	
Stage	Anton Parr HTK 1200N	
Detector	PIXcel^{3D} area detector	
Mode	Scanning Line Detector	
Active channels	255 (3.3482 °2θ)	
Collimation		
Incident		
Divergence Slit [°]	1/4	
Soller slit [rad]	0.04	
Anti-scatter slit [°]	1/2	
Mask [mm]	10	
Diffracted		
Anti-scatter slit [mm]	5	
Soller Slit [rad]	0.04	
Scan Parameters		
Step Size [°2θ]	0.0131	
Step Time [s]	17.6	
Scan Time [s]	104	
Scan Range [°2θ]	28.8 - 36.0	
Temperatures	Every ~4°C (RT to 1000 °C)	

Phase matching was performed utilizing the International Centre for Diffraction Data (ICDD) PDF-4+ 2018 database. Rietveld refinement was performed in HighScore Plus and refined lattice parameters, background, scale factors, surface sample displacement, phase fractions, and profile parameters relevant to crystallite size determination. Crystallite size was determined through pseudo-Voigt profile fitting and is documented in the HighScore Plus software package as being calculated with Equation 1 and Equation 2, which describe crystallite size and size variance, respectively. W_i and W_{std} are coefficients used to describe peak width for a given reflection i and the standard respectively and $\sigma^2(W_x)$ refers to the variance of those values. Instrumental broadening was characterized with NIST standard SRM 640e (Si), and the refined values were used during the HTXRD Rietveld refinements.

Equation 1 $$D_i = \left(\frac{180}{\pi}\right)\frac{\lambda}{(W_i - W_{std})^{0.5}}$$

Equation 2 $$\sigma^2(D_i) = \frac{\left(\frac{180}{\pi}\right)*\lambda}{(W_i - W_{std})^{0.5}}\left[\sigma^2(W_i) + \sigma^2(W_{std})\right]$$

Characterization of the microstructure was performed via scanning electron microscopy on either a Zeiss EVO MA15 or a Zeiss Auriga 40 scanning electron microscope using a backscattered detector. Electron dispersive spectroscopy (EDS) was performed utilizing a Bruker XFlash 6130 detector for elemental analysis. Samples used for characterization were fired at a temperature just above the formation temperature for all samples, determined by HTXRD to be 900 °C, for 4 h to evaluated microstructural evolution ex-situ. In the case when the pH is naturally <1, additional samples were synthesized at 1100 °C for 4 and 24 h for evaluation of microstructure evolution.

2.3.4 Results

Precipitation was observed during solvent evaporation when the pH of the solution was raised above 2.5. Analysis on individual citrate resins reveals that the precipitant is a Ca complex. Even when the solution was stable at a pH of 4, the precipitant would eventually be observed during an aging period (usually overnight, ~12 h) without solvent evaporation. An increase in the citrate-to-metal-cation ratio to 10:1 led to more stability at a pH of 4 that allowed for conventional solvent evaporation to occur; however, precipitation would occur after ~60% of the solution was evaporated. The precipitant was filtered, rinsed with deionized H_2O, and characterized with XRD. The pattern shown in Figure 13 dominated by a low-2θ reflection, but similarities exist when plotted on a log scale and compared to the calculated pattern for $Ca_3(C_6H_5O_7)_2$ (ICDD reference # 01-084-5956 [122]).The peak positions seem to match well, but there is little agreement between the relative intensities of the characteristic peaks. The strong relative intensity of the (200) reflection suggests preferred orientation. The instability of the cationic citrate solution at a pH above 2 is the motivation for utilizing the rapid drying drip evaporation method when the solution pH is modified to 4. The evolution of cationic complex decomposition as a function of pH was investigated for individual cation citrate resins. High-resolution dynamic rate TGA of the C12A7 and individual cation citrate resins reveals a difference in the expected stage-three decomposition temperatures, as shown in Figure 14. When the solution pH is not adjusted, Cu-C12A7, Ca, and Al resins all show similar behavior with cation-citrate decomposition during stage three at approximately 340-350 °C. The Ca resin shows a slow decomposition during the beginning of stage two, indicating limited reaction between free citrate and uncomplexed nitrates. The Cu-citrate resin deviates from the expected citrate resin decomposition behavior with all decomposition events compressed below 300 °C, indicating intense exothermic decompositions with localized heating.

As the solution pH is raised to 2, the nitrate-citrate decompositions during stage two increase in intensity and magnitude for the Al and Ca resins. The overall behavior during stage two of the Cu-citrate resin changes as well. The decompositions of the Cu-citrate resin are more gradual during stage two, and the bulk of decomposition occurs in stage three in the same temperature regime as the other cations. The reaction is

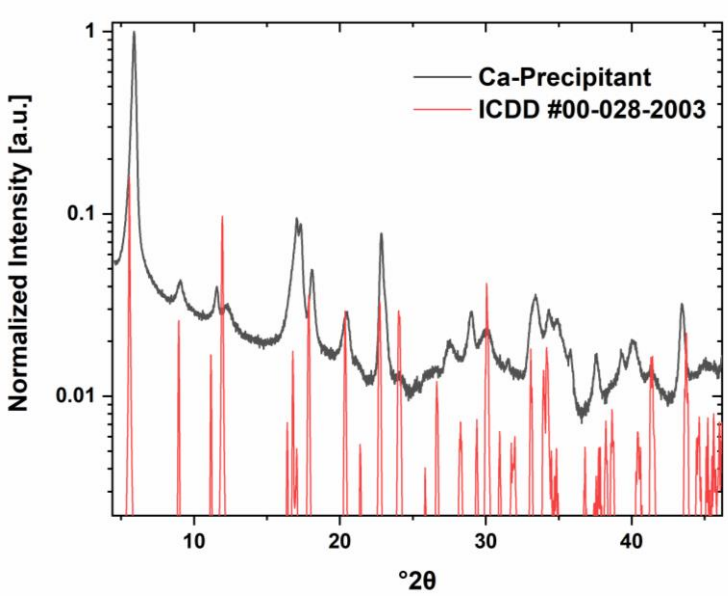

Figure 13 Ca-based precipitant observed when the solution pH is raised above 2.5 and solvent evaporation is performed. XRD pattern for Ca3(C6H5O7)2 is plotted in red for comparison of peak positions and relative intensities.

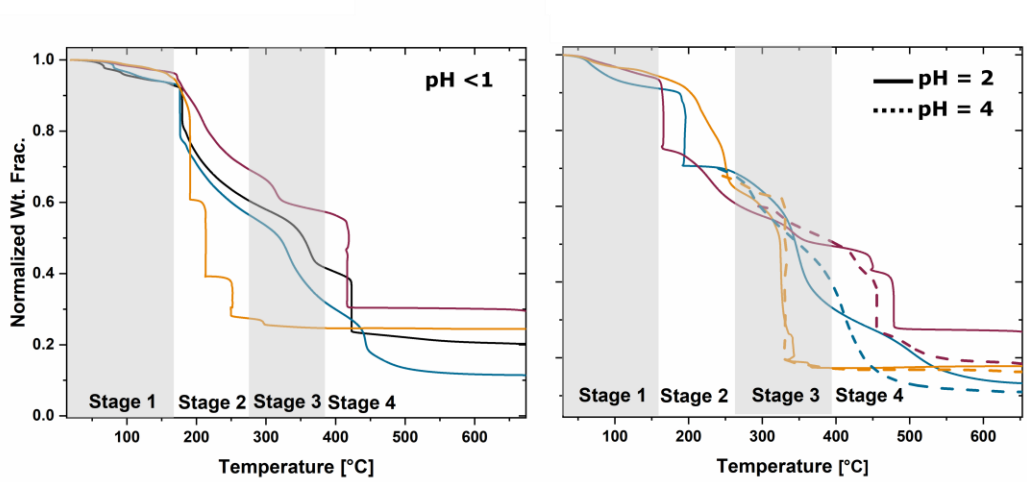

Figure 14 TGA decomposition of Cu-C12A7 and individual cation amorphous citrate resins. (Left) Solution pH is <1 and not controlled. Cu-Cit resin (orange), Ca-Cit resin (red), Al-Cit resin (blue), Cu-C12A7 resin (black). (Right) Solution pH of 2 shown as the solid lines, and solution pH of 4 shown as dashed lines. Due to the change in synthesis style, the pH = 4 samples are pre-decomposed to the temperature of rapid solvent extraction, and the decomposition profiles are scaled to account for this loss of mass for qualitative comparison. Colors remain the same as in the case of no pH control.

intense, introducing local heating and compressing the stage-four organics' decomposition to stage three.

Individual resins at a pH of 4 are produced by rapid solvent extraction at elevated temperatures, causing all resin decomposition up to the evaporation temperature to occur. For a rough comparison, TGA profiles of these resins start at the temperature that the drip evaporation was conducted. The relative intensity is scaled to the expected relative weight loss during solvent extraction. Nearly identical stage-three and -four decompositions are observed for Ca and Cu at pHs of 2 and 4. HTXRD, Figure 15, shows a clear difference as the solution pH is increased. An amorphous hump void of crystalline peaks is initially present, as to be expected with the amorphous citrate resin. A broad peak at approximately 28.8 °C is observed when solution pH is <1, indicating crystallization at 680 °C and increasing in intensity up to ~850 °C.

The peak is characteristic of $CaCO_3$ (ICDD #00-005-0586 [137]). At 870 °C, a noticeable decrease in $CaCO_3$ peak intensity is observed; this is correlated with the crystallization of an unidentifiable phase followed quickly by the formation of C12A7 (ICDD # 01-076-5010) characteristic peaks. No match for these unidentified peaks was found in the ICDD PDF-4+ database. However, the phase was isolated during isothermal HTXRD diffraction experiments; the pattern, peak d-spacings, and areas are shown in Figure 16. As the solution pH is increased to 2, multiple changes are observed in the kinetics. The crystallization of C12A7 is observed starting at 851 °C, which is 19 °C cooler than when the solution pH is <1. The crystallization of $CaCO_3$ is not pronounced on the amorphous background as was previously observed, and relative intensity related to the quantity and lifetime of the unknown secondary phase is decreased. As the solution pH is raised to 4 and drip evaporation is performed, no $CaCO_3$ is observed before C12A7 crystallization. The unidentified phase previously seen when solution pH is either <1 or 2 is not observed. C12A7 peaks are the first

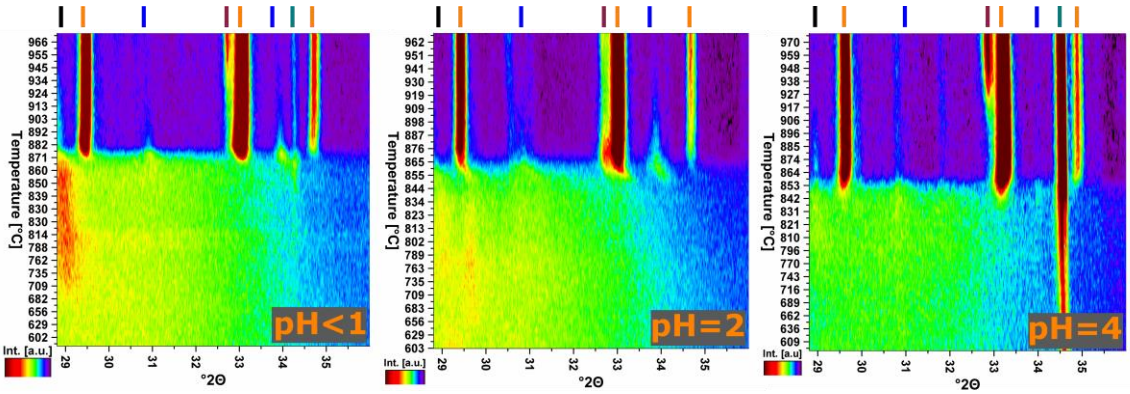

Figure 15 HTXRD phase evolution as a function of temperature. Color is indicative of the diffracted intensity. Phase markers are as follows: $CaCO_3$ (black), C12A7 (orange), C3A (maroon), sample holder (green), unknown high-temperature phase (blue). The Y axis is temperature which is analogous to scan number.

characteristic diffraction peaks observed, and the temperature of crystallization is 838 °C. While no $CaCO_3$ peak was observed on the amorphous hump, a low intensity peak that is barely above the noise of the background is observed, indicating a minor amount of $CaCO_3$ formation during heating. The quantity of $CaCO_3$, however, is sufficiently low enough to not affect the phases or temperature observed during C12A7 crystallization seen in previous reports.[130] The strong peak observed at 34.6 °2θ (green phase marker) before the crystallization of C12A7 is attributed to the sample holder. This peak is also observed, albeit less intense, in the patterns when solution pH is <1.

No characteristic peaks of Cu-containing phases were observed in any data collection, as would be expected with such a low concentration of Cu in the samples. All samples show the presence of the calcium-rich phase C3A (ICDD # 00-008-0005 [138]) at some point in the HTXRD data collection. For a pH of 4 and pH <1, C3A formation is observed around the same temperature of ~930 °C, well after the crystallization of C12A7. This agrees well with the temperature (943 °C) at which Ruszak et al. observed C3A crystallization in solid state synthesis thermodynamic studies, suggesting that the formation is due to incorrect stoichiometry as diffusion of cations is needed to form the off-solution stoichiometric and ordered C3A phase. For a solution pH of 2, C3A is observed to crystallize in conjunction with C12A7, suggesting that diffusion was not necessary for C3A formation and regions of inhomogeneity exist. This indicates that precipitation of a Ca-citrate phase was not avoided and likely occurred during the final stages of resin formation when solvent concentration was low.

The off-stoichiometry is attributed to a systematic error in either the molarity of Ca starting solutions or the method for which cationic solutions were appropriated and has no observed impact on the derived results. The systematic error actually increases the information obtained from the kinetic studies by highlighting the preferential kinetic formation pathway regardless of cation stoichiometry.

Characterization of peak shapes and positions yields crystallite size and lattice parameter, respectively, for Cu-C12A7, Figure 17. Lattice thermal expansion is traditionally observed in thermodynamic studies of C12A7; however, a decrease in the lattice parameter eventually plateaus during the kinetic investigation of the crystallization of C12A7.[50] The observation of cell contraction has also been observed isothermally at much higher temperatures (1400 °C) when synthesizing from solid state synthesis reactants.[65] The plateau decreases as a function of process pH from ~12.085(2) Å to ~12.071(4) Å and ultimately ~12.052(1) Å at a process pH of <1, 2, and 4, respectively. Grain size, assuming in this case a crystallite is a grain, increases as a function of temperature; however, the grain growth rate decreases as the pH is raised, and the ultimate crystallite size is 30% smaller (~78 nm) one hour after crystallization when the solution pH is raised to 4.

Microstructural characterization shows an evolution of crystallite size and the presence of a Cu-rich secondary phase as a function of process pH. When a solution

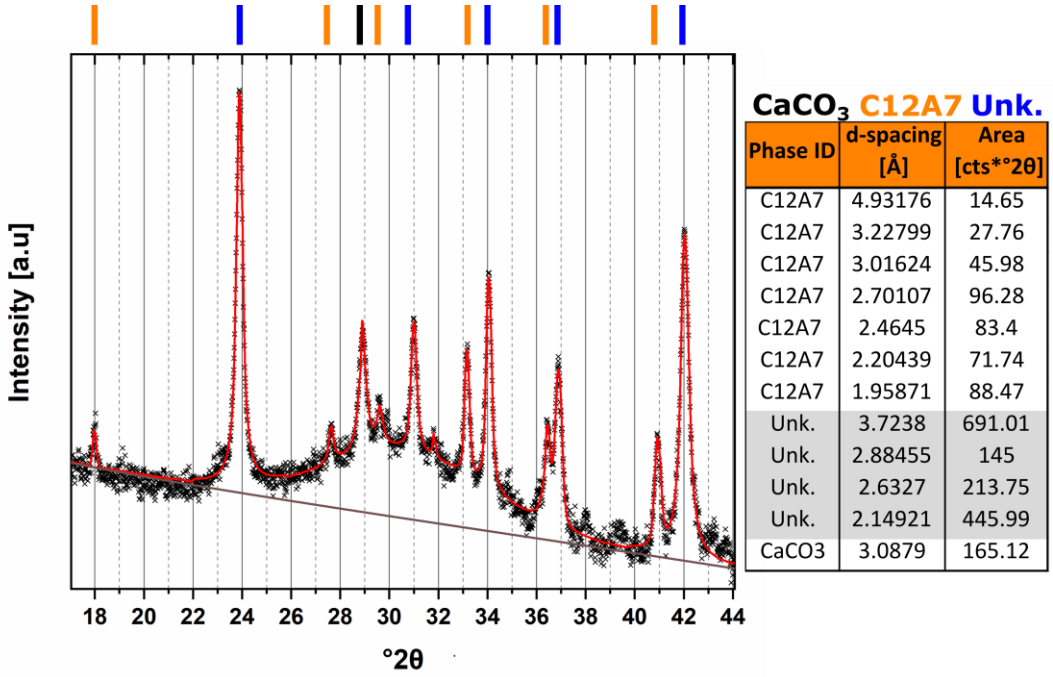

$CaCO_3$ C12A7 Unk.

Phase ID	d-spacing [Å]	Area [cts*°2θ]
C12A7	4.93176	14.65
C12A7	3.22799	27.76
C12A7	3.01624	45.98
C12A7	2.70107	96.28
C12A7	2.4645	83.4
C12A7	2.20439	71.74
C12A7	1.95871	88.47
Unk.	3.7238	691.01
Unk.	2.88455	145
Unk.	2.6327	213.75
Unk.	2.14921	445.99
CaCO3	3.0879	165.12

Figure 16 The unidentified high temperature calcium aluminate phase, identified in high temperature kinetic XRD studies, shows characteristic peaks in the area of interest in conjunction with characteristic peaks of C12A7 and $CaCO_3$. Observed data are represented in markers, peak fitting summary in red, and the background in brown. A broad peak was used to model the amorphous hump. The unknown phase peaks are represented by blue, C12A7 by orange, and $CaCO_3$ by black phase markers. Peak assignment, d-spacing, and area are tabulated in the accompanying table.

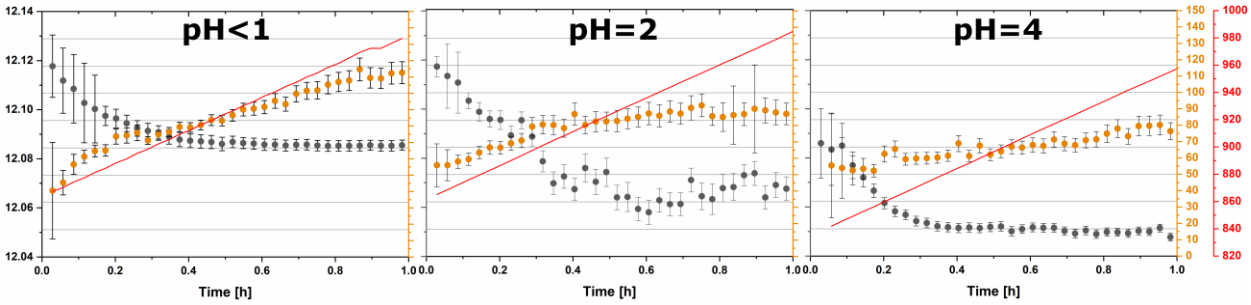

Figure 17 Refined lattice parameters and crystallite sizes as a function of time and temperature for HTXRD characterization of Cu-C12A7 with solution pH of <1, 2, or 4. Lattice parameters are represented in [Å] in black and crystallite sizes in [nm] in orange. Since observed temperature may have deviated non-linearly, all plots are plotted with time from crystallization as the independent variable, and the temperature is represented by the solid red line in units of [°C]. All errors are reported as 3σ and are significant due to the limited characterized d-spacing range and rapid data collection. All plots are shown on identical dependent axis ranges for easy comparison.

that has a pH of <1 is fired for 4 h at 900 °C, bright precipitates are observed on top of a fine-grained (~150-200 nm) C12A7 microstructure, Figure 18. Contrast when utilizing aback scattered electron detector is indicative of atomic number. As the temperature is raised to 1100 °C for 4 h, grain growth to the micron scale is observed and the bright secondary phase occupies grain boundary triple points. EDS analysis indicates that this bright secondary phase is Cu rich. As the temperature is raised to 1100 °C for 24 h, the secondary phase migrates out of the triple points to surround the grains and qualitatively appears to decrease in quantity. As the pH is raised to 2, bright Cu-containing phases are still observed, but the overall concentration is qualitatively decreased. A fine-grained C12A7 microstructure is still observed. No bright Cu-containing phases are observed when the pH is raised to 4, and a homogeneous fine-grained microstructure (60-100 nm) is observed that is similar to the grain size characterized by XRD after 1 h suggesting limited grain growth.

2.3.5 Discussion

To ensure optimal control over final product phase purity and microstructure, chemical homogeneity needs to be maintained in the solution, in the resin, during resin decomposition, and prior to crystallization. The results show that a pH adjustment to 4 with rapid solvent extraction is necessary to obtain a homogeneous and fine-grained Cu-C12A7 powder.

Solution and derived citrate resin homogeneity requires the formation of cationic citrate complexes. The optimal solution parameters, such as L:M ratio and pH, for synthesis are determined by calculating theoretical complex diagrams. The calculated complex diagrams indicate an increase in citrate-based complexes in the pH range of 4-7 with the largest benefit given to Cu and Ca species. Increasing the L:M concentration to 2:1 further increases the formation range of citrate species due to the higher affinity and availability of free citrate.

Both a decrease of nitrate-complexed cations and an increase in the availability of free nitrate should occur with this increase in citrate-based complexes. As the pH is raised to 2, the Ca-citrate resin shows an intense decomposition during stage two that was not observed when the pH was <1. This indicates a decrease in the concentration of $Ca(NO_3)_2$ species and an increase in the concentration of nitrate species available for combustion with citric acid. This decrease in the concentration of Ca nitrate complexes is corroborated in the HTXRD characterization. $CaCO_3$ formation is suppressed with an increase in solution pH, and the suppression of alkali earth carbonates has previously been correlated with a decrease in nitrate species. In Ba-containing amorphous citrate systems, Lee and Fang found that suppressing $Ba(NO_3)_2$ by increasing solution pH led to a decrease in observed $BaCO_3$ as a precursor phase to final phase crystallization.[131] Ca demonstrates the same behavior, and it can be inferred that the lack of observed $CaCO_3$ as a function of pH increase is due to a suppression of Ca nitrate species in the amorphous citrate resin.

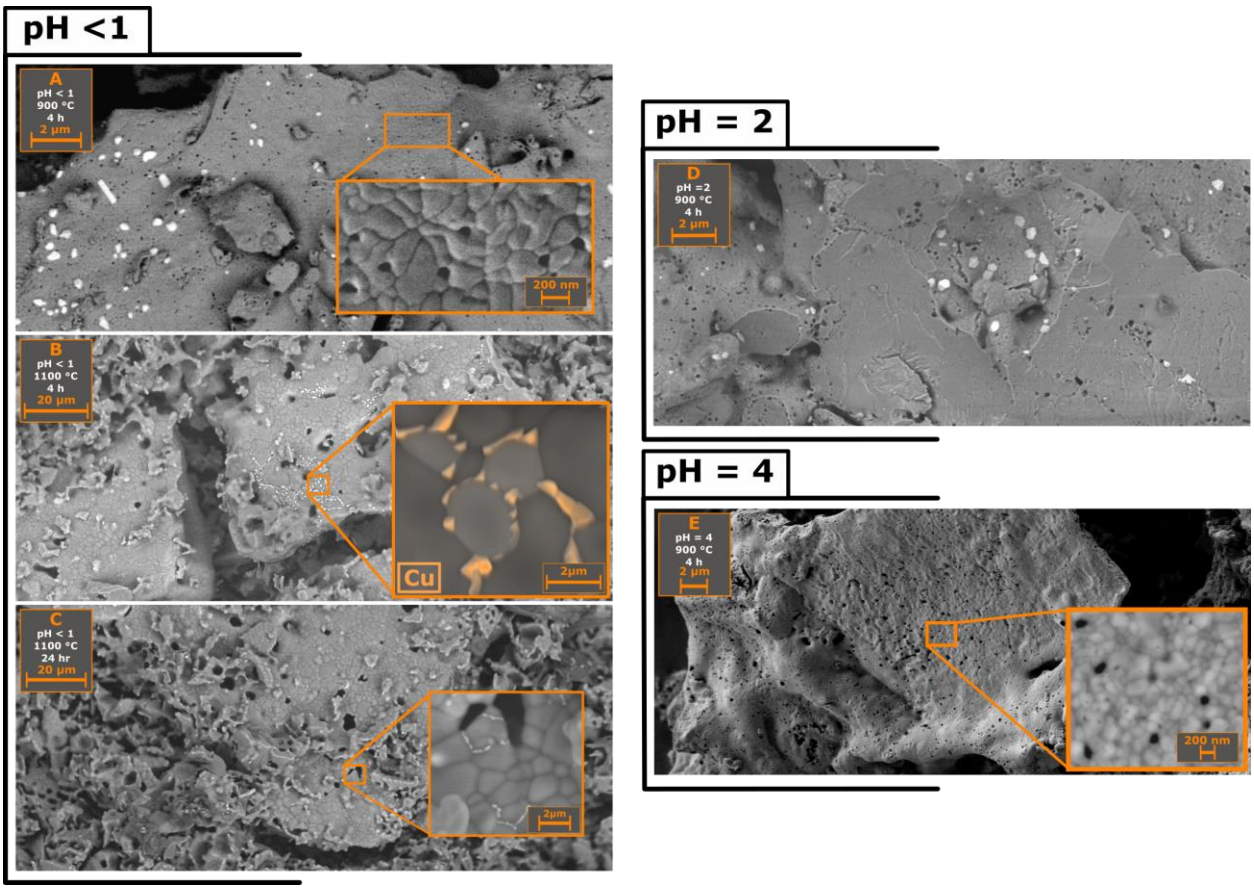

Figure 18 SEM characterization of Cu-C12A7 processed for various temperatures, times, and solution pH. (Left) When solution pH is not controlled, characterization was performed on samples fired at 900 °C for 4 h (A), 1100 °C for 4 h (B), and 1100 °C for 24 h (C). Insets show high-magnification images and EDS results, identifying Cu as orange, for the characterization of a sample fired for 4 h at 1100 °C (B). (Upper-right) Microstructure when solution pH is raised to 2 and the sample was fired for 4 h at 900 °C (D). (Lower-right) Microstructure when solution pH is raised to 4 and the sample was fired for 4 h at 900 °C (E).

The decrease in $Ca(NO_3)_2$ is observed to change the decomposition profile of the resin and has an effect on the homogeneous crystallization of the desired phase. C12A7 crystallization is dependent on the availability of CaO that then combines with aluminum species to form C12A7. The suppression of $CaCO_3$ as the pH is raised to 4 leads to a decrease in crystallization temperature due to the lack of time needed for the kinetic decomposition of $CaCO_3$ to CaO. When $CaCO_3$ concentration is significant, the kinetics of decomposition will occur over a longer duration, precluding Ca species from interacting with neighboring cationic oxides and resulting in temporary regions of incorrect stoichiometry. The unidentified secondary phase could be due to this incorrect stoichiometry and is likely a calcium aluminum oxide with slightly poor Ca stoichiometry from C12A7. As the $CaCO_3$ continues to decompose, the increasingly-available Ca combines with the unknown phase to form C12A7.

Solution modification becomes increasingly necessary as the cationic system increases in size and transition metal dopants are added. In the case of Cu, a lack of solution pH leads to poor citrate resin formation, intense decomposition, and exclusion from the C12A7 structure. The large difference in cationic radii between Ca and Cu prevents Cu inclusion at low temperatures unless kinetically favorable; this is achieved with an increase in atomic homogeneity. The transition metal easily changes its oxidation state in the local reducing environment of combustion, providing an increase in available nitrates and further promoting the combustion reaction between nitrate oxidizers and citrate fuel. This reduction is the source of the intense decomposition observed in stage two with no pH control. An increase in pH changes the observed decomposition behavior from being intense and early in stage two to occurring during stage 3. With the gradual decomposition during stage two, the localized reducing atmosphere and local heating is minimized, providing resin stability until stage 3 when resin decomposition is observed concurrently with Al and Ca resins. Full resin homogeneity is not expected until above a pH of 3, and Cu secondary phases are observed at a solution pH of 2, indicating that full atomic homogeneity is not achieved.

At a solution pH of 4, a microstructure free of a Cu secondary phase is observed, suggesting Cu inclusion into the C12A7 phase due to the full homogeneity of the citrate resin. This is further corroborated by characterization of the C12A7 high-temperature lattice parameter where a decrease from ~12.085(2) to 12.052(1) is observed as pH increases from <1 to 4, respectively. The lattice parameter of C12A7 changes linearly as a function of dopant cationic radii for a large set of cationic dopants and replacing the large Ca with a Cu cation leads to a decrease in lattice parameter. DFT theoretical calculations predict a smaller change in lattice parameter (12.07 to 12.059 Å); however, experimentally observed changes in lattice parameter (11.998 to 11.97 Å) through solid state techniques exhibit a similar change to that observed here.[1,139] Cu inclusion into C12A7, characterized by a decrease in lattice parameter and Cu-secondary phase concentration, increases as the solution pH. The increase in pH results in the use of the rapid solvent extraction method which further protects homogeneity during decomposition as it ensures that the bulk decomposes rapidly and homogeneously

without localized heating. It is not until full Cu-citrate complexes are expected by the complex diagrams that the microstructure is free of Cu-secondary phase.

While homogeneity can remain through resin decomposition, the desired phase must be kinetically favorable to form as cationic diffusion is sluggish and thermodynamic influences are not yet a contributing factor. Previous thermodynamic studies have characterized the formation of C12A7 through solid state synthesis.[65,66,140] The formation pathways of C5A3 + C3A and CA + C3A are observed at low (900-1100 °C) and high temperature (>1100°C), respectively. The lower temperature of synthesis through sol-gel techniques has been assumed to be due to the low-temperature pathway.[66] Kinetic non-ambient XRD reveals that this is not the case and that direct crystallization of C12A7, in the case of Cu-doping, is observed when cation homogeneity is high even if the precursor is off stoichiometric from C12A7. This is expected as C12A7 is highly disordered with a large amount of crystallographic void space due to the clathrate structure. The amorphous citrate process has the advantage of a near atomically homogeneous precursor that is beneficial for formation of a disordered, low-density crystal structure in which needed diffusion pathways are short. C5A3 ($\rho_{theoretical}$ = 3.067 g/cm^3) is an ordered layered structure, and C3A ($\rho_{theoretical}$ = 3.064 g/cm^3) and CA ($\rho_{theoretical}$ = 2.94 g/cm^3) have a higher density than C12A7 ($\rho_{theoretical}$ = 2.68 g/cm^3).[23,141,142] These phases are less likely to crystallize at these lower temperatures due to incorrect local stoichiometry leading to longer diffusion pathways required to create dense ordered crystal structures. This is observed as the crystallization of C3A requires elevated temperatures compared to C12A7.

The kinetics of crystallite growth, assumed to be the same as grain growth, show an evolution as a function of temperature and time. The magnitude of crystallite size and rate of crystallite growth is reduced as solution pH is increased. A decrease in grain growth could be due to altering the kinetics to reduce grain boundary mobility or thermodynamically reducing the driving force. The phenomenon is complicated and there is still no universal theory after almost a century of investigation. A kinetic reduction in mobility could be due to nanoinclusions, nanopores, triple junctions, and/or quadruple points.[143] The comparison of microstructures between a pH <1 and 4 show no nanoinclusions and have similar concentrations of nanopores, triple junctions, and quadruple points, which explains the stability of the grain structure with an increased processing time of 4 h. This does not account for the difference in growth rate between the samples, and a possible explanation for the difference could be the narrowing of the distribution of particle sizes.[144] As the grain sizes become similar and the grain boundary curvatures become equal, the gradient across the grain boundary decreases and both grains are at an equal energy state. Theoretically, it was determined that a decrease in the standard deviation of grain size leads to an increase in the growth exponent and a decrease in grain mobility.[144] A tighter distribution of particles is to be expected with an increase in atomic homogeneity as nucleation occurs evenly and no crystallization time is expended waiting for cationic diffusion for nucleation. This explanation of the reduction in grain growth and its correlation to an increase in atomic

homogeneity supports the importance of modification of solution pH to 4 and implementation of rapid solvent extraction.

2.3.6 Conclusions

Theoretical complex vs. pH diagrams were calculated based on available stability, or formation, constants to predict the formation of cation citrate complexes as a function of pH. In the Ca-Al-Cu-citrate system, an increase in pH and ligand-to-metal ratio leads to the full complexation of Ca and Cu citrate complexes. The optimal process values of 2:1 and a pH of 4-6 were determined. During experimental modification of solution pH, precipitation of Ca-citrate complexes was observed but was not predicted in our complex diagrams due to the lack of reported formation constant. Rapid solvent extraction was employed to avoid this precipitation, circumventing the kinetics of precipitation and yielding a precipitate-free amorphous resin.

Experimental characterization of the effects of solution pH and rapid solvent extraction on the synthesis of Cu-C12A7 corroborates theoretical complex diagrams. The increase of solution pH leads to a higher degree of homogeneity in the solution and dried resin, during decomposition of citrate complexes, and in the formation of the desired Cu-C12A7 phase. This increase in homogeneity yields a Cu-doped C12A7 powder 70 °C lower than that previously reported due to an increase in atomic homogeneity and circumvention of significant $CaCO_3$ formation during heating previously observed in the standard amorphous citrate synthesis. The decrease in temperature, increase in homogeneity, and decrease in firing time yields a fine-grained powder with an average crystallite size of approximately 78(3) nm which is 30% smaller than when solution pH and solvent extraction is not modified. The results reported here fundamentally changes the approach to the citrate-based sol-gel synthesis of C12A7 allowing for better control and optimization of powder morphology. Previous reports attempt to circumvent $CaCO_3$ formation by calcining and firing in controlled atmospheres and a simple alteration to the starting solution pH solves this problem without the need for complicated processing. This is ultimately the goal of implementing a sol-gel synthesis procedure rather than solid state synthesis and the results presented here for the Cu doped system likely extend to the parent undoped system. With a controlled morphology and successful Cu inclusion, an increase in performance of Cu-C12A7 for catalytic activity and electrically conductive oxide applications is achieved.

The kinetic formation pathways reported here deviate from that observed in thermodynamic studies. The benefit of rapid data collection allows for precise determination of formation pathways when atomic homogeneity is high. No C5A3 was observed during crystallization and C12A7 was the first product to form when $CaCO_3$ formation is avoided even if cationic stoichiometry is off. This observation is a fundamental shift in the discussion on formation kinetics and pathways of C12A7.

2.4 Polymer Assisted sol-gel Synthesis of Cu-doped $Ca_{12}Al_{14}O_{33}$

2.4.1 Introduction

The amorphous citrate, or more broadly small molecule sol-gel, synthesis techniques relies on the bonding between the cationic species and small molecules to retain homogeneity during resin formation. As the resin is calcined these weakly interacting metal ligand complexes decompose, and metal-oxide based species remain. When this occurs slowly, locally, or at temperatures much lower than the desired phase formation temperature the possibility for evolved inhomogeneities to occur increases. In the previous amorphous citrate synthesis method, the solution pH was modified to ensure that metal ligand complexes were formed and gel decomposition was controlled to ensure homogeneous calcination. Lack of process engineering resulted in inhomogeneous decomposition and metal complexes altering the observed synthesis kinetics and final powder morphology. $CaCO_3$ formed prior to C12A7 crystallization due to the presence of $Ca(NO_3)_2$ in the resin ultimately leading to heterogenous phase crystallization. Dopant incorporation was hindered due to a combination between a lack of dopant ligand complexation and inhomogeneous gel decomposition leading to local reducing atmospheres. The sol-gel process relies on chemical and decomposition control.

This investigation utilizes poly-vinyl alcohol (PVA) in a polymeric assisted sol-gel synthesis technique to transfer atomic level solution homogeneity to the formation temperature of $Ca_{12}Al_{14}O_{33}$ or C12A7. PVA synthesis of C12A7 allows better phase purity and process control. The in-situ polymerization Pechini and amorphous citrate sol-gel synthesis are most common in the C12A7 literature and are antiquated and ill-purposed techniques. The polymer of choice is PVA which is widely available industrially making it a low-cost synthesis method. Dissolved polymer chains provide structure during gelation creating a dense net of interconnected polymer branches [114]. This long-range polymer structure, compared to weak hydrogen interactions of the amorphous citrate complexes, leads to steric entrapment of metal cation complexes preventing diffusion and cationic interaction. Chemical interactions between cation complexes and OH^- functional groups, carboxylate moieties, and nitrogen lone pairs further adds a component to retain homogeneity [114,117,145]. An added benefit of the polymer is the ability to spatially distribute ionic charges evenly and interact with multiple cationic species on the same functional groups. This leads to localized areas of intended stoichiometry providing ideal nucleation points without the need for cationic diffusion. The combination of chemical interaction and steric entrapment prevents metal oxide formation and agglomeration until polymer decomposition. Further, since the PVA polymers are interacting with multiple cations, and no individual cation PVA complexes are being formed, the polymer will decompose homogeneously preventing localized decomposition as observed in the amorphous citrate process. The ability for multiple cations to interact with one PVA monomer leads to lower organic contents and higher oxide yields [145]. Once near the decomposition temperature the polymer network starts

to decompose in a non-combustive manner creating a liquid like state and allowing for liquid phase diffusion of cationic species increasing cationic homogeneity [145]. The polymer assisted sol-gel synthesis increases homogeneity during all stages of resin formation and decomposition due to the inherently different nature of the organic component.

With the polymer method, and more specifically the PVA method employed here, there are two fundamental variables to be chosen. The first is the starting molecular weight of the polymer and the second is the ratio between OH^- functional groups and metal cations; the ratio between $OH^-$and cations can be represented as a ratio of PVA monomer to cation molarity (PVA:Cations) since each monomer of PVA has one hydroxyl group. The degree of polymerization (DP) is a measure of the length of a polymer chain and is calculated by dividing the weight of an average chain by the weight of a single monomer. Optimizing chain length improves the efficiency of the synthesis by decreasing waste materials and reducing the diffusion path of the metal cations in the final powder. If a high molecular weight polymer is used, then the diffusion paths between cationic species will be large but steric entrapment will be better due to long cross-linked polymers acting as a diffusion barrier. When the molecular weight is low the cations are evenly distributed, but the steric entrapment of the polymer net is reduced. Increasing the ratio of PVA:cations while decreasing molecular weight, to decrease diffusion pathways, can offset the lower cation stability during decomposition [117]. For synthesis the molecular weight vs PVA:cations concentration needs to be balanced and some methods use a filter to ensure all polymer chain lengths are of the desired length [145].

Once the amorphous cation-PVA powder is obtained it is converted to the oxide phase through calcination. Like the amorphous citrate resin the PVA decomposition occurs in stages. At lower temperatures the evaporation of nitrate and hydrogenous species from the precursor powder occurs. Dehydration of the PVA structure occurs generally in the range between 240 - 340 °C; the exact temperature is based on the impurities present in the polymer [146,147]. As dehydration occurs the polymer chains decomposes into polyenes which ultimately decompose into carbons and hydrocarbons at approximate 450 °C. These remaining carbon based compounds then go through oxidative decomposition at temperatures between 500 - 600 °C [148].

In this report we analyze the synthesis of Cu and pure C12A7 through the PVA precursor technique. A medium molecular weight PVA powder is utilized and the ratio of polymer to cations, correlated to the concentration of OH^-interacting sites, is investigated; the optimal ratio is the used to characterize the kinetic formation pathways of Cu-doped C12A7 via the polymer assisted sol-gel route.

2.4.2 Experimental

The cationic sources and polymer used for the polymer assisted sol-gel technique included $\mathrm{Ca(NO_3)_2 * 4H_2O}$, $\mathrm{Al(NO_3)_3 * 9H_2O}$, $\mathrm{Cu(NO_3)_2 * xH_2O}$, and poly vinyl alcohol

($[CH_2CH(OH)]_n$). Stoichiometric amounts of cations were measured from stock cation nitrate solutions, created with high purity nitrate salts and deionized water, whose molarities were confirmed through inductively coupled plasma (ICP) spectroscopy. Acros Organics Poly(vinyl alcohol), 88% hydrolyzed with an average molecular mass of 20,000-30,000 $g \cdot mol^{-1}$ was used. The PVA with a PVA:cation ratio of 1:2, 1:4, or 1:8 was weighed and then mixed vigorously into deionized H_2O for 12 h. This solution was combined with the nitrate solutions and allowed to homogenize under vigorous stirring for 1 h prior to heating the hotplate raising the solution temperature to 90 °C. The evolved behavior of solvent evaporation depended on the PVA:cation ratio, but all ratios resulted in a dry powder or cake which was then ground and pressed into 30 mm pellets with 1800 lbs of force. For high temperature X-ray Diffraction (HTXRD) characterization, and ultimately for direct synthesis, the PVA powder was calcined to 600 °C and immediately quenched. The resultant white powder is the starting precursor for direct synthesis. A summary of this process is provided in Figure 19.

High-resolution thermogravimetric analysis (TGA) was performed utilizing a Thermal Analysis (TA) Q500 instrument. Thermal decomposition of the 1:4 PVA:cation powder was performed for comparison to the amorphous citrate resins. Experimental conditions followed that in the amorphous citrate section, section 2.3.3**,** consisting of ~20 ± 2 mg of pressed powder in 100 mL Pt sample pans under flowing compressed air.

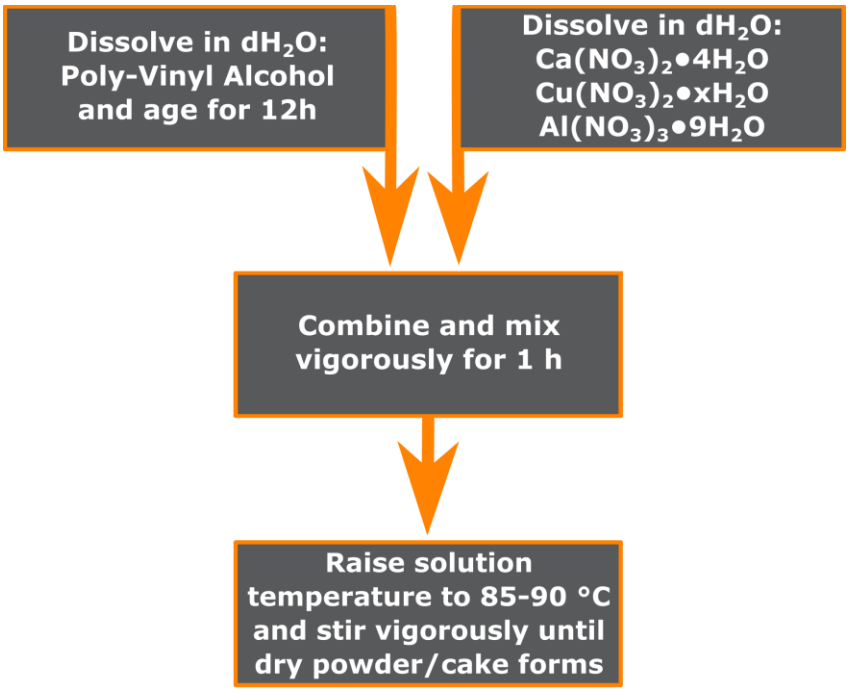

Figure 19 Flow diagram for the synthesis of C12A7 via a polymer assisted sol-gel route using poly-vinyl alcohol to retain solution homogeneity.

The same mid-range sensitivity and resolution was utilized.

X-Ray Diffraction (XRD) with Cu-kα radiation was used for thermodynamic equilibrium phase characterization and non-ambient in-situ diffraction was used to characterize kinetic pathways. XRD was performed on a Malvern PANalytical Empyrean diffractometer utilizing an Anton Paar HTK 1200N high temperature furnace sample stage and a PIXcel^{3D} area detector with 255 active channels with ~ 3 °2θ of coverage. Samples were heated to 1100 °C with a variable ramp rate of 300 °C/h in areas not of interest and 150 °C/h in areas of kinetic transformation. Flowing dry compressed air (~120 ppm H_2O) was circulated in the environmental furnace chamber used during the in-situ experiment. The same amorphous citrate collection procedure and instrumental collimation was implemented characterizing a small 2θ range of 28.8-36 °2θ with rapid data collection of ~104 seconds per pattern. The reported temperature is the sample temperature and not the set temperature.

Phase matching and Rietveld analysis were performed in the same manner as the previous section, section 2.3.3**,** providing refined lattice parameter, crystallite size, and quantitative phase amounts along with estimated standard deviations. Additional analysis was performed through pseudo Voight peak fitting of the C12A7 (024) reflection to characterize the increase in area during crystallization. The ultimate peak area was assumed to indicated full crystallization and corresponds to a 100 wt.% when only C12A7 characteristic peaks are observed.

Characterization of the microstructure was performed via scanning electron microscopy (SEM) on a Zeiss Auriga 40 scanning electron microscope using a backscattered detector. Samples used for characterization were fired at 900 °C for 4 h.

2.4.3 Results

The behavior of the PVA nitrate solutions changed as a function of PVA:cation ratio. Solutions with a 1:2 ratio exhibited auto-combustion during evaporation resulting in a black carbonaceous fine-grained powder. A 1:4 ratio exhibited substantial gas evolution during dehydration, due to nitrate decomposition, and resulted in a yellow fine powder and no combustion was observed. Solutions with a ratio of 1:8 had less of an evolution of gaseous phases and a mint/blue color was observed which is assigned to the precipitation of cation nitrate species during solvent evaporation.

Thermogravimetric Analysis (TGA) of a 1:4 Cu-C12A7 PVA powder shows three major decomposition stages. The first, from 100 to 300 °C, attributed to H_2O and volatile evaporation. As the PVA is heated, polymer condensation reactions occur and H_2O that was trapped in the structure is released leading to the formation of polyenes [3]. Between 300 and 400 °C, the polymers formed during the condensation reactions decompose. The large weight loss after 500 °C is likely due to the decomposition of the remaining organics and carbonaceous residue left by the polymer decomposition [4]. When compared to the amorphous citrate decomposition profile PVA decomposition consists of less intense gradual decompositions retaining organic matter until 100 °C

higher and the final mass of inorganic material is ~48 wt.% rather than ~20 wt.%, Figure 20.

XRD characterization of the PVA precursor powder obtained after solvent evaporation shows a difference in cation stability, Figure 21. Pure C12A7 precursors are amorphous once the PVA:cation ratio is increased above 1:4. When the ratio is 1:8 characteristic nitrate peaks are observed above the amorphous background. In the case of Cu-C12A7 full stability is only observed above a ratio of 1:4, however, the characteristic nitrate peaks are much less intense and dominated by the amorphous background.

To assess how the lack of cation segregation, that occurs at a PVA:Cation ratio of 1:8, and excess polymer, that occurs at a PVA:Cation ratio of 1:2, effects the final phase products the thermodynamic state achieved after firing at 900 °C for 4 h was analyzed using XRD and is shown in Figure 22. In all cases, including both pure and Cu-doped C12A7, C12A7 is the dominant phase. Both the 1:8 and 1:2 PVA: Cation ratios exhibit calcium aluminate secondary phases with the fraction of C12A7 increasing as a function of polymer content. In the synthesis of pure-C12A7, with a PVA:Cation ratio of 1:4, C12A7 is accompanied by C5A3 which is close in stoichiometry and related to instability of the C12A7 framework. Previous investigation, and future investigation in,

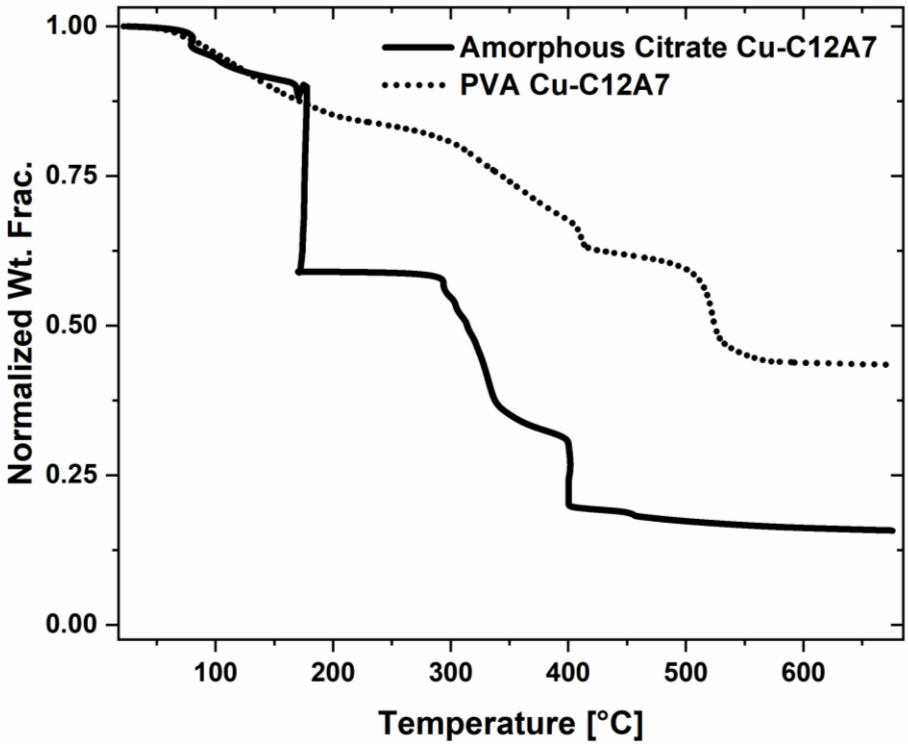

Figure 20 Comparative decomposition of Cu-C12A7 PVA powder with a PVA:Cations ratio of 1:4 (dashed line) and amorphous citrate powder (solid-line).

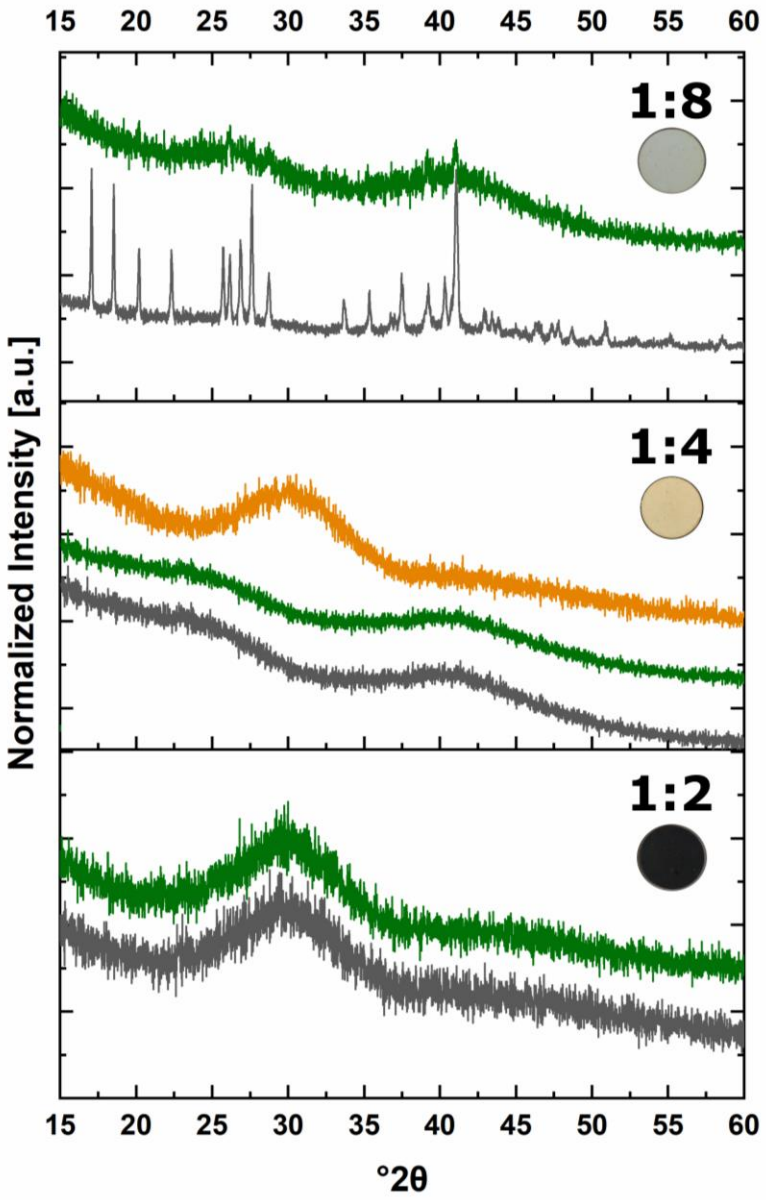

Figure 21 XRD data obtained on PVA powders after solvent evaporation. PVA:Cation ratio is noted and is either 1:8, 1:4, or 1:2. Data from samples doped with Cu are shown in green while data from undoped or pure C12A7 are shown in gray. The orange data demonstrates the change in amorphous behavior as the 1:4 Cu-PVA powder is calcined to 600 °C and quenched. The circular insets are images of the dried PVA powder after solvent extraction.

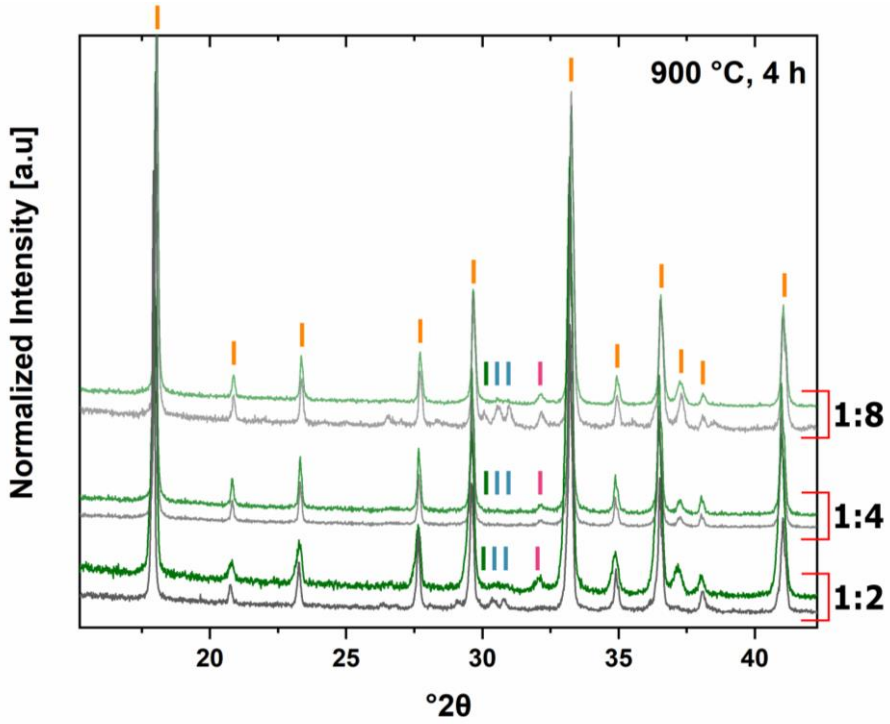

Figure 22 XRD data of fired PVA powder as a function of PVA:cation ratio and dopant. All samples were fired directly at 900 °C for 4 h. Phase markers represent C12A7 in orange, CA in green, C5A3 in blue, and CaO in pink. Cu C12A7 is plotted in green and pure C12A7 is plotted in gray.

section Error! Reference source not found., indicates this likely formed after formation o f C12A7 and is a function of the processing environment during synthesis [10]. The lack of non-stochiometric phases suggest that 1:4 is the optimal ratio for pure-C12A7 synthesis. In the case of Cu-C12A7 99 wt.% phase purity was achieved with a ratio of 1:4 and no C5A3 phase formation was observed.

The thermodynamic studies give little insight into the changes in kinetic formation, but the final phases assembly does indicate the behavior of the kinetic formation pathways have little effect on the thermodynamic equilibrium. Kinetic studies of C12A7 synthesis through in-situ XRD characterization reveal the crystallization temperature, microstructural evolution, and kinetics of phase formation. This study was performed on samples synthesized with the 1:4 PVA:Cation ratios since they were observed to yield fully amorphous PVA powder and final products with >99 wt.% C12A7. Direct formation to C12A7 is observed starting at 850 °C under flowing dry air and decomposition to C5A3 and C3A is first observed at 1024 °C as is expected due to the instability of the occluded oxygen anion, Figure 23. The kinetic in-situ investigation shows that for these environmental conditions that the instability temperature is lower than that previously reported (1050 °C) [10]. The amount of the decomposition product C3A is low and is

obscured by superposition of the (024) C12A7 peak and is not included in graphical representation of present phases; with an increase in collection range or an increase in resolution (at the expense of longer data collection and time resolution) the C3A phase fraction can be determined. The quantification of lattice parameter shows a larger discrepancy over the data set than in previous data collection, however, the average value of approximately 12.055 Å agrees well with the lattice parameter when Cu incorporation occurred in the amorphous citrate method, Figure 24. The discrepancies come from experimental error and the difficulty in resolving two correlated refinement parameters in a small 2Θ range; a larger data collection range can reduce this discrepancy with a larger characterized d-spacing. The crystallite size increases from ~48 nm to above 150 nm as the temperature is raised, Figure 24.

Sample microstructure characterized with an ex-situ synthesized sample, which did not undergo decomposition, consists of nanosized uniform crystallites (grains), approximately 200 nm, and appears to be homogenous since no bright Cu-containing secondary phases are observed when utilizing the back scattered detector, Figure 25. Less severe cracking was observed, compared to samples synthesized using the amorphous citrate sol-gel technique, and the microstructure shows evidence of sintering in the form of necking and needle growth across microstructural voids.

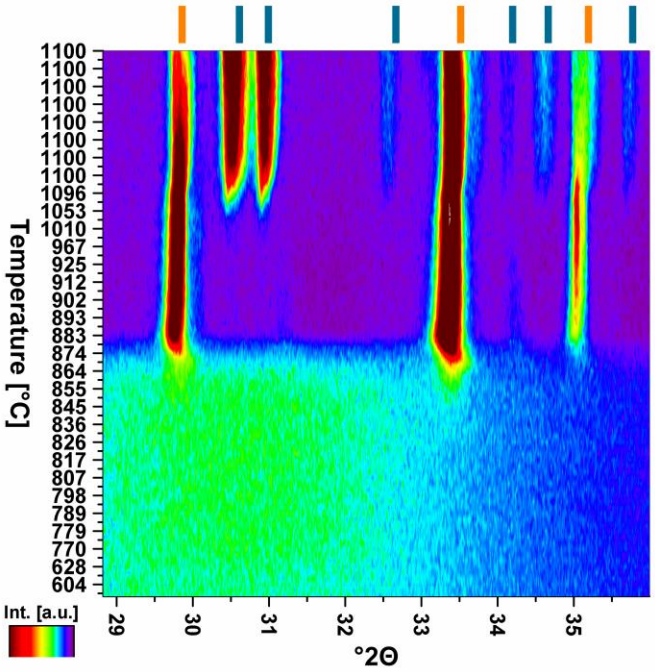

Figure 23 HTXRD data of Cu-doped C12A7 synthesized with a PVA precursor with a 1:4 PVA:cation ratio. The Y axis is represented in temperature and correlates with increasing scan number and the color is indicative of measured intensity. Phase markers identify characteristic C12A7 peaks in orange and C5A3 in blue.

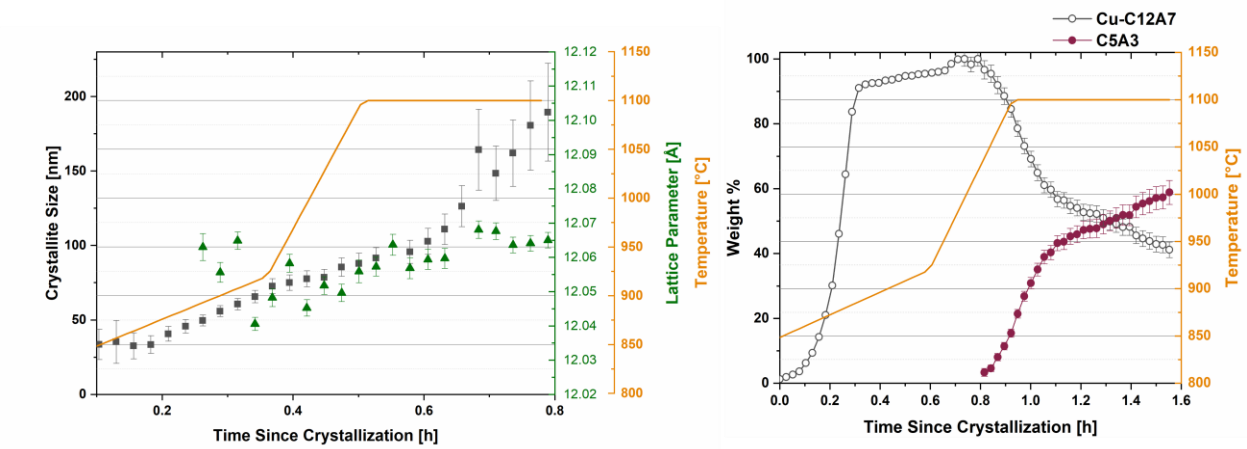

Figure 24 (Right) Quantitative phase amounts as a function of crystallization time. Peak Area, obtained from peak fitting, was used to characterize the formation of C12A7 and decomposition to C5A3 was quantified via Rietveld Refinement. (Left) Characteristic changes in lattice parameter and crystallite size as a function of crystallization time. In both plots sample temperature is plotted as a function of time.

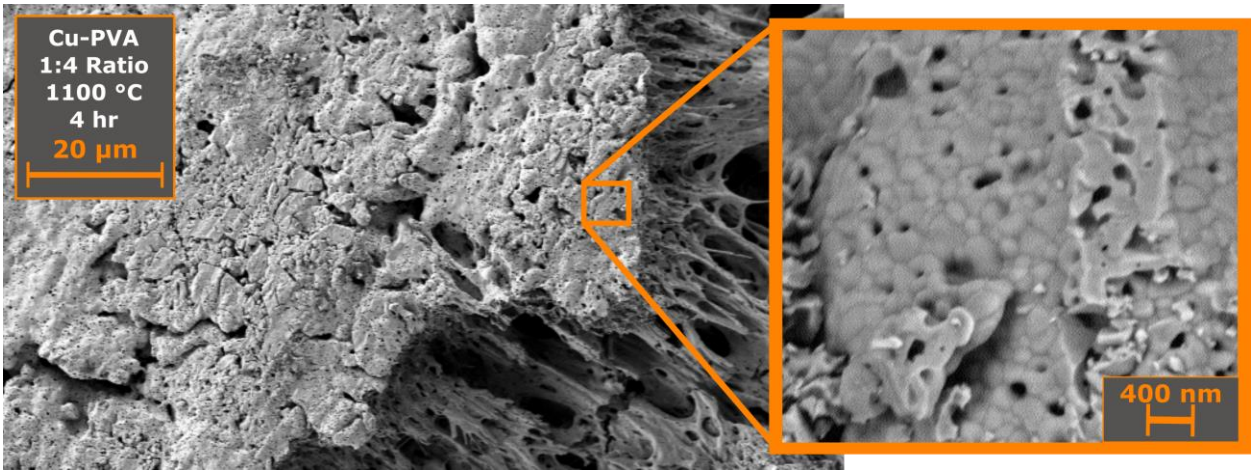

Figure 25 SEM Characterization of the Cu-C12A7 product calcined for 4 h at 900 °C utilizing the a PVA powder precursor with a 1:4 PVA to cation ratio.

2.4.4 Discussion

Kinetic evolution and microstructure closely mirrors that obtained in the amorphous citrate synthesis when the pH is raised to 4 and drip evaporation is performed. Crystallite size characterization identifies a smaller nucleation value, but significant growth is observed suggesting non-homogenous nucleation and the ability for growth. This is to be expected for the polymer assisted method. Localized clusters of cationic species are observed due to the ability for the OH^- functional group to bond to multiple cations. This results in a small nucleated grain, but grain growth will happen non-homogenously allowing for a distribution of crystallite sizes and thermodynamic pressure for grain growth. Modifications to polymer molecular mass to smaller values can result in shorter diffusion pathways between nucleation sites and a higher degree of homogenous nucleation.

No Cu-rich secondary phases are observed and the lattice parameter of ~ 12.055(6) Å, close to that observed in the amorphous citrate method of ~12.050(4) Å suggests Cu incorporation. The slow non-oxidative decomposition of the PVA polymer chain reduces the risk of reduction of the transition metal and the lack of the need to form individual metal ligand complexes eliminates the need for pH adjustment. This may not be the case for all metal species and the addition of ethylene diamine tetra-acetic acid (EDTA) can be added as it will bond to almost all cationic species and has a high affinity for coordination with PVA [145]. TGA of the PVA decomposition exhibits a gradual decomposition compared to the intense decomposition in the amorphous citrate process. A 2x yield in oxide powder is observed decreasing cost of synthesis and the CO_2 emissions reducing the ecological footprint of manufacturing.

Decomposition of the Cu-C12A7 phase is observed at 1024 °C which is 25 °C lower than previously reported. The decomposition has been characterized to be nucleated at the grain boundaries and macroscopic crystalline defects and is correlated to the instability of the occluded oxygen anion [47]. The instability of the anion is also dependent on the surrounding atmosphere and as the atmosphere and macroscopic defect concentration changes the onset temperature and rate of decomposition will likely change [7, 9]. The mobility of the Ca cation has been suggested as the defining factor for the onset temperature of 1050 °C, and the presence of Cu may act as a catalyst whose critical mobility limit should be lower than Ca due to the less refractory behavior of CuO compared to CaO.

The PVA method is an efficient method for obtaining Cu-C12A7 regardless of experimental parameters. The optimum formation occurs with a 1:4 PVA:cation ratio for both pure and Cu-doped C12A7 synthesis and is assumed to be ideal for all low mol% dopant systems allowing for near universal application without process refinement as the cationic system changes. The synthesis yield is increased leading to a reduction in cost and ecological impact. For these reasons the PVA method is chosen for the direct synthesis of C12A7 electrides and should be the preferred sol-gel synthesis method moving forward.

2.4.5 Conclusion

The PVA synthesis method introduces steric entrapment to retain atomic homogeneity and the lack of the necessity to form individual metal ligand complexes results in the formation of Cu-C12A7 at the same temperatures observed in the amorphous citrate process. A nanometer size grain structure is retained after processing for 4 h at 900 °C and the amount of powder yield is double that of the amorphous citrate method resulting in the retention of pellet shape with limited cracking if any at all. The process is robust for the cationic systems tested and the addition of EDTA results in process adaptation to almost all cationic systems with no process refinement such as pH, ratio, or solvent evaporation. For these reasons the PVA synthesis is implemented for direct synthesis of C12A7 electrides and is a novel synthesis for the C12A7 system with numerous advantages over the widely used amorphous citrate method.

CHAPTER 3
Kinetic Studies of C12A7 Formation

3.1 Abstract

Rapid in-situ non-ambient X-ray diffraction represents a powerful tool for characterizing the evolution of crystalline materials in real time. The calcium aluminate system and formation of $Ca_{12}Al_{14}O_{33}$ (C12A7) is particularly sensitive to processing conditions. This report characterizes the kinetic pathways to thermodynamic equilibrium as a function of atmosphere (ambient, dry, and vacuum) and reactant heterogeneity (as-received, milled, and sol-gel reactants). When reactants are heterogenous (as-received and milled) intermediary phases of $Ca_3Al_2O_6$ (C3A) and $CaAl_2O_4$ (CA) are observed as the route to C12A7 formation and $Ca_5Al_6O_{14}$ (C5A3) is only observed as a decomposition product of C12A7. When reactants are heterogenous C12A7 is only thermodynamically favorable under ambient conditions due to the stability provide by hydration. When reactants are homogenous (sol-gel) direct crystallization of C12A7 from an amorphous precursor is observed at low temperature regardless of atmosphere defining C12A7 as the kinetic equilibrium. These findings accurately define the previously misclassified heterogenous formation pathways and report for the first time the formation of C12A7 under a carbon free vacuum environment.

3.2 Introduction

3.2.1 C12A7 Background

$Ca_{12}Al_{14}O_{33}$, the mineral mayenite or C12A7, crystallizes in a clathrate structure where a positively charged framework is balanced by occluded anionic species. The high interconnectivity of the cages in the clathrate structure leads to high occluded anion mobility. The functionality of the structure is derived from the mobility and diversity of occluded chemical species leading to a wide range of applications [42,45]. The C12A7 structure, occluded anion speciation, lattice parameter, and kinetic formation are all heavily correlated to processing conditions. Current thermodynamic studies of C12A7 present a thermodynamic equilibrium derived inference on the kinetics of phase formation. With the thermodynamic phase equilibria defined, an in-situ kinetic structural investigation of C12A7 is warranted to better understand the proposed kinetic pathways to thermodynamic equilibrium. With this knowledge careful control of synthesis can lead to optimization of material properties for a wide variety of applications.

C12A7 thermodynamic phase equilibria is well characterized, and through characterization of these end points inferences of the kinetic pathways were made [65,66]. Thermodynamic equilibria of calcium aluminate formation via solid state synthesis reactants $CaCO_3$ and Al_2O_3 identify C5A3 and C3A as the first phases to form followed by aluminum rich phases, for example CA, regardless of starting reactant stoichiometry; this leads to the suggestion that the diffusion of Ca is the kinetic pathway to the equilibrium [65]. Tian et al. characterized an onion like microstructure structure where Al_2O_3 particles are at the core and layers of progressively higher Ca containing calcium aluminate phases consecutively surround the core through to the surface [65]. More specifically for C12A7 stoichiometry the synthesis pathway is dependent on the

heterogeneity of starting reactants and two formation pathways (1) C5A3 + C3A and (2) C3A + CA are observed in high homogeneity and low homogeneity cases, respectively [66]. The C5A3 and C3A pathway is predicted to be the low temperature pathway for C12A7 formation as reactant homogeneity increases via wet chemistry/sol-gel techniques. C12A7 thermodynamic phase equilibria also changes with process environment. C12A7 is precluded from the thermodynamic $CaO\text{-}Al_2O_3$ binary phase diagram under dry atmospheres and only appears when moisture is present indicating metastability under elevated temperature conditions in inert, dry oxidative, or reducing atmospheres [42]. Thermodynamic studies have thoroughly characterized the phase equilibria, but a kinetic characterization and confirmation of the proposed kinetic pathway to equilibrium is missing.

The historical characterization of phase equilibria has adopted a thermodynamic approach. The technique dubbed ‘cook and look’ involves heating at a temperature for an extended period of time, quenching to retain the phase assemblage, and then structurally characterizing the results. This characterizes the thermodynamic equilibria well but information on the kinetic pathway is lost. The kinetic transformation can be captured by quenching the sample at various process durations and temperatures to ‘freeze in the evolving phases’, however, this requires Edisonian experimental procedures, and only provides a single snapshot of the behavior. If the sampling rate is not high enough full kinetic pathways could be missed. While quenching works to freeze diffusive transformations, non-diffusive phase transformations behavior may be lost during the quench due to the fast transformation rates.

With the advances in computational modeling and instrumentation software and hardware, the precise and high resolution structural determination of kinetic pathways is now possible in a laboratory setting. In-situ non-ambient high-temperature X-ray diffraction (HTXRD) provides a characterization method that can probe the kinetics of phase transformations in real time by rapidly collecting diffraction patterns during heating. This allows for identification metastable and non-equilibrium phases and formation pathways. Until recently this type of characterization required travel to a synchrotron X-ray or time-of-flight neutron source to collect diffraction data at the intervals needed to capture fast kinetic transitions. Lab XRD has evolved to where an area detector can continuously monitor a large enough region of °2Θ, where several key phase diffraction maxima are located, dynamically replacing point detectors and leading to large increases in measurement of diffracted intensity as a function of °2Θ.

The Malvern PANalytical Empyrean diffractometer equipped with an Anton Paar HTK1200N high temperature furnace and PIXcel^{3d} area detector provides stable controllable sample environmental modification and rapid data collection. Rapid data collection on heating captures dynamic and static phase transformations. A combination of isothermal and non-isothermal data collection, normally acquired through thermal analysis characterization, can be used to derive information about the activation energy, type of kinetic process, limitations in kinetic transformations, and modes of structural transformation.

3.2.2 Kinetic Theory

Specifics of the kinetic transformation can be determined by analyzing the integrated peak area, or phase fraction determined through Rietveld refinement if multiple phases coexist, to track the evolution of crystallization as a function of time or temperature. This parameter, frequently denoted $\alpha = \frac{A_{observed}}{A_{max}} = \frac{Wt\%_{observed}}{Wt\%_{max}}$, is analyzed as a function of time at a constant temperature in isothermal characterization or time and temperature in a non-isothermal characterization. To properly identify the limiting kinetics of the phase transformations the development of a master plot allows for direct comparison of the rate of reaction to various kinetic models [149].

A master plot is a diagram which graphically represents an analytical expression for the rate of transformation vs transformed fraction for diffusion, phase boundary, and random nucleation and growth kinetic models [149]. When experimental data is superimposed on the diagram the type of kinetic transformation can be elucidated based on the correlation of experimental data to the analytical expression of the theoretical models. Gotor et al. redefined a method for creating master plots which can be applied universally to the analysis of solid state kinetic transformations regardless of the temperature dependence of the characterization [149]. The original application was for thermal analysis, but with the advent of kinetic HTXRD analysis the methods can be reinterpreted for X-ray characterization. For isothermal characterization only a single isothermal α vs time curve is needed to identify the kinetic model which best characterizes the kinetic transformation. For a linear non-isothermal temperature vs time dependence (isochronal), an α vs temperature curve and the activation energy of the transition is needed to utilize the master plot. Activation energy can be derived from thermal analysis characterization or through multiple isothermal characterization and implementation of methods such as the Kissinger method [150]. For a non-linear non-isothermal temperature vs. time dependence the relationship between temperature and time, α as a function of temperature, and activation energy must be known [149].

Derivation of the formation of an isothermal master plot is presented here, but any further understanding or application of the generalized time master plot to non-isothermal data will require referencing the original publication [149]. The rate of kinetic transformation is described by an Arrhenius form multiplied by a function which describes the kinetic reaction, Equation 3.

$$\textbf{Equation 3 } \frac{d\alpha}{dt} = A \exp\left[\frac{-E}{RT}\right] f(\alpha)$$

Where A is the Arrhenius factor, T is the absolute temperature, E is the activation energy, and $f(\alpha)$ is the function which characterizes the kinetic transition. For easy comparison between models and experimental data normalization to the rate of kinetic transformation at $\alpha = 0.5$ is performed Equation 4.

Equation 4 $$\left.\frac{\frac{d\alpha}{dt}}{\left(\frac{d\alpha}{dt}\right)_{\alpha=0.5}}\right. = \frac{f(\alpha)}{f(0.5)}$$

Normalizing the data to $\alpha = 0.5$ demonstrates that the experimental reaction rate is equivalent to the theoretically calculated value of $\frac{f(\alpha)}{f(0.5)}$ only when the correct model is used to describe the rate of kinetic transformation. This simplification occurs due to the equivalence of the exponential term with constant temperature; in the case of non-isothermal heating the exponential terms are not equivalent and further information is required. The comparison of the experimental data against the theoretical expression allows for the identification of the model which accurate describes the kinetic transformation.

The function $f(\alpha)$ for diffusion, grain boundary, and homogenous nucleation and growth kinetic transformations are represented in Table 9. The master plot is created by plotting $\frac{f(\alpha)}{f(0.5)}$ and the experimental data $(d\alpha/dt) \,/\, (d\alpha/dt)_{\alpha=0.5}$. The master plot of $\frac{f(\alpha)}{f(0.5)}$ vs α is shown in Figure 26.

The homogenous nucleation and growth kinetic model is known as the Johnson-Mehl-Avrami-Kolmogorov (JMAK) model. The kinetics of this transformation have three distinct processes; the first is homogenous random nucleation, followed by nuclei growth, and nuclei impingement. The model analytically describes isothermal kinetic transformation and has been expanded by Kissinger and Ozawa to non-isothermal kinetic transformations [151]. The model in the general form represents the change in α as an exponential factor, Equation 5, where I(T,t) is the nucleation rate of the nuclei and V is the volume of a particle formed at t_0; these two factors correspond to the first two processes nucleation and nuclei growth, respectively, and the third stage of impingement is assumed to be due to hard impingement of randomly nucleated nuclei which leads to the $1 - \exp(-X)$ dependence.

Equation 5 $$\alpha[T,t] = 1 - \exp\left(-\int_o^t I[T,t] * V[T,t,t_0]\, dt\right)$$

The most widely used form of the model is a special JMAK case which assumes that nucleation occurs randomly and homogeneously and the growth rate is constant with respect to time and transformed fraction, Equation 6 [152]. k, described in Equation 7, represents a temperature dependent rate constant dependent on the growth mode factor m, dimensionality d, dimensionality of growth f_d, ΔS system entropy, ν effective attempt frequency, Boltzmann constant, and U particle growth rate. n, described in Equation 8, represents the JMAK exponent which is dependent on the dimensionality and the growth mode [153].

Table 9 $f(\alpha)$ representing the main models for solid-state kinetic transformations

Kinetic Mechanism	Symbol	$f(\alpha)$
Phase Boundary Controlled (2D)	R2	$(1-\alpha)^{\frac{1}{2}}$
Phase Boundary Controlled Reaction (3D)	R3	$(1-\alpha)^{\frac{1}{3}}$
Unimolecular decay law (instantaneous nucleation and 1D growth)	F1	$(1-\alpha)$
Random nucleation and growth (JHAM model)	Am	$n*(1-\alpha)*[-\ln(1-\alpha)]^{1-\frac{1}{n}}$
2D diffusion	D2	$\frac{1}{-\ln(1-\alpha)}$
3D diffusion (Jander equation)	D3	$\frac{3(1-\alpha)^{\frac{2}{3}}}{2(1-\alpha)^{\frac{1}{3}}}$
3D diffusion (Ginstein-Brounshtein equation)	D4	$\frac{3}{2[(1-\alpha)^{-\frac{1}{3}}-1]}$

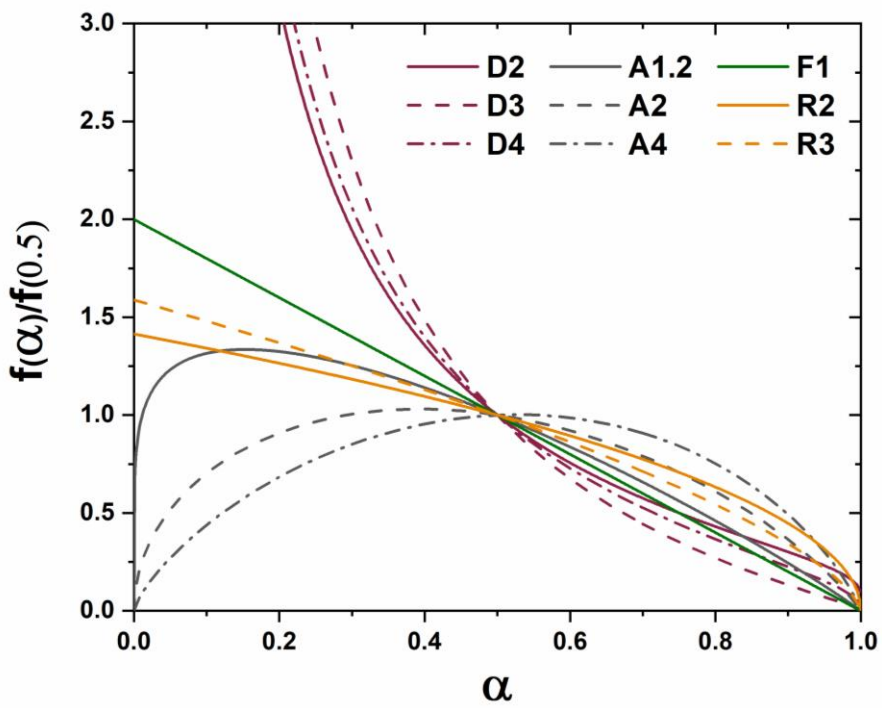

Figure 26 $f(\alpha)/f(0.5)$ master plot. Recreated from [149]

$$\textbf{Equation 6 } \alpha = 1 - e^{(-k*(t-t_0)^n)}$$

$$\textbf{Equation 7 } k = \sqrt[n]{\frac{f_d \nu e^{\frac{\Delta S}{k_b}} U^{\frac{d}{m}}}{\frac{d}{m}+1}}$$

$$\textbf{Equation 8 } n = \frac{d}{m} + 1$$

Conventional analysis involves determining these two values (k and n) through data fitting and deriving information about the kinetic transformation dimensionality, growth mode, and activation energy. Table 10 demonstrates the analysis of JMAK exponent for different kinetic models.

In the case of heterogeneous kinetic transformations, commonly referred to as diffusion-controlled transformations, the mobility of constituents in the system controls the transformation rate. In homogeneous reactions the growth of the new phase is expected to occur non-preferentially where as in heterogenous reactions the nucleation and growth occurs at preferred non-homogenous interfaces. In heterogeneous systems the constituents are separated into their own particles, normally individual oxides in solid state synthesis reactions, and long diffusion pathways are required to reach and grow the nucleating phase. The kinetics of these reactions are dependent on constituent mobility, for oxides this include anion and cation mobility, and mobility can be limited by

Table 10 Analysis of JMAK exponent for all possible growth scenarios. Reproduced and updated from Fotsing [153].

Dimensionality	Nucleation Model	Interface controlled transformation (m=1)	Diffusion controlled transformation (m=2)
3-D (d=3)	Site Saturation	3	1.5
	Continuous Nucleation	4	2.5
	Decreasing Nucleation	3-4	1.5-2.5
2-D (d=2)	Site Saturation	2	1
	Continuous Nucleation	3	2
	Decreasing Nucleation	2-3	1-2
1-D (d=1)	Site Saturation	1	0.5
	Continuous Nucleation	2	1.5
	Decreasing Nucleation	1-2	0.5-1.5

lattice defects and microstructural voids [154]. As the diffusion based kinetic reactions continue the growing phase will further separate the two reactant phases leading to a decay of the reaction rate. When the reactant particles are spherical, three-dimensional diffusion will occur; α, given by Equation 9, is analytically derived from the radius of the reactant particle, R, and the thickness of the product layer, x [154].

$$\textbf{Equation 9 } \alpha = 1 - \left(\frac{R-x}{R}\right)^3$$

Geometric contraction models assume that nucleation of the transformed phase occurs on the surface of the reactant phase and growth is controlled by the consumption of the bulk phase. In general, the reaction rate is governed by Equation 10 where r is radius at time t, r_0 is the untransformed particle radius, and ν is the reaction rate constant. The reaction rate can be expressed for special cases such as 2D cylinder (contracting area) or 3D spherical (contracting volume) growth [154]. For the spherical case α is given by Equation 11. The particle size is incorporated in the rate constant in both the contracting volume and geometric models (diffusion models) indicating a change in the reactant particle sizes will alter the transformation reaction rate [154].

$$\textbf{Equation 10 } r = r_0 - \nu t$$

$$\textbf{Equation 11 } \alpha = 1 - \left(\frac{r_0 - kt}{r_0}\right)^3$$

A physical representation of the three kinetic models is shown in Figure 27. With the tool of in-situ XRD this study characterizes the kinetic pathways of a C12A7 stochiometric reactant mixtures as a function of reactant homogeneity, atmosphere humidity, and oxidizing/reducing conditions. The kinetic transformations observed with HTXRD are analyzed applying the master plot method.

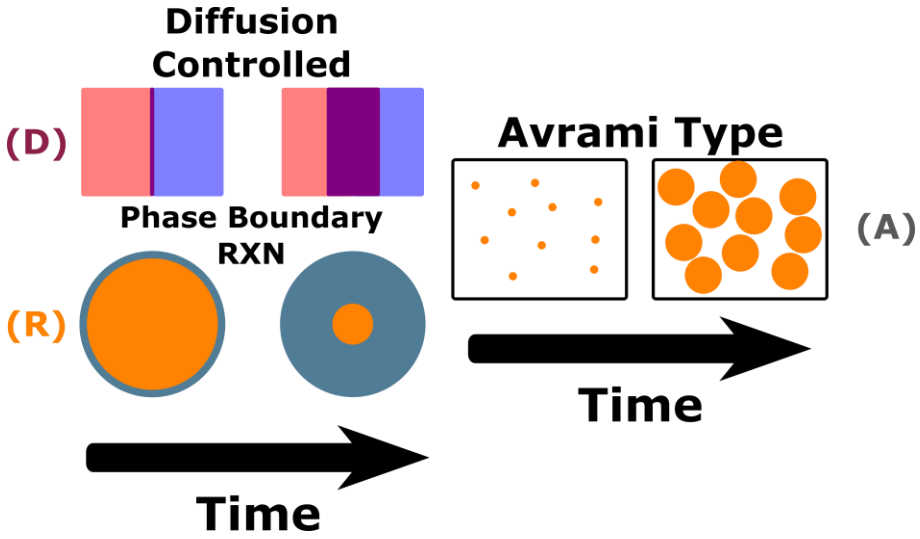

Figure 27 Physical representation of JMAK, heterogenous diffusion, and geometric contraction kinetic transformations.

3.3 Experimental

Three different reactant mixtures where characterized to identify changes in kinetic formation as a function of reactant homogeneity. Solid state synthesis reactants where analyzed both with the reactant materials in the as-received state resulting in a high heterogeneity mixture and with the as-received reactant subject to ball milling to reduce the particle size resulting in a lower heterogeneity mixture. A polymer assisted sol-gel reactant mixture was used to characterize the case of atomic level homogeneity.

A high heterogeneity reactant mixture was derived from the standard solid-state synthesis precursors of $CaCO_3$ and Al_2O_3 powders. The powders were dried in a vacuum drying oven at 37 torr and 200 °C for 24 h before being measured into stoichiometric amounts and thoroughly mixed in a vibratory mill. The starting particle size of as-received reactants is on the order of 10's □m for $CaCO_3$ and ≤ 100 nm for Al_2O_3.

A lower heterogeneity reactant mixture was prepared by ball milling the as received $CaCO_3$ to decrease the particle size to ≤ 200 nm. The reactant powder mix was milled in a Pulversette 7 premium high energy planetary ball mill in a yttria

stabilized zirconia (YSZ) bowl with 1 mm YSZ milling media and isopropanol alcohol. Process parameters consisted of a 0.5 h milling step at 900 rpm followed by a 0.5 h hold and repeated six times.

An atomically homogenous reactant mixture was prepared through the polymer assisted synthesis route utilizing polyvinyl alcohol (PVA) [117]. A 4:1 cation to PVA ratio was chosen and the appropriate mass of PVA (molecular mass of 20,000-30,000) was dissolved in DI water and allowed to age for 24 h. $Ca(NO_3)_2 \cdot 4H_2O$ and $Al(NO_3)_3 \cdot 9H_2O$ were used as cation sources and were measured from 1 molar stock solutions whose molarities were determined through inductively couple plasma spectroscopy (ICP). Stoichiometric amounts of nitrate solutions were extracted and combined with the PVA solution under vigorous stirring. The solution was aged for 1 h before solvent evaporation was performed at a solution temperature of 90 °C. When approximately 15% of the solvent volume remained, the solution exhibited bubbling before returning to a steady state. Powder was continually scrapped off the bottom and sides of the beaker after this step until the solution was completely converted to a yellow powder. This powder was then ground in a YSZ mortar and pestle and calcined to 600 °C. The obtained white powder is the homogenous non-carbonaceous reactant for the kinetic investigations.

In-situ non-ambient high-temperature X-ray diffraction (HTXRD) experiments were performed on a Malvern PANalytical Empyrean diffractometer utilizing an Anton Paar HTK 1200N high temperature furnace sample stage and a PIXcel^{3D} area detector with 255 active channels and ~ 3° 2θ of coverage. Samples were heated to either 1100 or 1200 °C with a ramp rate of 300 °C/h under flowing compressed air (~120 ppm H_2O), static ambient atmosphere, or high vacuum (8E-5 torr); in the case of PA sol-gel reactants the ramp rate was decreased to ~150 °C/h to yield more transformation resolution due to the rapid kinetics of formation. Data were collected both rapidly (< 2 min per pattern) and continuously during the furnace ramp. A small 2θ range of 27.5 - 37° 2θ was utilized as it captures the amorphous hump of the sol-gel reactant mixture, high-intensity peaks for all phases $Ca_5Al_6O_{14}$ (C5A3), $C_3Al_2O_6$ (C3A), $CaAl_2O_4$ (CA), $CaCO_3$, Al_2O_3, and CaO, and five characteristic peaks of C12A7. Reported temperature is the sample temperature, not the set temperature, and was measured by a thermocouple directly below the sample. Instrumental setup and collection specifics are summarized in Table 11 and incident and diffracted beam optics were optimized for intensity over resolution. For data collection all reactant mixtures were pressed into 13 mm pellets with a thickness of 2 mm and placed in the sample holder.

Phase matching was performed utilizing the International Centre for Diffraction Data (ICDD) PDF-4+ 2018 database. Rietveld refinement was performed using the Malvern PANalytical HighScore Plus software package [155]. Lattice parameters, background, scale factors, surface sample displacement, phase fractions, and profile parameters relevant to crystallite size determination were refined. During the formation of the C12A7 phase from an amorphous reactant mixture pseudo-Voight peak fitting was used to determine the change in peak area relating to an increase in the wt.% of

Table 11 HTXRD instrumental and data collection parameters.

Instrument Parameters			
Instrument	PANalytical Empyrean		
Source	Cu $K\alpha_1/K\alpha_2$		
Stage	Anton Parr HTK 1200N		
Detector	PIXcel3D-Medipix3 1x1 detector		
Mode	Scanning Line Detector		
Active channels	255 (3.3482 °2θ)		
Collimation			
Incident			
Divergence Slit [°]		1/4	
Soller slit [rad]		0.04	
Anti-scatter slit [°]		1/2	
Mask [mm]		10	
Diffracted			
Anti-scatter slit [mm]		5	
Soller Slit [rad]		0.04	
Scan Parameters			
Step Size [°2θ]	0.0131		
Step Time [s]	13.7		
Scan Time [s]	90/150*		
Scan Range [°2θ]	27.5 - 37		
Temperatures	Dynamically (RT to 1100/1200 °C)*		

* PVA/SSS respectively

C12A7 relative to the amorphous content. Crystallite size was determined through pseudo-Voigt profile fitting and is documented in the HighScore Plus software package as being calculated using Equation 12 and Equation 13, which describe crystallite size and size variance, respectively [155]. W_i and W_{std} are coefficients used to describe peak width for a given reflection i and the standard respectively and $\sigma^2(W_x)$ refers to the variance of those values. Instrumental broadening was characterized with NIST standard SRM 640e (Si), and the refined values were used during the HTXRD Rietveld refinements.

$$\textbf{Equation 12} \quad D_i = \left(\frac{180}{\pi}\right)\frac{\lambda}{(W_i - W_{std})^{0.5}}$$

$$\textbf{Equation 13} \quad \sigma^2(D_i) = \frac{\left(\frac{180}{\pi}\right)*\lambda}{(W_i - W_{std})^{0.5}}\left[\sigma^2(W_i) + \sigma^2(W_{std})\right]$$

3.4 Results

The comprehensive characterization of reactant homogeneity and synthesis atmosphere through HTXRD leads to a 3 x 3 matrix of characterization. For simplicity the results will be subdivided by atmosphere with analysis of reactant homogeneity

contained in that subsection; The subsection organization follows the order SSS as-received, SSS milled, PVA isochronal, and PVA isothermal. Kinetic analysis is only performed in situations where isothermal phase evolution is observed.

3.4.1 Ambient Processing Atmosphere

In the case of high heterogeneity, SSS as-received, the path way towards the phase equilibria assemblage progresses through four distinct regions; these regions are $CaCO_3$ decomposition to CaO, CaO and Al_2O_3 phase equilibria, C3A and CA phase formation, and finally C12A7 formation, Figure 28.The decomposition transformation of $CaCO_3$ to CaO initializes at 680 °C and completes by 880 °C. Equilibrium of the CaO and Al_2O_3 phase remains until 980 °C when the formation of CA followed by C3A at 1025 °C is observed. The transformation continues as time and temperature are increased. C12A7 formation is observed at 1180 °C, before the complete conversion of CaO and Al_2O_3 to C3A and CA, and the formation continues at a processing dwell temperature of 1200 °C. C3A wt % reaches a maximum amount correlated with the presence of rapid C12A7 formation while CA formation continues. The isothermal master plot of C12A7 formation for SSS as-received reactants shows a clear multi-type transformation behavior, Figure 29. During the initial stages of the transformation the rate of C12A7 formation displays an JMAK type behavior with an initial acceleration of the reaction rate. As the process continues a diffusion-based transformation mode is observed with an exponential decay of the reaction rate. The high heterogeneous reactant phase equilibria agrees with previously characterized thermodynamic equilibrium and the type of kinetic transformation changes as the availability of reactants decreases; no C5A3 formation was observed at any point during the HTXRD experiment [65,66].

In the case of low heterogeneity, a change in the energy needed for phase formation and the rate of formation are altered, but the same phase evolution pathway is observed, Figure 28. $CaCO_3$ to CaO decomposition initializes at 750 °C and completes by 800 °C with an increased reaction rate than that observed before a reduction in $CaCO_3$ particle size. C3A phase formation is observed concurrent with $CaCO_3$ decomposition at 785 °C followed by CA phase formation at 915 °C. C3A and CA phase formation continues at the expense of all remaining Al_2O_3 and CaO. C12A7 phase formation is not observed until 1000 °C after Al_2O_3 and CaO reactants are consumed and formation occurs at the expense of C3A and CA. The formation of C12A7 is rapid with formation completed by 1125 °C within 0.5 h of the start of the transformation. Single phase C12A7 is not observed and an equilibrium between C3A, CA, and C12A7 is observed with no change with extended process time of up to 12 h; albeit the concentration of C12A7 is increased to approximately 90 wt.%. No kinetic analysis can be performed as C12A7 formation occurs completely during the isochronal heating, but the lack of complete C12A7 formation suggesting a diffusion limited process. The synthesis utilizing milled starting reactants follows the expected thermodynamic equilibrium and a clear benefit to the reduction of particles size in the

kinetic transformation rate to this equilibrium is observed; No C5A3 is observed at any point during the HTXRD experiment. In agreement to the SSS as-received a decrease in the transformation temperature and an increase in the rate of formation is observed with milling of the reactant mixture. The milling decreases the particle size of the $CaCO_3$ and subsequently decreases the reactant heterogeneity.

The polymer assisted sol-gel reactant removes heterogeneity by providing homogeneity at the atomic level. During isochronal characterization of powder previously calcined to 600 °C an amorphous background is observed up to 850 °C after which direct and rapid formation of the C12A7 phase is observed completing by 950 °C after a transformation time of 0.3 h, Figure 28. During the formation of C12A7 the characteristic peaks of C5A3 are qualitatively observed until approximately 1050 °C. The net height of the C5A3 peaks above the background is less than three times the standard deviation of the background noise indicating that the peaks are not statistically significant; C5A3 is observed momentarily and is below the resolution of phase quantification. During isothermal characterization the process temperature is held at 850 °C, Figure 28. As in the isochronal case C12A7 formation occurs instantaneously and full phase formation is observed after a processing time of approximately 2 h. During the formation of C12A7, C5A3 characteristic peaks are barely discernable with net intensity even less than in the isochronal case. A comparison of the rate of reaction for the isothermal investigation, Figure 29, clearly demonstrates an JMAK type transformation. Fitting the Avrami equation, Equation 6**,** a n value of 1.81(5) and a rate constant, k, of $3.6(2)x10^{-7}$ s^{-1} was determined Figure 30. Determination of crystallite size elucidates a slow growth rate as a function of process time with an increase of approximately 7 nm, from 35 to 42 nm, was observed after 2 h leading to a growth rate of $5.0(5)x10^{-13}$ m/s. Larger errors in crystallite size are observed initially due to the errors in fitting the peak shape that emerged on top of the amorphous background. As the reactant mixture moves to atomic homogeneity deviation from thermodynamic studies is observed with direct statistically phase pure C12A7 formation accompanied by a decrease in formation temperature from 1000 and 1180 °C observed when utilizing milled and as-received solid-state reactants, respectively, to 850 °C for the homogenous PA sol-gel reactant mixture.

3.4.2 Dry-Air

With high heterogenous reactants C12A7 formation deviates from the behavior observed during ambient conditions; while all four phases are still observed the presence of an additional phase C5A3 and the ultimate thermodynamic phase equilibria is altered, Figure 31. The $CaCO_3$ decomposition is observed starting at 580 °C and completes by 760 °C. CaO and Al_2O_3 are observed until 1025 °C where formation of C3A and CA are observed with equivalent rates at the expense of CaO and Al_2O_3. Once process temperature reaches 1200 °C C5A3 and C12A7 formation are observed with the rate of C5A3 formation occurring more rapidly than C12A7; C3A and CA phase concentration continue to increase during this regime and only CaO and Al_2O_3 exhibit a

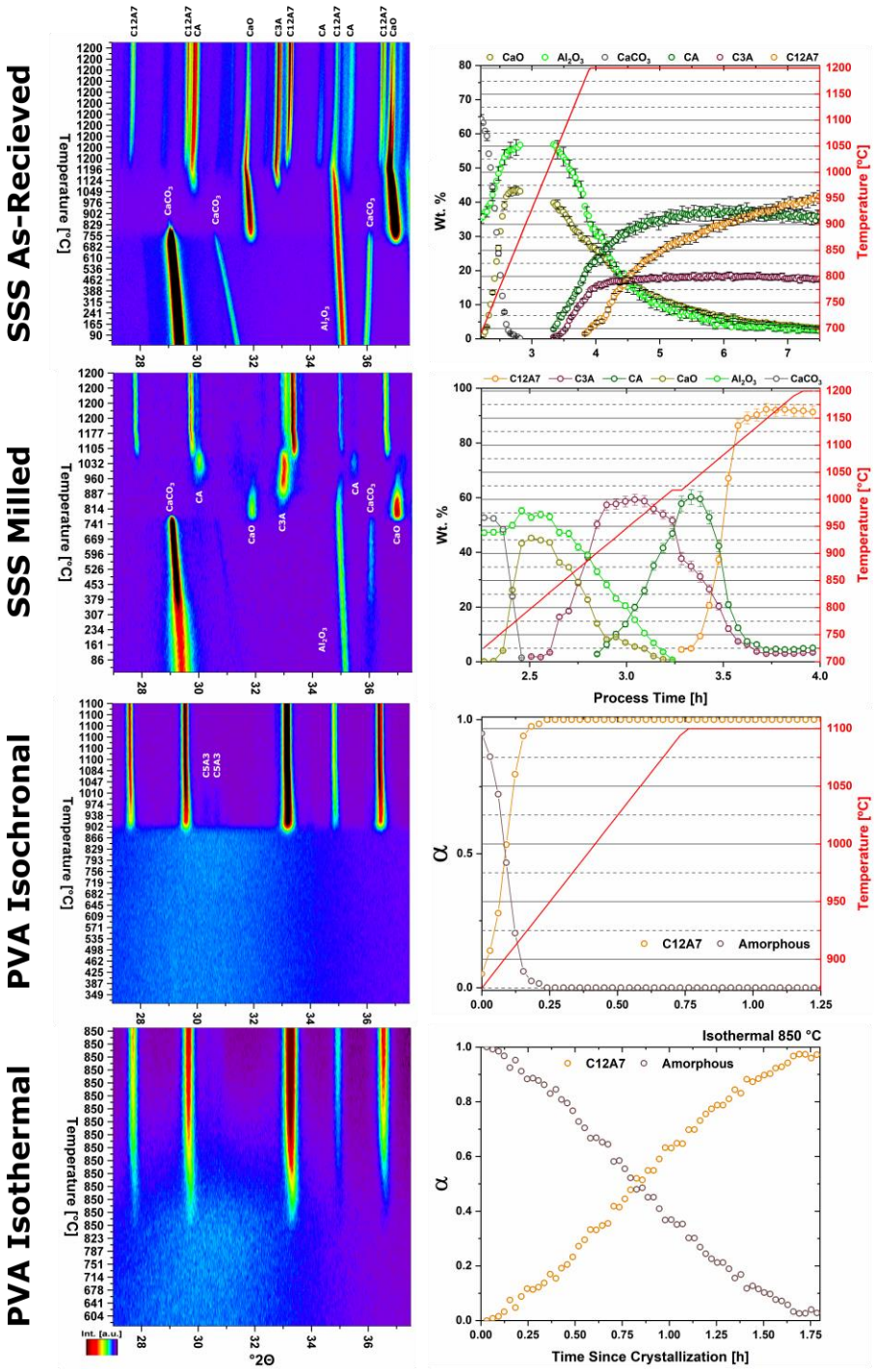

Figure 28 HTXRD data showing peak evolution (left) and quantitative phase determination (right) of high heterogeneous as-synthesized SSS, low heterogenous milled SSS, and homogenous PVA (isochronal and isothermal) reactants under ambient conditions.

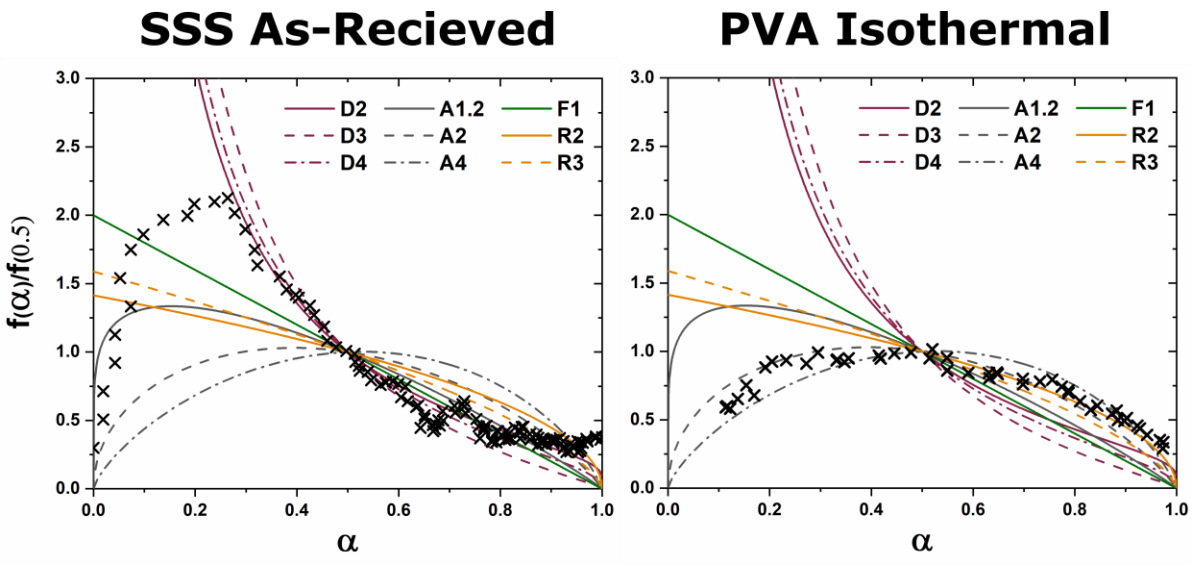

Figure 29 Isothermal master plot of C12A7 formation from as-received solid-state reactants (left) and PVA reactants (right).

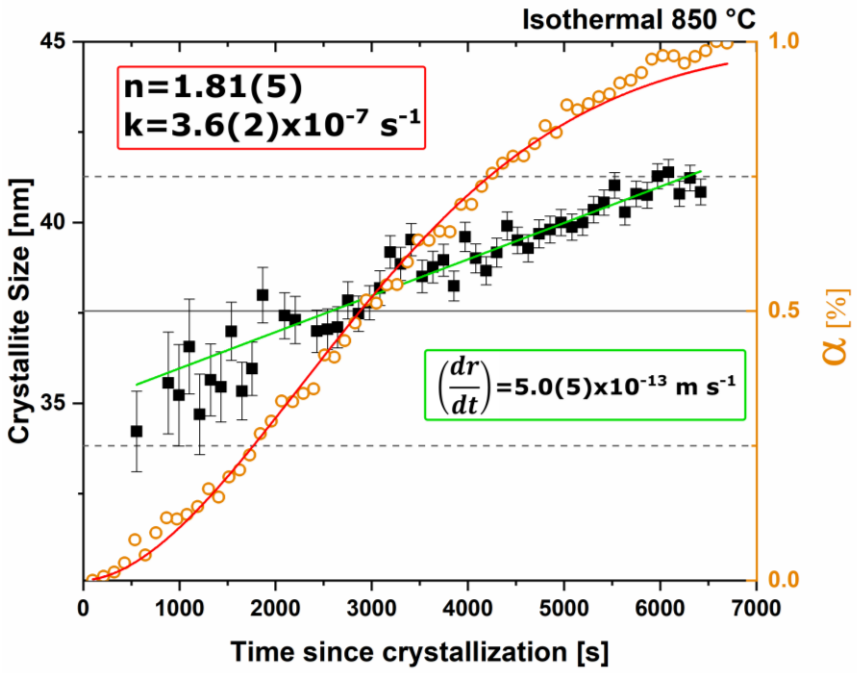

Figure 30 For the isothermal PVA investigation under ambient conditions the fit of the Avrami model to α (orange markers) is observed in red with a n value of 1.81(5) and rate constant of 3.6(2)x10^{-7} s^{-1} and the change of microstructural crystallite size (black markers) shows a linear relationship, green trend line, yielding a radial growth rate of 5.0(5)x10^{-13} m/s.

decrease wt.%. Isothermal master plots characterizing the rate of the formation transformation of both C12A7 and C5A3 from as-received solid-state reactants demonstrate a linear decreases in rate correlated with a phase boundary-controlled process and not a diffusion or JMAK type transformation Figure 32. The transformation appears to reach an equilibrium value after 4 h with the complete reaction of CaO and Al_2O_3; C3A and CA phase evolution is stagnant and C5A3 and C12A7 formation exhibits a decreasing rate. The presence of C5A3 is observed under dry conditions, however, formation does not occur until 1200 °C concurrent with the formation of C12A7. This represents a change in thermodynamic equilibrium to C5A3 under dry conditions as compared to humid conditions.

With low reactant heterogeneity phase formation pathways are the same, however, the temperatures of formation and the rate of formation increase just as observed in an ambient atmosphere, Figure 31. $CaCO_3$ decomposition is observed starting at 600 °C and completes by 700 °C. In a dry atmosphere C3A phase formation does not occur concurrently and a CaO and Al_2O_3 phase assemblage is observed. C3A phase formation is observed starting at 925 °C concurrent with CA formation and continues rapidly at the expense of CaO and Al_2O_3 with the rate of CA formation higher than C3A formation; maximum CA content is observed at 1050 °C while C3A maximum concentration does not occur until 1125 °C. The C12A7 (024) characteristic peak is initially obscured by the C3A peak, however, C12A7 and C5A3 phase formation are observed by 1100 °C at the expense of C3A and CA. The rate and concentration of C12A7 phase formation is initially greater than that of C5A3, however, once at 1200 °C the C5A3 phase formation continues increasing while the C12A7 weight fraction plateaus. As the process continues for 4 h C5A3 wt.% continues increasing at the expense of C12A7.

Isothermal master plots indicate the rate of formation of the C12A7 and C5A3 phases have an increasing then decreasing sigmoidal character consistent with JMAK type transformations, Figure 32A. After this initial formation, ~50 wt.% C5A3 and ~30 wt.% C12A7, the decomposition of C12A7 and further formation of C5A3 have a different rate dependence with a linear decreasing reaction rate as would be characteristic with phase boundary-controlled transformation, Figure 32B. The phase boundary-controlled transformation is similar to the formation rate dependency observed with as-received solid-state reactants under a dry atmosphere. The decrease in reactant heterogeneity displays an increase in the rate of kinetic transformation to the thermodynamic equilibria which at 1200 °C under dry atmospheric conditions is dominated by C5A3.

When the starting reactant has atomic homogeneity the formation of C12A7 occurs directly from the amorphous background at 900 °C, Figure 31. Under isochronal characterization the formation of C12A7 is rapid just as in the ambient atmosphere, however, an increase in the onset temperature by 50 °C is observed. C5A3 phase formation is higher under dry conditions isochronally and statistically quantifiable, however, the formation only occurs during the initial stage of phase formation directly

from the amorphous reactant and no formation kinetics are observed during an isothermal dwell at 1100 °C for 1.5 h. Under isothermal conditions, C12A7 is the predominant phase to form with full formation observed after only 1 h. This is approximately half the time observed under ambient conditions, Figure 31. Under isothermal conditions at 900 °C C5A3 phase formation is negligible and statistically insignificant for quantification. An isothermal master plot characterizing the rate of formation for C12A7 synthesized using the PVA sol-gel method in dry conditions demonstrates a clear JMAK behavior and fitting to the Avrami equation determines an n value of 1.54(3) and a rate constant, k, of 1.3(3)x10^{-5} s^{-1}, Figure 32 and Figure 33. This constitutes a decrease in the n parameter by ~30% and an increase of two orders of magnitude in the rate of reaction. Microstructural evolution demonstrates a clear two stage transformation not observed under ambient conditions, compare Figure 33 to Figure 30. Initially, for low levels of formation, rapid isothermal coarsening of crystallite size from 32 to 38 nm is observed at a rate of $(dr/dt)_1 = 5.0(4)\text{x}10^{-12}$ m/s followed by a slow increase from 38 to 42 nm over a 2 h isothermal dwell with a rate of $(dr/dt)_2 = 7.2(3)\text{x}10^{-13}$ m/s. The latter rate is equivalent to the rate observed under ambient conditions. With atomic homogeneity statistically phase pure C12A7 formation is observed when isothermally characterized at 900 °C and when isochronally characterized C12A7 and C5A3 formation occurs, however, an equilibrium is reached with no further increase in C5A3 during a dwell at 1100 °C.

3.4.3 Vacuum

With high heterogeneous reactants, as received SSS, the same phase evolution as in wet and dry atmospheres is observed initially, however, in the fourth and fifth stages the presence of C12A7 formation and C5A3 formation, respectively, do not occur **Figure** 34. $CaCO_3$ decomposition is observed starting at 500 °C. The exact end temperature is unknown as the furnace was isothermally held at 600 °C to protect vacuum stability during the decomposition and evolution of CO_2 gas. The CaO and Al_2O_3 phase equilibrium is maintained until 990 °C where C3A and CA phase formation is observed. C3A demonstrates a quicker initial formation, however, the rate of CA formation increases and after 2 h of processing at the maximum temperature the CA wt. % is 70% of the theoretical maximum CA concentration and C3A is only 30 % theoretical maximum C3A if all CaO and Al_2O_3 were expended. A clear equilibrium is observed with the reaction rates plateauing. No C12A7 or C5A3 formation is observed during the isothermal dwell at 1200 °C in a high vacuum environment. The C3A formation occurs rapidly initially but approaches a maximum value before 1200 °C. CA phase formation continues with the largest increase in wt.% observed at 1200 °C. Isothermal master plots characterize of the rate of CA formation during this isothermal segment and reveal a clear exponential decay of reaction rate characteristic of diffusion-based transformations, Figure 35. Under vacuum conditions the thermodynamic equilibria favors C3A and CA phase formation, however, diffusion based kinetics is the main impediment to full CaO and Al_2O_3 reaction to form C3A and CA. Milled SSS

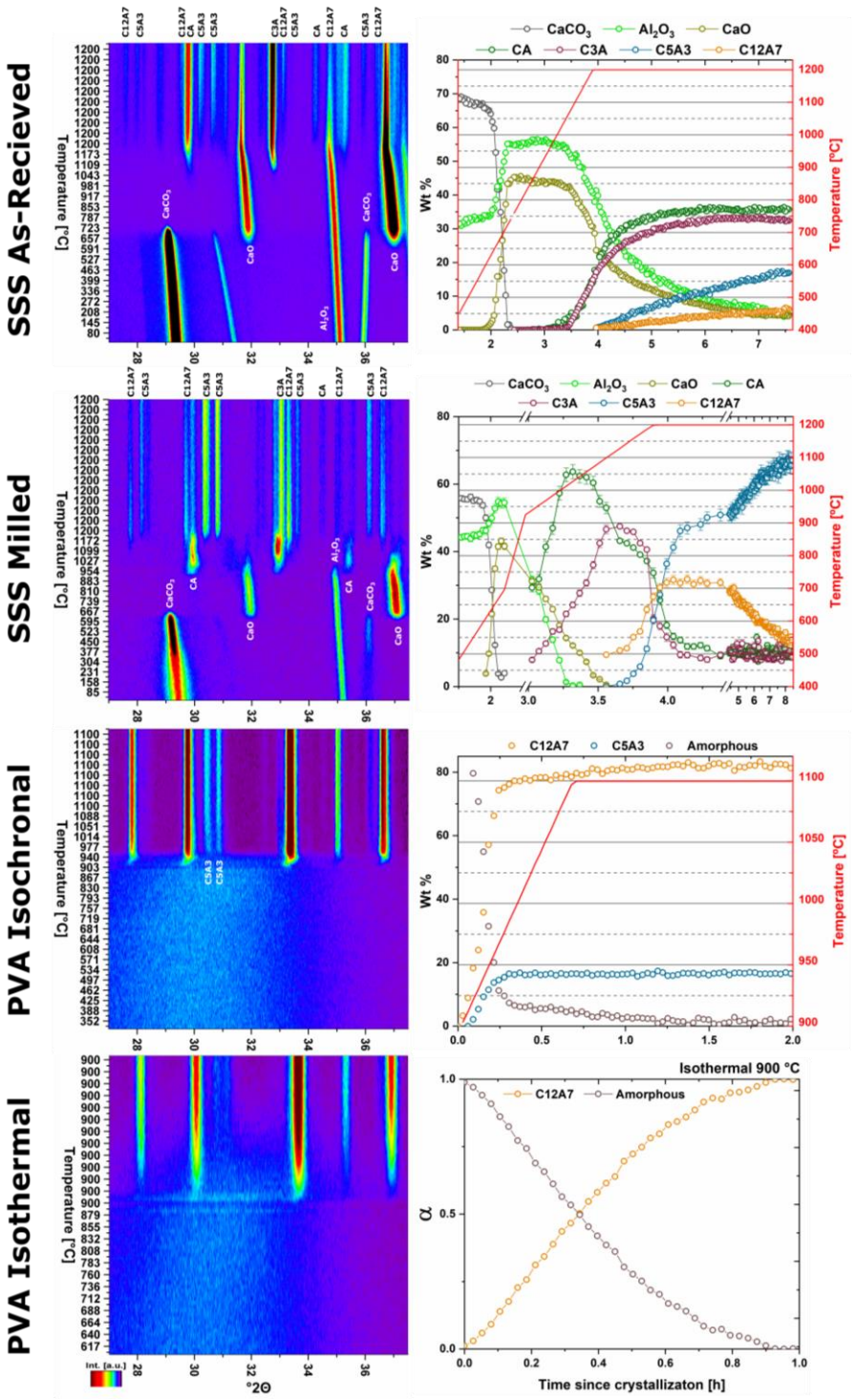

Figure 31 HTXRD data showing peak evolution (left) and quantitative phase determination (right) of high heterogenous as-synthesized SSS, low heterogenous milled SSS, homogeneous PVA (isochronal and isothermal) reactants under dry conditions.

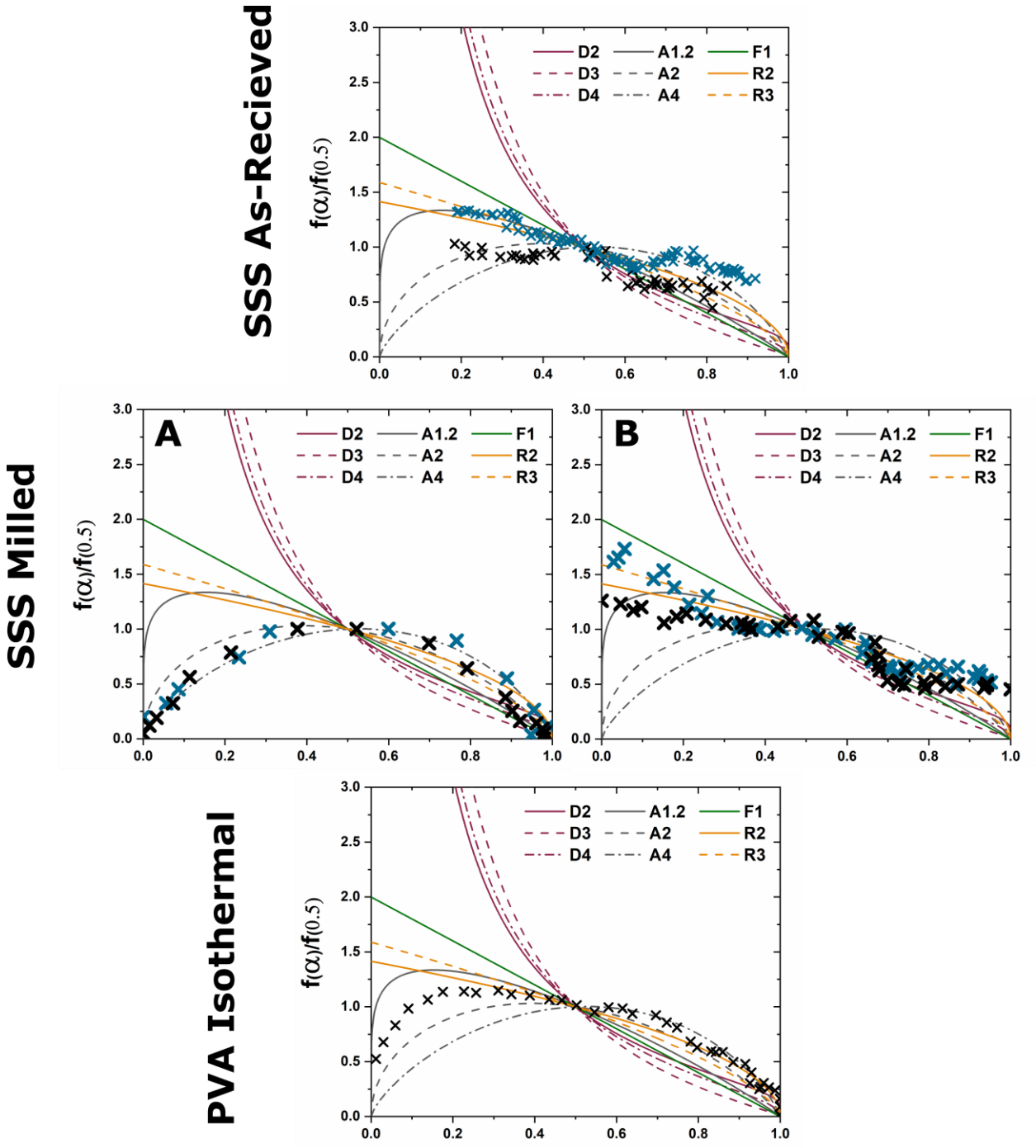

Figure 32 Isothermal master plot of C12A7 formation (black markers) and C53 formation (blue markers) from as-received solid-state reactants (top), initial C12A7/C5A3 formation (middle A) and latter C12A7 decomposition and C5A3 formation (middle B) from milled solid-state reactants, and PVA reactants (bottom) under dry conditions.

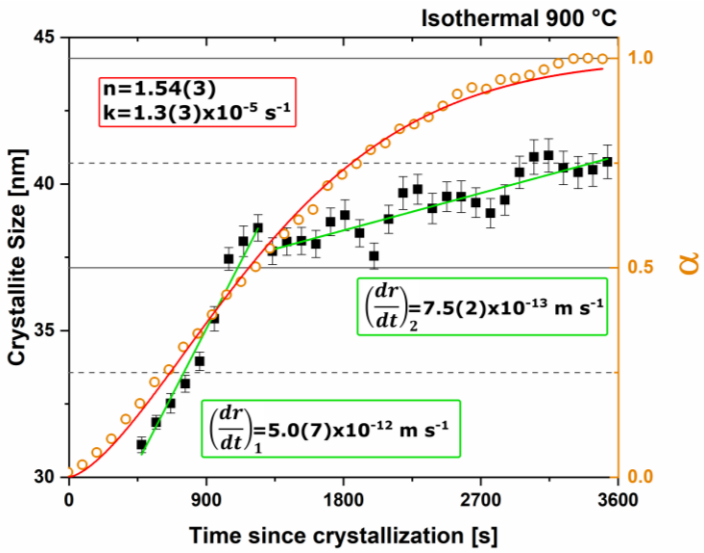

Figure 33 For the isothermal PVA investigation under dry conditions the fit of the Avrami model to α (orange markers) is observed in red with a n value of 1.54(3) and rate constant of 1.3(3)x10-5 s-1 and the change of microstructural crystallite size (black markers) shows a clear two stage growth mechanism with linear relationships, green trend lines, yielding a radial growth rates of 5.0(7)x10-12 m/s and 7.5(2)x10-13 m/s for the first and second growth stages, respectively.

reactant studies were unable to be performed under vacuum conditions due to the rapid evolution of CO_2 gas during $CaCO_3$ decomposition and vacuum level instability.

When atomic reactant homogeneity is achieved with the sol-gel reactants C12A7 phase formation is observed directly from the amorphous precursor at 960 °C, **Figure** 34. This is an increase in the onset temperature of C12A7 formation by 60 and 110 °C in dry and ambient atmospheres, respectively. C3A and CA phase formation occurs concurrent with C12A7, but the rate of phase formation of C12A7 mirrors that observed under ambient and dry conditions albeit at a higher temperature. As the isochronal characterization continues with an isothermal dwell at 1100 °C C5A3 formation at the expense of C12A7 is observed as process time is extended. Under isothermal conditions at the onset of formation, 960 °C, the C3A and CA phase formations are initially delayed and no C5A3 formation at the expense of C12A7 is observed at these temperatures, **Figure** 34. The isothermal master plot of C12A7 formation indicates the rate of reaction correlates well with a JMAK type kinetic transformation consistent with previous characterizations under dry and ambient atmospheres, Figure 35. Fitting α to the Avrami equation a n value of 1.2(3) and a rate constant, k, of $1.8(3)x10^{-4}$ s^{-1} is determined, Figure 36. This demonstrates a further decrease in the n exponent and an order of magnitude increase in the rate constant compared to those observed under dry conditions. Microstructural evolution demonstrates a two-stage growth process, Figure

36, similar to that observed for dry conditions. Initially, for low levels of crystallization, rapid coarsening of crystallite size from 35 to 52 nm is observed at a rate of $(dr/dt)_1 =$ 1.0(4)x10^{-11} m/s followed by a slow increase from 52 to 57 nm over a 2 h isothermal dwell with a rate of $(dr/dt)_2 = 4.8(3)\text{x}10^{-13}$ m/s. The first stage rate of crystallization and the increase in size is higher than under dry conditions; this is likely correlated to the increase in isothermal characterization temperature. The second stage growth rate is similar in magnitude to that observed under dry and ambient conditions with a limited increase in crystallite size of approximately 7 nm from 51 to 58 nm. Under vacuum conditions direct formation of C12A7 is observed with secondary phases (<20 wt%) at 960 °C and eventual phase instability leads to decomposition at 1100 °C

3.5 Discussion

The change in reactant homogeneity has no effect on the thermodynamic equilibrium. Given sufficient time for the kinetics and diffusion to occur, all systems should reach the same final state for a specified temperature. The change produced by altering reactant homogeneity alters the kinetic behavior and pathway to that final state. Characterization of stoichiometrically C12A7 reactant mixtures as a function of reactant homogeneity and processing atmosphere leads to changes in C12A7 formation, elucidates the atmosphere dependent thermodynamic equilibrium and role of C5A3 in the calcium aluminate system, and defines the low temperature kinetic equilibrium of C12A7 regardless of the thermodynamic equilibrium.

3.5.1 Kinetics Pathways of Formation

The kinetic pathway toward C12A7 equilibrium displays changes in the rate of reaction and a decrease in temperature; The following discussion pertains to ambient atmosphere characterization. Large reactant heterogeneity exists when the $CaCO_3$ particles are orders of magnitude larger than the Al_2O_3 particles. In this case, the kinetic pathway demonstrates evolution through off-C12A7 stoichiometry phases C3A and CA with the latter Al-rich phase showing a larger concentration. C12A7 formation is not observed until approximately 1200 °C and the system approaches equilibrium, which violates the Gibbs phase rule, of C3A, CA, and C12A7. The kinetic behavior shows clear diffusion-type behavior as the diffusion pathways are long and grow longer with continued formation of C12A7. This is typical behavior for solid-state reaction synthesis and results in the need of the iterative process of firing, grinding, and pressing usually implemented to disrupt this long diffusion pathway and facilitate reaction of the off-stoichiometry phases.

The alternative to grinding after the initial reaction is milling the initial starting reactants to lower the degree of mixture heterogeneity. In this study the reactants are milled until both $CaCO_3$ and Al_2O_3 reactants have particle sizes on the order of 100 nm. This reduction in heterogeneity, when compared to the high heterogenous as-received reactants, leads to a reduction in the formation temperature by 15% to approximately 1000 °C with most of formation occurring above 1050 °C. The kinetic pathway follows

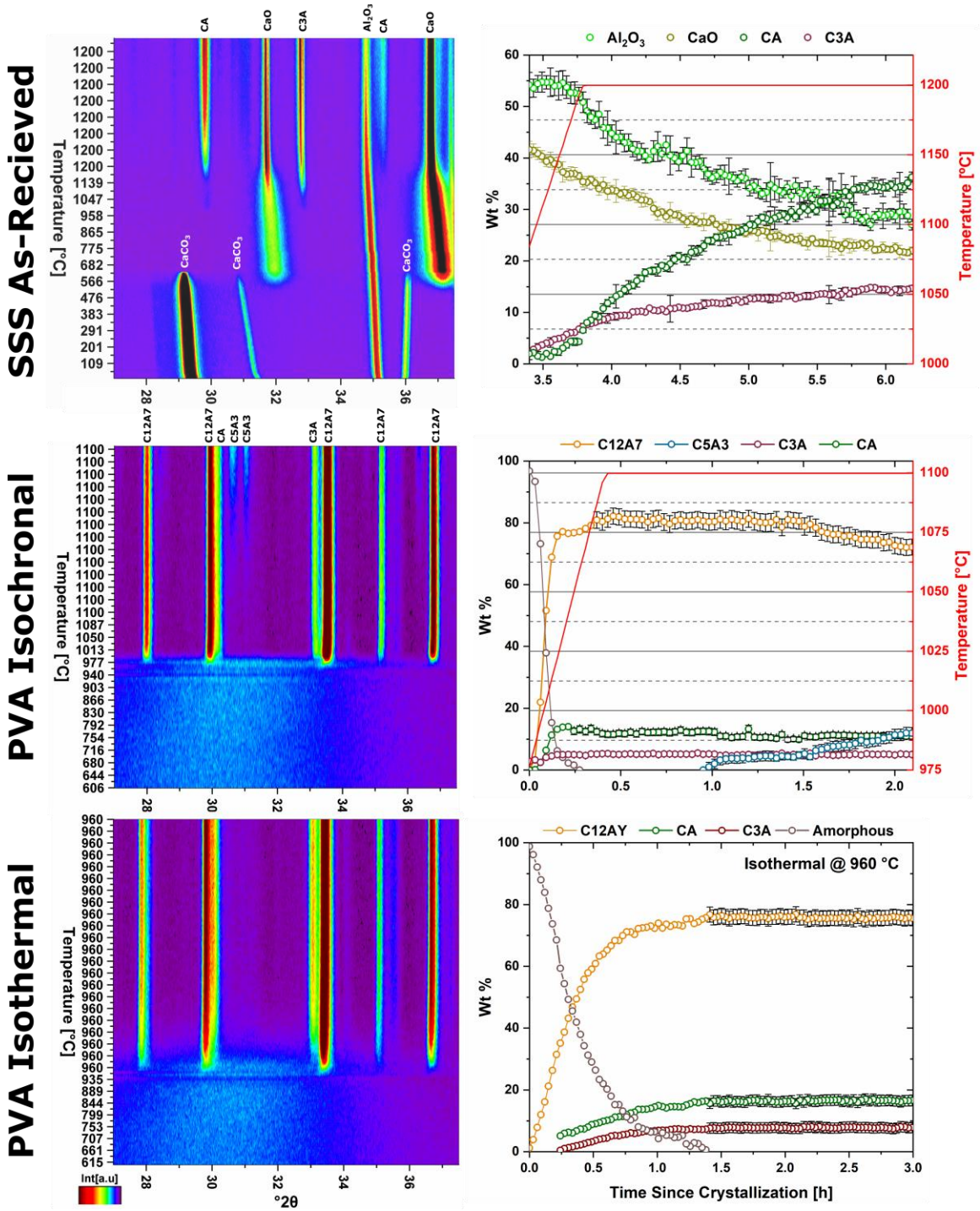

Figure 34 HTXRD data showing peak evolution (left) and quantitative phase determination (right) of high heterogenous as-synthesized SSS and PVA (isochronal and isothermal) reactants under vacuum conditions.

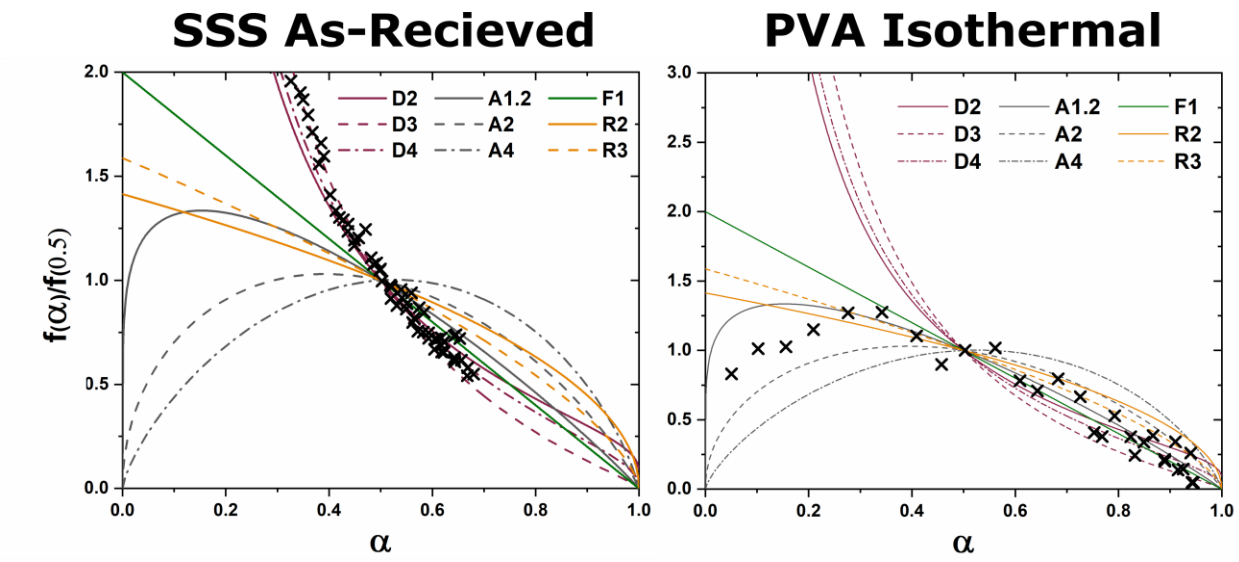

Figure 35 Isothermal master plot of CA formation from as-received solid-state reactants (left) and C12A7 formation from PVA reactants (right) under vacuum conditions.

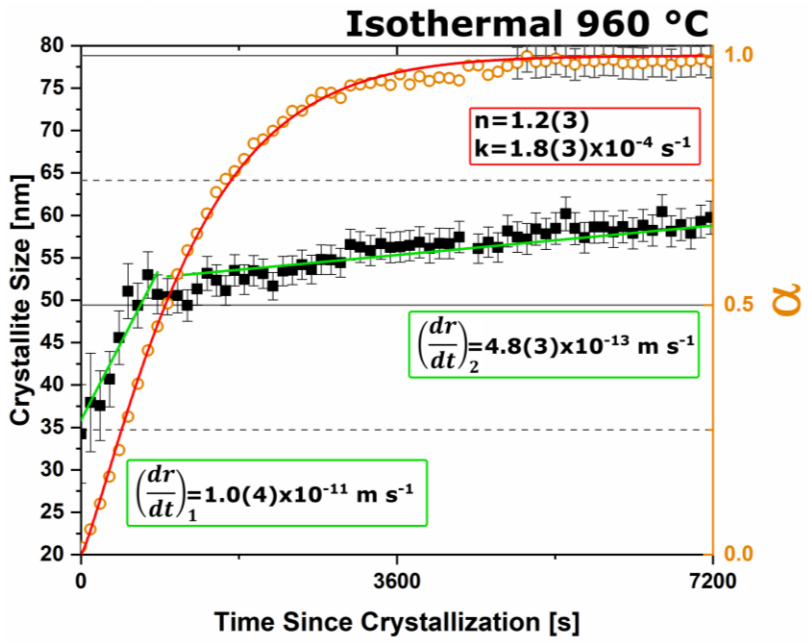

Figure 36 For the isothermal PVA investigation under vacuum conditions the fit of the Avrami model to α (orange markers) is observed in red with a n value of 1.2(3) and rate constant of 1.8(3)E-4 s^{-1} and the change of microstructural crystallite size (black markers) shows a clear two stage growth mechanism with linear relationships, green trend lines, yielding a radial growth rate of 1.0(4)x10^{-11} m/s and 4.8(3)x10^{-13} m/s for the first and second growth stages, respectively.

the same route through off-stoichiometric C3A and CA phases, however, the rate of formation of these phases and C12A7 is drastically increased. The ultimate C12A7 concentration of > 90 wt.% achieved after 0.5 h. A non-equilibrium state of C3A, CA, and C12A7 is observed but the concentration of C12A7 has more than doubled. The type of kinetic transformation cannot be determined as the formation occurs in a non-isothermal region, but under dry conditions a JMAK type kinetic formation is observed which can be assumed to be the type of kinetic transformation under ambient conditions as well. This indicates that nucleation and growth of the C12A7 phase, rather than long-range diffusion, is the limiting factor in phase formation.

If the highly heterogenous solid-state reactant mixture represents the extreme of heterogeneity, an amorphous sol-gel reactant represents the opposite extreme, where atomic level homogeneity eliminates reactant heterogeneity. The formation temperature of C12A7 is reduces 30% from the heterogeneous extreme to 850 °C with C12A7 being the first and only crystalline phase to form. Previously, thermodynamic studies have proposed the pathway through C5A3 and C3A to be the low temperature formation pathway [65,66]. For homogeneous reactants, this pathway is not present. At these low temperatures, diffusion does not readily occur and kinetically favorable phases, which are often disordered, lower-density phases, will form [128]. In the calcium aluminate systems C3A ($\rho_{theoretical}$ = 3.064 g/cm^3), C5A3 ($\rho_{theoretical}$ = 3.067 g/cm^3), and CA ($\rho_{theoretical}$ = 2.94 g/cm^3) are all ordered higher-density phases while C12A7 ($\rho_{theoretical}$ = 2.68 g/cm^3) forms a disordered clathrate structure with a large amount of crystallographic void space [23,44,141,142]. Therefore, there is no precursor crystalline phase and C12A7 is the only favorable phase to form at low temperature. The kinetic formation of C12A7 under these conditions exhibits JMAK type behavior with an n value approaching 2 suggesting 2-D interface-controlled growth. The lack of diffusion driven thermodynamic behavior leads to a slowly evolving microstructure with crystallite size of ~40 nm. The limit to the formation of C12A7 is how quickly the species can migrate across the interface of the growing nucleate.

A physical relationship between reactant homogeneity and the observed behavior is shown in Figure 37. In the heterogenous reactant case (Figure 37A) a large portion of the Ca stoichiometry is trapped at the center of the large $CaCO_3$ particles and is essentially blind to the ensuing reactions after decomposition to CaO. This leads to local Al rich regions and highly reactive Al_2O_3 particles due to their higher surface area explaining the preferential formation of the aluminum rich CA phase. The long distance to the Ca stoichiometry limits the reaction yielding diffusion-limited kinetic behavior.

When the particle size is reduced as in Figure 37B, both reactants have equivalent surface area and reactivity leading to high nucleation and growth of the thermodynamically favored C12A7 phase. The shorter diffusion pathways change the limiting kinetic behavior from the availability of stoichiometry to the nucleation, growth, and impingement of nucleates; This is a process that requires less energy, lowering the formation temperature and accelerating the reaction.

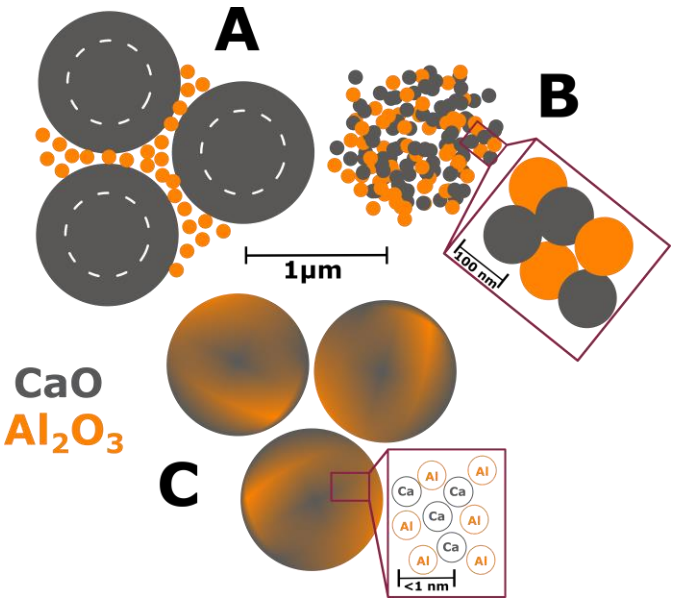

Figure 37 Schematic of reactant homogeneity with Ca species in gray and Al species in orange. High heterogenous solid-state reactants (A), low heterogeneity milled solid state reactants (B), and amorphous atomically homogeneity polymer assisted sol-gel reactants (C). The white circles in the high heterogenous reactant particles demonstrates the blind region of stoichiometry whose diffusion pathways are too long to effectively play a role in the phase formation reactions.

When reactant heterogeneity is removed, and atomic homogeneity is achieved as in Figure 37C**,** formation of C12A7 requires the diffusion of atoms on the order of single atomic spacings. The kinetic behavior is also controlled by the nucleation, growth, and impingement of nuclei giving the observed JMAK behavior. The controlling kinetic process in C12A7 formation is dependent on reactant heterogeneity and diffusion of cationic anionic pairs; indicating a microstructural and processing behavior which varies as the reactant mixture changes. The intrinsic behavior of the system without microstructural influence is revealed if diffusion is not required. Under these conditions C12A7 is the only phase to form as it is the most disordered and lowest density calcium aluminate phase and kinetically favorable to form at low temperatures.

3.5.2 C12A7 Atmospheric Effects on Thermodynamic Stability

The role of process atmosphere has a significant, systematic effect on the stability and occluded anion chemistry of the C12A7 structure and by correlation its properties and application. C12A7 is the thermodynamically favorable structure under humid, ambient conditions. Furthermore, the literature thoroughly establishes that the C12A7 structure is thermodynamically unfavored in non-humid atmospheres (e.g. dry or vacuum conditions) at elevated temperatures (>1050 °C). This includes both thermodynamically calculated phase diagrams and experimental results [10,42]. The

kinetic characterization for dry (~150 ppm H_2O) and vacuum atmospheres reported herein supports the instability of C12A7 under non-humid atmospheres but details a formation pathway contrary to that reported in thermodynamic studies. Under dry conditions the formation of C12A7 occurs but it is only an intermediary phase in route to the final C5A3 thermodynamic equilibrium. Under vacuum conditions no C12A7 forms and by correlation no C5A3 leading to a C3A and CA thermodynamic equilibrium.

With heterogenous reactants under a dry atmosphere the formation pathways remain the same as under ambient conditions albeit with an additional step in the kinetics related to the decomposition of C12A7 to the thermodynamically favored phase C5A3. When heterogeneity is high C12A7 formation and C5A3 formation occurs slowly due to the diffusive nature of the formation process. As the reactants are milled and heterogeneity is decreased the formation of C12A7 and C5A3 initially occur with JMAK type kinetic behavior leading to rapid phase formation. The formation of C5A3 follows the formation of C12A7 with an increase in temperature supporting the decomposition of C12A7 to C5A3 formation mechanism. Comparison of the extended behavior at 1200 °C confirms this reaction; a linearly decreasing rate is observed, consistent with a particle conversion process. Initially JMAK type behavior is observed as C5A3 nucleates on the outside of the C12A7 particles. As the formation process proceeds, the inward conversion of the C12A7 particle leads to a change in the limiting kinetic process**,** Figure 38.

With heterogenous reactants under a vacuum atmosphere only the high-heterogeneity characterization was performed to protect vacuum integrity. No C5A3 formation from C12A7 was observed. The combined long-diffusion pathways and lack of

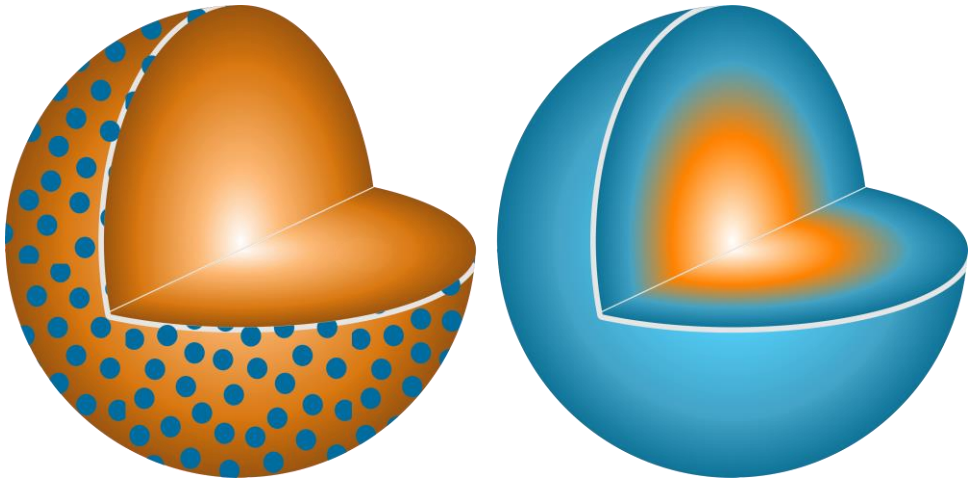

Figure 38 Schematic representation of JMAK nucleation (left) and particle conversion (right) of C12A7 to C5A3. As the transformation proceeds with increased time the kinetic formation proceeds from nucleation to particle conversion.

atmospheric oxygen further precludes C12A7 formation, with oxygen as the occluded anion, which prevents the kinetic decomposition and transformation to C5A3. C5A3 itself does not appear to form from C3A and CA indicating it is only favorable to form through the kinetic pathway with C12A7 as an intermediary phase.

This represents a shift in the understanding of the C12A7 phase space where C5A3 and C3A are currently reported as the low temperature formation routes to C12A7 and to calcium aluminates in general [65,66]. In this kinetics studies C5A3 was never observed as an intermediary product to C12A7 formation regardless of atmosphere and reactant homogeneity. C5A3 is only a product that is formed through the decomposition of C12A7. This is a discrepancy when considering thermodynamic studies of calcium aluminate formation, however, review of the relevant literature shows that a misclassification of the C12A7 as C5A3 has led to the dialog where C5A3 and C3A are the intermediary phases [65,66]. When this correction is made the results from the thermodynamic studies support the observed kinetic behavior and C5A3 should be considered a decomposition product of C12A7 and not an intermediary phase in the formation of calcium aluminates. The presence of C5A3 indicates a lack of sufficient moisture to stabilize the C12A7 structure after formation at elevated temperatures above 1050 °C.

1.1 C12A7 Atmospheric Effects on Kinetic Stability

Thermodynamic equilibrium drives the system kinetics to the lowest free energy phase; however, the process inherently requires the diffusion of cationic and anionic species in ionic materials. When in a temperature regime where this diffusion is sluggish, the thermodynamic equilibrium may not be achieved due to sluggish kinetics and instead a new kinetic equilibrium exists. The kinetic equilibrium is characterized by phases favored by limited diffusion. As the reactant mixture heterogeneity is removed and atomic level homogeneity is achieved diffusion is no longer the limit to formation and C12A7 is observed as the first crystalline phase at a temperature 30% lower than with heterogenous reactants. C12A7 is the kinetically favored phase to form under ambient conditions and as the atmosphere is changed C12A7 is still the predominant phase to form regardless of the thermodynamic equilibrium characterized at higher temperatures.

Under dry and vacuum environments C12A7 is still the first crystalline phase to form from the amorphous precursor, but the formation temperature is increased from 850 °C under humid environments to 900 and 960 °C for dry conditions and under a vacuum, respectively. This change in temperature also comes with a change in the evolution of the microstructure and fitted JMAK behavior. The change in temperature indicates a change in the activation energy for C12A7 formation indicating a change in the formation process as a function of atmosphere. Initially hydration and the hydroxide occluded anion play a role in the formation kinetics. When this moisture is removed the increase in temperature indicates that the formation of just oxygen occupied cages has a higher activation energy. The further increase in temperature with the removal of

oxygen partial pressure can be characterized by a change in the occluded anion source from the atmosphere to purely the reactant mixture. This process requires solid state rather than atmosphere-solid interface diffusion leading to the higher observed formation temperature correlated to a higher activation energy.

The change in the source of the anionic species leads to the observed change of the fitted kinetic parameters. A two-stage nuclei-growth behavior is observed under dry and vacuum conditions where rapid growth is observed for the first 50% of the transformation followed by a slower growth rate that is equivalent to the growth rate under ambient humid atmospheric conditions. The change is the removal of moisture and the lack of hydroxide occupied cages. In C12A7 the rate of diffusion for O^{2-}vs $OH^{-}$is higher allowing for rapid diffusion of oxygen [7,10]. The diffusion within ionic materials requires the co-diffusion of cation and anionic species. With this change in occluded anion mobility the extra framework oxygen can quickly diffuse to the growing particle interface, which facilitates the diffusion of the just cationic species, rather than the combined diffusion of anionic and cationic species, to lead to further growth. In the presence of rapid diffusion of oxygen to the surface of the C12A7 particle, only the diffusion of cationic species is required.

This is the first report of crystallization of C12A7 in a non-carbonaceous vacuum environment and is achieved by limiting the expression of the thermodynamic equilibrium in favor of the kinetic equilibrium; this raises the issue of the source of the occluded anion which has historically been correlated to the atmosphere. The decomposition of PVA results in an amorphous low C content precursor which is white in color after calcining at 600 °C. The PVA reactant consists of Ca-O and Al-O complexes with no long-range order and when viewed stoichiometrically CaO and Al_2O_3 requires no additional oxygen to reach oxy-C12A7 stoichiometry.

$$7\ \mathrm{Al_2O_3} + 12\ \mathrm{CaO} \rightarrow \mathrm{Ca_{12}Al_{14}O_{33}}$$

When diffusion pathways are short this extra oxygen could be used to template the cages and form C12A7 without the addition of atmospheric oxygen. This observation represents a fundamental shift in the perception that no template anion is present in reducing non-oxidizing atmospheric conditions. The compromise for sourcing the stabilizing anion from the reactant mixture is the needed increase in energy to promote diffusion which leads to a formation temperature 110 °C higher than under a humid environment; this also enters an energy regime where the thermodynamic equilibrium can be expressed leading to the concurrent formation of C3A and CA. When atomic homogeneity exists, the short diffusion pathways allows for reactant mixture occluded oxygen to template the C12A7 structure under vacuum conditions.

3.6 Conclusion

In-situ rapid XRD data provide real time insight into the kinetics of solid state phase transformations and represents a valuable tool to further understand the evolution of materials toward thermodynamic equilibrium. Through this characterization

a new understanding of the evolution of phase formation and thermodynamic and kinetic stability of various calcium aluminates and especially C12A7 formation has been presented.

The kinetics and process variables for calcium aluminate formation is directly related to the physical heterogeneity of the reactant mixture. By decreasing reactant heterogeneity, the rate of reaction and the temperature of phase formation can be controlled. When reactant homogeneity is eliminated C12A7 no longer requires intermediary crystalline phases and forms directly form the reactant mixture. It was previously understood that C5A3 and C3A along with C3A and CA were preferred formation pathways to C12A7 and that C5A3 and C3A are the initial intermediary phases to all calcium aluminates. In-situ kinetic studies highlight that this is not the case and that C3A and CA and direct crystallization to C12A7 are the formation pathways under heterogenous and homogeneous conditions, respectively. C5A3 is a decomposition product of C12A7 and is only observed to form through a kinetic pathway related to a particle conversion transformation.

The thermodynamic equilibrium for a Ca:Al ratio of 12:14, given enough time for all kinetic processes to complete, is as follows:

1. **Ambient Conditions:** C12A7
2. **Dry (≤150 ppm H_2O) Conditions:** C5A3 through C12A7 particle conversion process
3. **Vacuum Conditions**: C3A and CA

The thermodynamic equilibrium is contrasted by the kinetic equilibrium observed at temperatures below 1000 °C with a homogeneous reactant mixture. C12A7 is the predominate phase (≥80 wt%) to form under ambient, dry, and vacuum conditions. When the temperature is raised the thermodynamic equilibrium ultimately results with decomposition of C12A7 to C5A3 under dry and vacuum conditions; the rate of decomposition is higher under vacuum conditions. The presence of C12A7 formation under vacuum conditions demonstrates that the anion source is not solely derived from the process atmosphere but also from the reactant mixtures. This is the first reported formation of C12A7 under vacuum conditions due to the favorable kinetic conditions. With the correlation of reactant heterogeneity and process atmosphere understood synthesis and processing of calcium aluminates including the highly functional C12A7 can be better controlled for desired micro and atomic structured products.

CHAPTER 4
Direct Synthesis and Structural Characterization of Electride C12A7 formation in a Carbonaceous Vacuum Environment

4.1 Abstract

$Ca_{12}Al_{14}O_{33}$ (C12A7 or Mayenite) is a material whose caged clathrate structure and occluded anionic species leads to significant functionality. The creation of occluded anionic vacancies leads to the injection of localized electrons at the center of the cage, converting the wide band gap insulator to a semi- or metallic conducting material. The conversion to the electride historically requires the synthesis of oxy-C12A7, consolidation, and then reduction to introduce anionic vacancies. This report develops and characterizes a direct electride synthesis procedure from either heterogenous solid state reactants ($CaCO_3$ and Al_2O_3) or homogenous non-carbonaceous polymer assisted sol-gel reactants. Electride-C12A7 formation is observed in a vacuum furnace where the reactants are in direct contact with a carbon source. Process time and temperature dependent characterization provides insight into the source of high temperature C12A7 stability, the mechanism of anionic vacancy formation, and the magnitude of ultimate conductivity, which cannot be explained by current reduction theories. A new theory is presented where mixed O and C occupied cages lead to high temperature stability, oxidation of C species creates anionic vacancies, and an equilibrium between the reducing power of the electride-C12A7 and of the C species leads to the ultimate conductivity achieved by the process. This represents a shift in understanding of the carbonaceous reduction process and the first report of high purity electride-C12A7 direct synthesis from solid state reactants and non-carbonaceous polymer assisted sol gel reactants.

4.2 Introduction

The mineral mayenite, also known as C12A7 and chemically $\mathrm{Ca_{12}Al_{14}O_{33}}$, has gained attention in last two decades due to the high degree of functionality afforded by the crystal structure. C12A7 crystallizes in the highly symmetric, $I\bar{4}3d\ (\mathrm{no.}220)$, space group with *a* = ~11.98 Å and two formula units per unit cell resulting in 118 atoms within the unit cell. The functionality of the material results from the clathrate structure where the unit cell is made up of a positively charged framework of twelve interconnected cages and occluded stabilizing anions. These anions within the cage are weakly bound to the framework leading to a [Framework]:Occluded-Anion notation, $[\mathrm{Ca_{24}Al_{28}O_{64}}]^{4+}:2O^{2-}$. Manipulating cationic doping of the framework and mobile occluded anions in C12A7 leads to potential applications in inorganic and organic synthesis, surface treatments, catalytic reactions, as a high purity and high density anionic source, transparent conductive oxide, direct writable transparent wires and media, luminescent for displays, lighting, or photoelectric devices, gas and biomass reforming, and even an antibacterial agent among numerous other applications; Liao et al. present a comprehensive review on the potential applications of the stoichiometric $[\mathrm{Ca_{24}Al_{28}O_{64}}]^{4+}:2O^{2-}$ as well as its derivatives [42].

Hosono et al. have conducted extensive research on C12A7 most notably on the formation of the $[\mathrm{Ca_{24}Al_{28}O_{64}}]^{4+}:\mathrm{e}^{-}_{(2*\partial)}\mathrm{O}^{2-}_{(1-\partial)}$ derivative [3,61]. The stabilizing O^{2-} anion is

replaced by electrons which are localized in the “potential well” created by the cationic cage leading to the classification of an electride. C12A7 was the first room-temperature stable inorganic electride bringing the realization and application of electrides to ambient conditions [36]. The formation of the electride seems to be robust with many different formation routes all focusing on processing C12A7 in the presence of a preferentially oxidized sacrificial target, known in this context as an “oxygen getter” [156]. The most practical methods involve utilizing carbonaceous environments due to experimental ease and lack of post processing of previously synthesized and consolidated samples. This research analyzes the structural changes associated with processing as-synthesized oxy-C12A7, $[\mathrm{Ca_{24}Al_{28}O_{64}}]^{4+}:2\mathrm{O}^{2-}$, to electride C12A7, $[\mathrm{Ca_{24}Al_{28}O_{64}}]^{4+}:\mathrm{e}^{-}_{(2*\partial)}\mathrm{O}^{2-}_{(2-\partial)}$, and identifies a new theory explaining the mechanisms for electride formation and lack of full conversion ($\partial = 2$).

The stoichiometric compound, $[\mathrm{Ca_{24}Al_{28}O_{64}}]^{4+}:2\mathrm{O}^{2-}$ is an invariant binary compound in the $\mathrm{CaO}-\mathrm{Al_2O_3}$ system at approximately 37 mol% $\mathrm{Al_2O_3}$,Figure 39. On either side is a two-phase region containing C12A7 and two other invariant binary compounds $\mathrm{Ca_3Al_2O_6}$ (C3A) and $\mathrm{CaAl_2O_4}$ (CA). The compound $\mathrm{Ca_5Al_6O_{14}}$ (C5A3) is meta-stable and is frequently discussed in the literature when dealing with the C12A7 system. Thermodynamic solid state synthesis investigations into the formation of C12A7 from $\mathrm{CaCO_3}$ and $\mathrm{Al_2O_3}$ found that the first phases to crystalize are C5A3 and C3A with the former being favored as reactant homogeneity increases [65,66]. The C5A3 concentration increases until approximately 950 °C after which C5A3 is consumed in favor of the formation of C12A7. C5A3 and C12A7 are close in stoichiometry, $7\mathrm{Ca_5Al_6O_{14}} + \mathrm{CaO} \rightarrow 3\mathrm{Ca_{12}Al_{14}O_{33}}$, and crystal structure. Both structures contain octahedrally coordinated Ca and tetrahedrally coordinated Al cations, but C5A3 is an ordered layered structure while C12A7 is a disordered clathrate structure, Figure 40. As the temperature is increased the formation of CA occurs until approximately 1200 °C when C3A and CA combine to form C12A7 [66]. These observations suggest there are two formation pathways from solid state reactants: (1) C5A3 + C3A at low temperatures (<900 °C) when cationic species are well mixed [67,130] and (2) C3A + CA at high temperatures (>1100 °C) observed when long diffusion lengths of reactants are present [65,66]. Recent in-situ kinetic studies suggest that different pathways might occur with C12A7 being a kinetically favorable phase to form directly at lower temperature and C5A3 only observed as a decomposition product of C12A7 [157].

The relationship between C3A, CA, and C5A3 is further elucidated when investigating the decomposition of C12A7. The presence of occluded anions is heavily correlated to the stability of the clathrate structure, and in the absence of any template anions, i.e. in dry reducing conditions, C12A7 is not thermodynamically favorable and decomposes. This was first observed in single crystal growth experiments where moisture or oxygen was needed in order to nucleate the C12A7 framework. The decomposition products were reported to vary based on process temperature and were either C5A3+C3A or C3A+CA; A historical summary of formation products in various oxidizing, reducing, inert, dry, and hydrated atmospheres has been compiled by Kim et

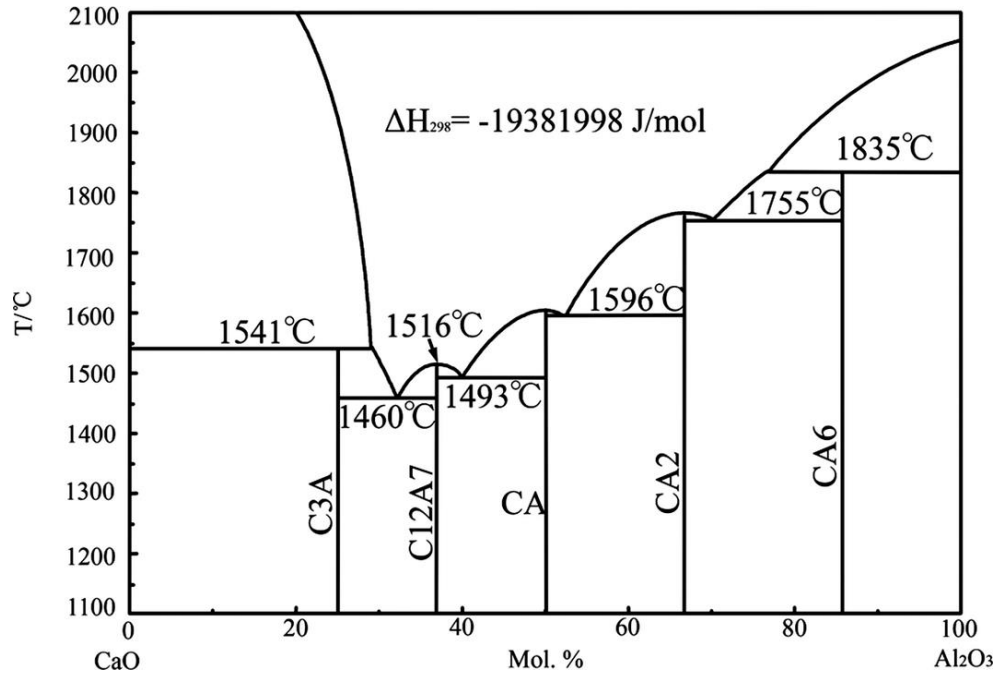

Figure 39 Calculated CaO-Al2O3 phase diagram under ambient "humid" synthesis conditions from Liao et al. [42]

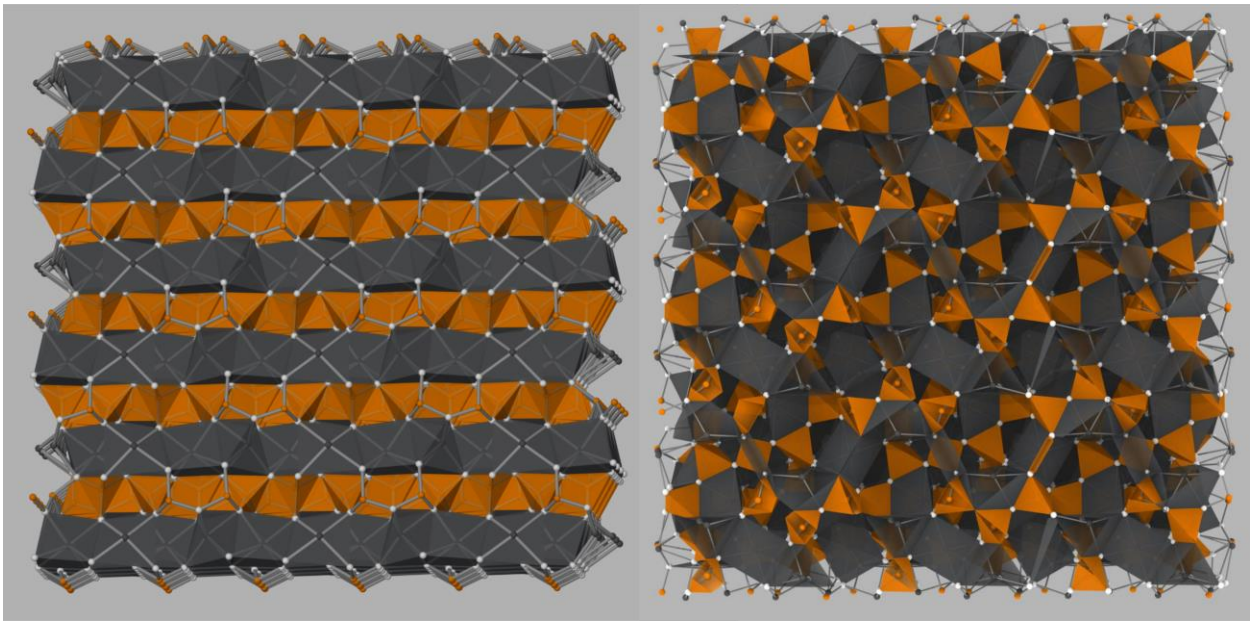

Figure 40 Comparison of the ordered layered C5A3 structure (left) and the C12A7 cage structure (right). Ca cations and coordination polyhedra are shown in gray, Al cations and coordination polyhedra are shown in orange, and oxygen anions are shown in white. Reproduced from Salasin and Rawn [156].

al. [5,158]. As the breadth of electride formation research grows the decomposition of C12A7 continues to limit electride formation at elevated processing temperatures for long process durations. Palacios et al. observed the electride formation and subsequent decomposition of electride-C12A7 powder to C5A3 and C3A through in-situ neutron diffraction in a V sample holder heated to 1100 °C under vacuum [48]. Ali et al. observed C12A7 decomposition during electride formation of float zone (FZ) single crystals sealed in an evacuated quartz ampule with Ti powder and fired at 1200 °C for 48 h [73]. Eufinger et al. conducted a study to identify the diffusion of various anions in the C12A7 structure and discovered a correlation to humidity and decomposition of the C12A7 framework [10]. A decomposition analysis found that under dry conditions C12A7 decomposes at temperatures above 1050 °C which is correlated to the critical mobility limit for Ca ions [10]. This decomposition was observed in both inert and oxidative atmospheres; decomposition times were greater than 24 h. The decomposition products of C3A+C5A3 or CA+C3A were observed and correlated to the temperature and atmosphere conditions during the initial temperature ramp [10]. Decomposition was found to nucleate at the macroscopic crystal defects which agrees well with the calculated Avrami exponent by Palacios et al. suggesting that the limiting rate step of decomposition is the growth of the decomposed products around the C12A7 phase and not the random nucleation of C5A3 products [10,48]. These decomposition times and temperatures agree with those observed in the reduction experiments, but the vacuum and reducing environments may lead to an increase in the rate of the decomposition reaction. Just as in the formation of C12A7 there are two decomposition pathways: (1) C5A3 + C3A and (2) C3A + CA.

Conversion to $[\mathrm{Ca}_{24}\mathrm{Al}_{28}\mathrm{O}_{64}]^{4+}:\mathrm{e}^{-}_{(2*\partial)}\mathrm{O}^{2-}_{(2-\partial)}$ occurs primarily by the reaction of the occluded oxygen with an oxygen getter [156]. As the electride formation occurs sample color transitions from white, through green, to black and the electrical conductivity transitions through an insulating, semi-conducting, and metallic conducting regime, respectively [158]. One oxygen getter reduction method involves processing the synthesized C12A7 powder, single crystal, thin film, consolidated sample, etc. in a C crucible under flowing inert gas. This generates a strong reducing atmosphere in the crucible leading to the proposed reduction of the sample by the following reaction $O^{2-}_{(cage)} + CO_{(g)} \rightarrow CO_{2(g)} + 2e^{-}_{(cage)}$ [60]. This is favorable leading to a conversion with no post processing, but the degree of reduction attainable is not well reported or discussed and it appears that only limited conversion of O^{2-} to e^{-} occurs. The other proposed C based reduction method involves the replacement of the occluded $\mathrm{O}^{2-}$by C_2^{2-}which has a similar radius, 1.4 and 1.2 Å, respectively, and valence [30,159]. The carbide anion is then hypothesized to be instantaneously unstable or unstable during cooling and decomposes to either solid C or CO gas creating anionic vacancies and forming the electride. The pathway to anionic exchange is not clear and appears to not be an exchange but a full recrystallization of the decomposition products to C12A7, indicating that decomposition of $[\mathrm{Ca}_{24}\mathrm{Al}_{28}\mathrm{O}_{64}]^{4+}:2\mathrm{O}^{2-}$, needs to occur before $[\mathrm{Ca}_{24}\mathrm{Al}_{28}\mathrm{O}_{64}]^{4+}:2C_2^{2-}$formation and electride conversion can occur [30]. The realization of

a full recrystallization process yields promise for direct synthesis of electride-C12A7. The direct formation of electride-C12A7 from C3A + CA reactant mixtures has been presented as well as from a carbon rich Pechini sol-gel precursor [30,160,161]. These studies show a clear plateau in electrical conductivity but little theory for this plateau in electronic properties or characterization of the underlying atomic structure has been presented.

This report seeks to study the processing-structure-property relationships of the conversion of oxy-C12A7 to electride-C12A7 as well as the direct synthesis of electride-C12A7 from both conventional solid state ($CaCO_3$ + Al_2O_3) and non-carbonaceous polymer-assisted sol-gel reactants. The polymer-assisted sol-gel reactant mixture also benefits from short diffusion pathways achieved in the Pechini synthesis but instead utilizes the environmental carbon instead of reactant carbon to create a consolidated C12A7 sample with low carbon content. The experiments reported here make use of a carbonaceous environment within a high vacuum furnace that results in a carbonaceous dry (low P_{H_2O}) low-pressure (low P_{O_2}) environment. Temperature and time is controlled to investigate the formation, stability, and degree of reduction obtainable by the carbonaceous reduction processes. The changes in electronic and atomic structure for the conversion from oxy-C12A7 to electride-C12A7 and direct synthesis of electride-C12A7 can be analyzed post-processing; X-ray diffraction (XRD) is used to characterize the change in the atomic structure, scanning electron microscopy (SEM) is used to evaluate microstructural changes, electrical resistivity measurements associate the atomic and microstructural features to electronic properties determining the degree of reduction. The results of this characterization are then used to develop a reduction model involving the formation of a mixed C and O occupied C12A7 caged structure; C is sourced from the outward solid-state diffusion of C from the sample holder and O is sourced from the extra oxygen present in the solid reactants. The O is explicitly not sourced from any gas phase reactant.

4.3 Experimental

The formation of the electride C12A7 will be characterized through three methods; a conversion of as-synthesized oxy-C12A7 to electride-C12A7, direct synthesis of electride-C12A7 from solid state reactants $CaCO_3$ and Al_2O_3, and direct synthesis of electride C12A7 from non-carbonaceous polymer assisted sol-gel reactants are implemented to characterize the process from a variety of starting points for elucidation of electride formation mechanics.

For conversion of oxy-C12A7 to electride-C12A7, oxy-C12A7 was first synthesized using solid state techniques. $CaCO_3$ and Al_2O_3 that were dried in a vacuum oven at 200 °C and 37 torr for 24 h and then stoichiometric amounts of powders were weighed and homogenized in an alumina milling jar with 10 mm diameter PTFE milling beads in a vibratory mill. The powder was then pressed into 30 mm pellets with 58 MPa of uniaxial pressure and fired at 1250 °C for 24 h. Phase equilibria was analyzed with XRD and subsequent firing steps were performed until single phase C12A7 was

obtained. No efforts were taken to avoid moisture uptake during synthesis and likely the oxy-C12A7 phase formed with occluded $O^{2-}$and OH^{-}stabilizing anions. This is not an issue as the dehydration of oxy-C127 will occur during heating [7,10].

For direct synthesis of the electride from solid state reactants $CaCO_3$ and Al_2O_3 were used as the starting materials. Stoichiometric amounts of $CaCO_3$ and Al_2O_3 were mixed in a vibratory mill and used as-mixed for consecutive processing step. No calcination or particle size reduction was performed prior to processing in the vacuum environment.

For direct synthesis of electride-C12A7 from a homogenous reactant mixture a polymer assisted sol-gel route was implemented; the polymer assisted method was chosen over the conventional amorphous citrate or Pechini method for better control over reactant homogeneity and carbon content. Poly vinyl alcohol (PVA) was used in this synthesis and a 4:1 cation to PVA ratio was chosen. The PVA (molecular mass of 20,000-30,000) was dissolved in DI water and allowed to age for 24 h. $Ca(NO_3)_2$•$4H_2O$ and $Al(NO_3)_3$•$9H_2O$ were used as cation sources and were measured from 1 molar stock solutions whose molarities were quantified through inductively coupled plasma (ICP) spectroscopy. Stoichiometric amounts of nitrate solutions were combined with the PVA solution under vigorous stirring. The solution was aged for 1 h before solvent evaporation was performed at a solution temperature of 90 °C. Near the end of solvent evaporation the solution exhibited vigorous bubbling before forming a viscous gel; the bubbling relates to the decomposition of nitrate species. The gel was further heated on the hotplate until completely dried. This powder was then ground in a yttria stabilized zirconia mortar and pestle and calcined to 600 °C and immediately quenched. This ensures oxidation of all carbonaceous residue and the obtained white powder was used as the starting homogeneous reactant mixture for direct electride synthesis.

The formation of electride C12A7, in a carbonaceous environment within a vacuum furnace, was performed from the three starting points according to the process flow summarized in Figure 41. The sample chamber is contained within a stainless-steel vacuum furnace with W heating elements and Mo and W shielding. Powder (1 g) was loaded into a 13 mm graphite die placed in the furnace, Figure 42. A graphitic die was used due to the ability to have a carbon source in direct contact with the entire sample; no pressure was applied during the processing. The sample chamber is under high vacuum, 9.0×10^{-6} torr, leading to a low oxygen and moisture partial pressure. The temperature of the furnace is raised at a rate of 8 °C/min to the target processing temperature of 1000, 1100, 1200, or 1300 °C. The effects of process duration were investigated by increasing the dwell time at the target temperature. The samples furnace cooled under vacuum and were prepared for characterization by removing residual graphite with a diamond grinding disk and mineral oil. After processing the samples underwent a full set of characterization to analyze the crystal structure, microstructure, and electrical properties.

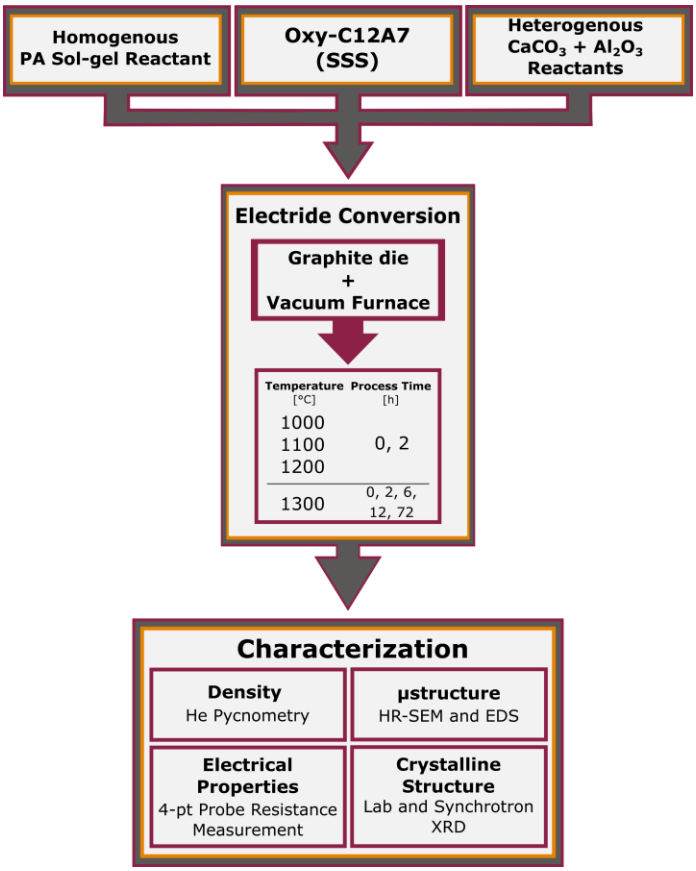

Figure 41 Experimental flow chart for the synthesis, consolidation and electride formation, and characterization.

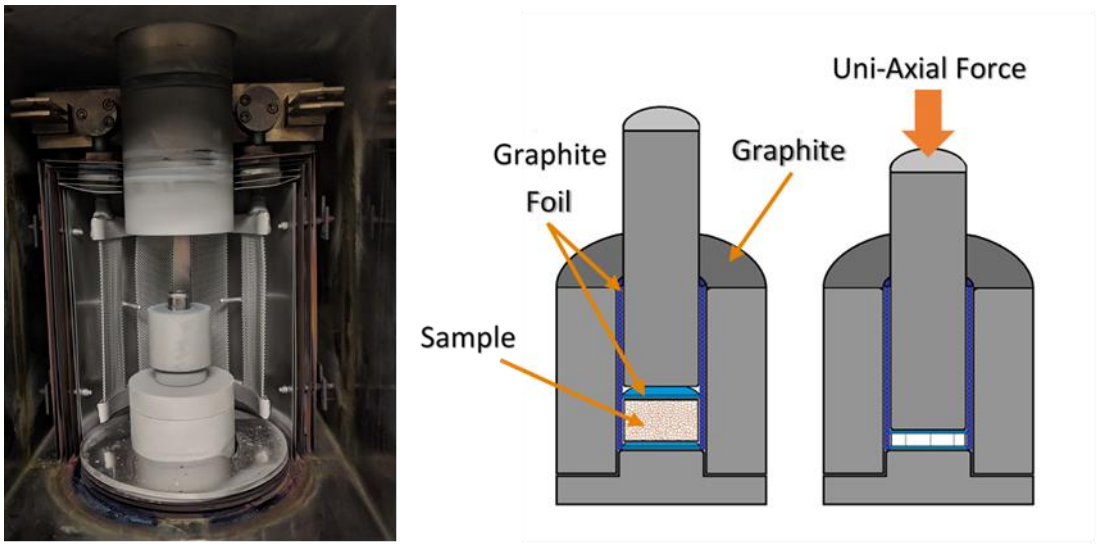

Figure 42 Vacuum furnace (left) and graphite die (right).

XRD data were collected at the Joint Institute for Advanced Materials (JIAM) Diffraction Facility using a PANalytical Empyrean diffractometer in Bragg-Brentano geometry with the reflection spinner stage and the PIXcel^{3D} area detector in scanning line mode. The instrumental collimation utilized a $^1/_8{}^\circ$ divergence slit, $^1/_4{}^\circ$ anti-scatter slit, 0.02 rad soller slit, and 10 mm mask on the incident beam side and a $^1/_8{}^\circ$ anti-scatter slit, 0.02 rad soller slit, and Ni-ß filter on the diffracted beam side. Data were collected from 15-120° 2Θ with a step size of 0.00655° and each step had a 53 second counting time. XRD data were analyzed via the Rietveld method using the GSASII software package [162]. Refined parameters include lattice parameter, sample surface displacement, scale, crystallite size, strain, atomic coordinates, and isotropic thermal parameters; Instrumental broadening was characterized through analysis of NIST SRM 640e (Si). Structural changes as a function of processing parameters were studied; due to the high disorder resulting from various different cage types and heavy correlation between split positions, the thermal parameters were refined isotopically and no attempts were made to refine the fractional occupancies of split positions beyond the basic Ca1 and Ca2 split position [44,156]. To gain better resolution of split positions and occluded position density, select samples were characterized at the powder diffractometer BM-11 at the Advanced Photon Source (APS). Rietveld refinements were performed using the synchrotron data and, with the increasing probed d-space and resolution, Fourier difference maps were generated along the XY plane at z= $^1/_4$. This plane contains the S_4 symmetry axis at the cage center allowing for observation of the scattering density at the cage center and Ca split positions to elucidate these heavily correlated low occupancy split positions and occluded position.

Microstructural characterization was performed to identify the presence of carbon inclusions due to the electride formation technique and the degree of consolidation; Consolidated samples were fractured to provide a defect rich and sample post-processing independent microstructure for characterization. Characterization of the microstructure was performed via SEM on either a Zeiss EVO MA15 or a Zeiss Auriga 40 scanning electron microscope using a backscattered detector. Electron dispersive spectroscopy (EDS) was performed utilizing a Bruker XFlash 6130 detector for elemental analysis. A Quantachrome Ultrapyc 1200e was used to determine the density of the consolidated samples via He pycnometry.

Room temperature resistivity measurements are performed on pellets with >95% theoretical density that were processed for various process times and temperature. The four-point contact technique was used to accurately determine the resistance of the samples. High purity silver paste and 25 µm diameter gold wires were used for electrical contacts. A Keithley 2450 Source meter was used to inject current and sense potential drop across the sample. Low temperature resistivity measurements were performed on a Quantum Design Physical Property Measure System (PPMS) at a pressure of 4 Torr in AC mode. All the measurements were repeated twice in the same condition to confirm the reproducibility.

4.4 Results

4.4.1 Conversion of Oxy-C12A7 to Electride-C12A7

Samples processed under high vacuum in the graphite die remained white through 1200 °C with a processing time of 2 h. Laboratory XRD reveals that the C12A7 structure was retained through 1000 °C but C12A7 decomposition to C5A3 and C3A was observed at 1100 and 1200 °C. A cross section of a sample processed for an extend period of 240 h at 1200 °C reveals a clear boundary between black and white regions, inset of Figure 43. XRD characterization identified the black region located near the carbonaceous foil as C12A7 and the white core as C5A3 and C3A suggesting a diffusion of carbonaceous species into the bulk. When the processing temperature is raised above 1300 °C a bulk color change through green to black is observed for increasing process times, but when ground to a powder only samples with a processing time greater than 6 h are green while those processed for less than 2 h are white/manila. When processing time is below 2 h at 1300 °C XRD data show the main phase is C12A7 with a few wt% of the C3A and CA secondary phases suggesting non-equilibrium. After a processing time of 6 h single phase C12A7 is observed. No C5A3 was observed for any processing time at a processing temperature of 1300 °C.

SEM microstructural characterization, shown in Figure 44 on a fractured surface reveals a high concentration of carbonaceous precipitates, both large (10 µm) and small nano-sized (<1 µm) C precipitates were observed. Similar to melt grown C12A7 electrides, following the procedure of Kim et al., showing a high concentration of carbonaceous precipitates suggesting that these precipitates are characteristic of processing at high temperatures in carbonaceous environments [30].

Structural changes between the as-synthesized oxy-C12A7 and carbonaceous process formed electride-C12A7 were quantitatively analyzed using laboratory and synchrotron XRD data. As the oxy-C12A7 changes to the electride-C12A7 a relaxation of the occupied cage shape toward the unoccupied cage shape is observed due to a weaker interaction between the occluded electrons and the framework. Traditionally this averages out to a predictable increase in lattice parameter to approximately 12.01(2) Å in the fully electron injected $[\mathrm{Ca}_{24}\mathrm{Al}_{28}\mathrm{O}_{64}]^{4+}:\mathrm{e}_{(4)}^{-}$ [1,68,82]. An increase in lattice parameter is observed at 1300 °C for increasing process durations. The increase in lattice parameter slows as process duration increases approaching an asymptotic value of approximately 11.9930(6) Å as shown in Figure 45A. The system is heavily disordered due to the local changes in cage shape with interactions between the framework and the occluded species. This leads to split positions of most atomic positions, most notably the Ca cations, due to the difference in shape of occupied cages, their nearest neighbor cages, and unoccupied cages [46]. With the resolution available in laboratory powder diffraction the split positions are difficult to resolve. All structural refinements use a modified Boysen structure with only a single split Ca (Ca1a) position [2,33,163]. The actual split cation atomic positions of O^{2-}, OH^{-}, and

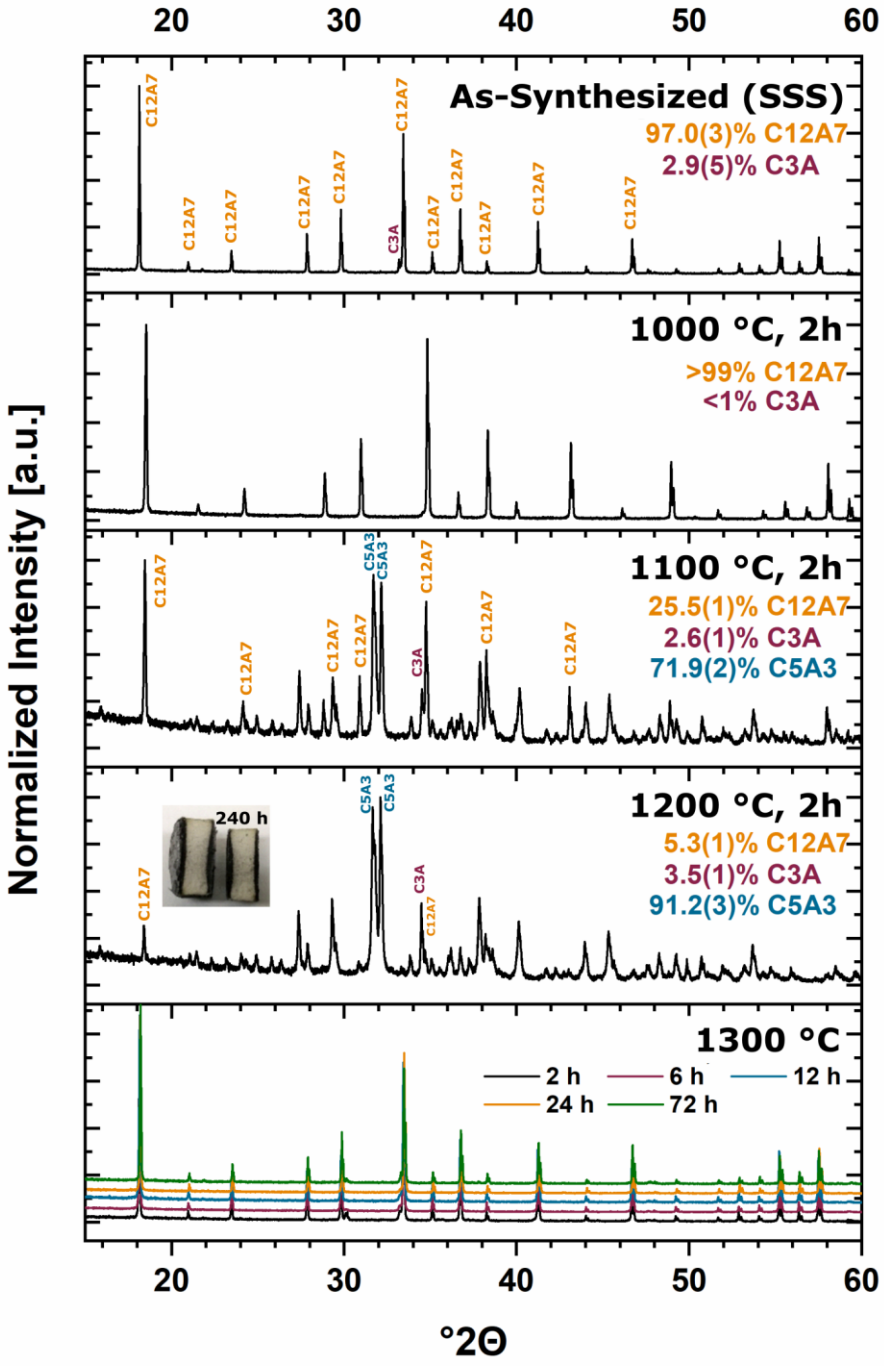

Figure 43 XRD data plotted as a function of process temperature and at 1300 °C as a function of time. Refined phase fractions are inset on the XRD patterns. Main C12A7 and secondary phase peaks are identified.

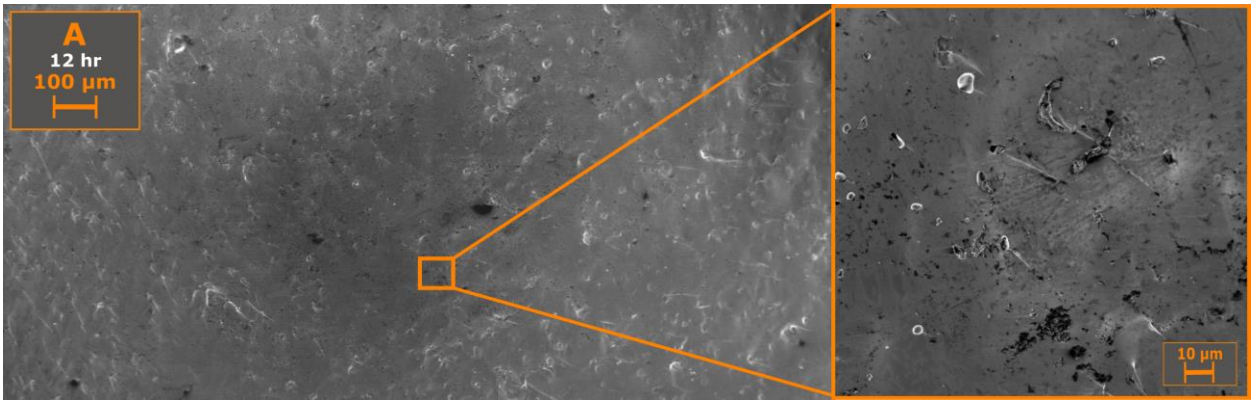

Figure 44 SEM backscattered micrograph on a fractured surface showing low porosity as well as the presence of carbon nodule impurities.

e^- occupied cages have been characterized by Palacios et al. and Sakakura et al. through structural analysis of single crystals [46,47]. Structural characterization through Rietveld refinement identifies a decrease in occupancy of the Ca1a position as process time at 1300 °C is decreased leading to an increase in the occupancy of the Ca1 position; This indicates an increase in the number of unoccupied cages and decrease in the number of anion occupied cages. Occupancy of the Ca1 position, associated with an unoccupied cage, increases to an asymptotic value correlated to the occupancy of a single cage per unit cell from an original occupancy correlated to 3 occupied cages, Figure 45. This suggests a mixed O^{2-} and OH^- occupied cage structure.

The system is heavily disordered due to the local changes in cage shape with interactions between the framework and the occluded species. This leads to split positions of most atomic positions, most notably the Ca cations, due to the difference in shape of occupied cages, their nearest neighbor cages, and unoccupied cages [46]. With the resolution available in laboratory powder diffraction the split positions are difficult to resolve. All structural refinements use a modified Boysen structure with only a single split Ca (Ca1a) position [2,33,163]. The actual split cation atomic positions of O^{2-}, OH^-, and e^- occupied cages have been characterized by Palacios et al. and Sakakura et al. through structural analysis of single crystals [46,47]. Structural characterization through Rietveld refinement identifies a decrease in occupancy of the Ca1a position as process time at 1300 °C is decreased leading to an increase in the occupancy of the Ca1 position; This indicates an increase in the number of unoccupied cages and decrease in the number of anion occupied cages. Occupancy of the Ca1 position, associated with an unoccupied cage, increases to an asymptotic value correlated to the occupancy of a single cage per unit cell from an original occupancy correlated to 3 occupied cages, Figure 45B. This suggests a mixed O^{2-} and OH^- occupied cage structure.

This change in the atomic positions and occupancy provides insight into the effect the occluded anion has on the cage. Fourier difference maps generated without

an occluded position in the structural model can be used to qualitatively assess the sites of occluded anions, which changes based on anionic type, as well as give an idea for the overall scattering density of those sites. In the as-synthesized powder the occluded position shows a high circular density at the center of the cage (0.375, 0, 0.25) as well two smaller areas of density on each side, (0.335, 0.04, 0.25) and (0.35 0.07, 0.25) corresponding to OH^-, O_2^{2-}, and O^-species, Figure 46. After processing at 1300 °C for 6 h the intensity is drastically reduced and in addition to a small amount of density in the center (0.375, 0, 0.25) equally intense positions are observed on an angle to either side whose maxima lie slightly out of the present plane at the coordinates (0.33779, 0.04639, 0.24038) and (0.33779, -0.04637, 0.25962). The distance between the center atom and the off-center maxima are approximately 0.7 Å.

In processes in which complete conversion to the electride is observed the initial wideband gap insulator transitions through a semi-conducting state ultimately to a metallic temperature invariant conductivity state as the conversion process proceeds. Characterization of the magnitude of conductivity and the proportionality of conductivity as a function of temperature indicates what degree of reduction has been achieved; semi-conducting variable range hopping is an activated process resulting in a change in conductivity as a function of temperature, while metallic type band conductivity is relatively temperature invariant. Physical property measurements show an increase in conductivity with process duration ultimately approaching an asymptotic value of approximately 15 S•cm-1,Figure 47. The temperature dependence of conductivity in the 72 h sample (Figure 9 inset) shows a decrease in conductivity with decreasing temperature indicating a temperature activated conductivity mode consistent with variable range hopping semi-conducting behavior; metallic conductivity is not achieved as process duration is increased as observed in metal reduction processes.

A subsequent experiment was performed by processing samples at 1200 °C for 2 h before raising the temperature to 1300 °C for 2 h. The intent was to decompose the C12A7 framework completely to C5A3 and C3A and then raise the temperature and analyze the crystalline product. XRD characterization of the processed sample shows single phase C12A7, compared to a multi-phase (C12A7 + C3A + CA) sample when processed directly at 1300 °C for 2 h. Further, the lattice parameter of 11.9912(2) is larger than the lattice parameter, 11.9889(3), of the sample which was processed directly at 1300 °C for 2 h. Electrical conductivity was measured to be 4.0(1) S•cm^{-1} at room temperature which is two orders of magnitude larger than the sample processed at 1300 °C for 2 hours. The lattice parameter and electrical conductivity are near the same values of the sample that was processed directly at 1300 °C for 6 h.

To assess the effect of intimate contact with the carbon source a C12A7 pellet was pressed and then placed between two alumina plates. Samples were then processed at 1200 and 1300 °C in the high vacuum furnace for 2 and 6 h, respectively. Comparison between these samples and those processed in the carbon die for equivalent process durations demonstrate a clear change in C12A7 phase content, Figure 48. At 1200 °C five times as much C12A7 is observed when processed on Al2O3

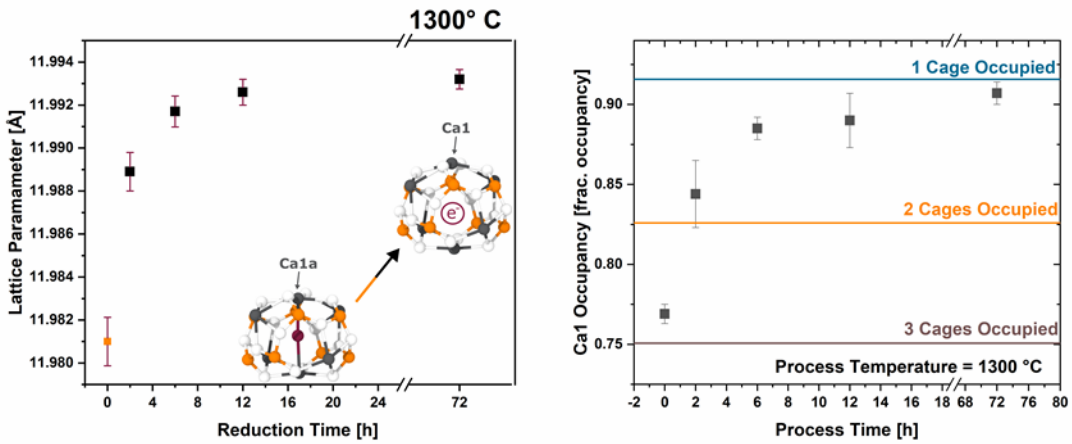

Figure 45 A) Refined lattice parameter of C12A7 reduced at 1300 °C for various process duration times. The lattice parameter continues to increase as processing time is increased. Inset shows how contracted occupied cages expand and the cage dimension increases when cages lose their occluded molecular species resulting in an increased lattice parameter. Error bars are reported as 3σ. B) Refined Ca1 (unoccupied cage) site occupation. Error bars are reported as σ.

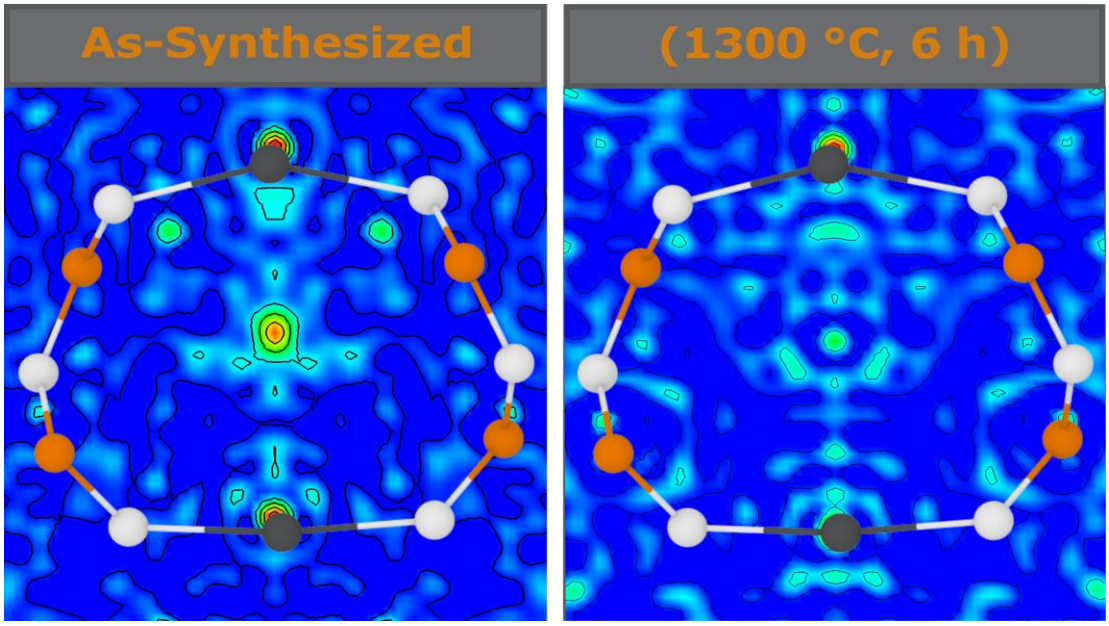

Figure 46 Fourier difference maps of the xy plane at z = ¼, slicing through the middle of a cage, generated from the synchrotron diffraction data. Brighter colors indicate an increase in scattering density with both Fourier maps having the same arbitrary scale. A comparison of as-synthesized (a) and after processing for 6 h at 1300 °C (b). The contour lines are of consistent separation across samples.

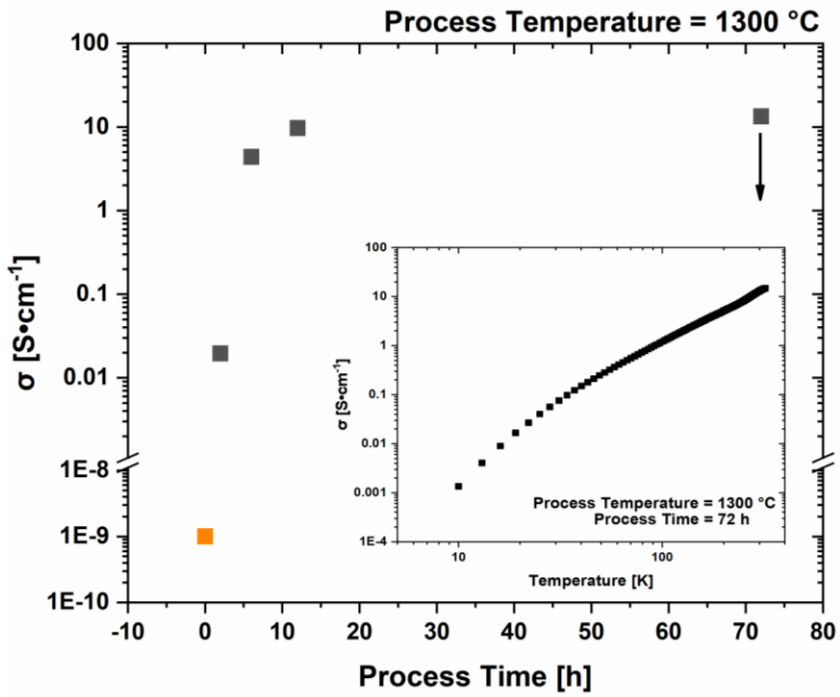

Figure 47 Electrical conductivity of samples processed at 1300 °C for various durations. The conductivity converges to a value of 15 S•cm^{-1}. The inset shows the temperature dependence of the sample which was reduced for 72 h indicating the sample was semi-conducting.

compared to samples processed on carbon. At 1300 °C, on carbon, C12A7 phase purity was observed, however, when processed on Al2O3 only 1 wt.% of C12A7 is observed; the decomposition products of C5A3 and C3A are observed. The observed lattice parameter of the sample processed on Al2O3 is that of the oxy-C12A7 structure indicating its presence is only due to the lack of full decomposition after 6 h.

4.4.2 Direct Electride Synthesis

When the starting powder is changed from oxy-C12A7 to solid state synthesis (low homogeneity) or sol-gel formed (high homogeneity), reactants formation and stability of the electride-C12A7 structure is observed once process temperature increases to 1300 °C regardless of starting reactants, Figure 49. For SSS reactants as the temperature is raised to 1000 °C $CaCO_3$ decomposition is observed. C12A7 does not form, however, the off C12A7 stoichiometry Ca rich C3A phase and Al rich CA secondary phases are observed. C3A and CA phase fractions increase as the process temperature is raised and at 1300 °C C12A7 phase formation is observed. As the process time is increased at 1300 °C the observed C12A7 content increases to 88 wt.%

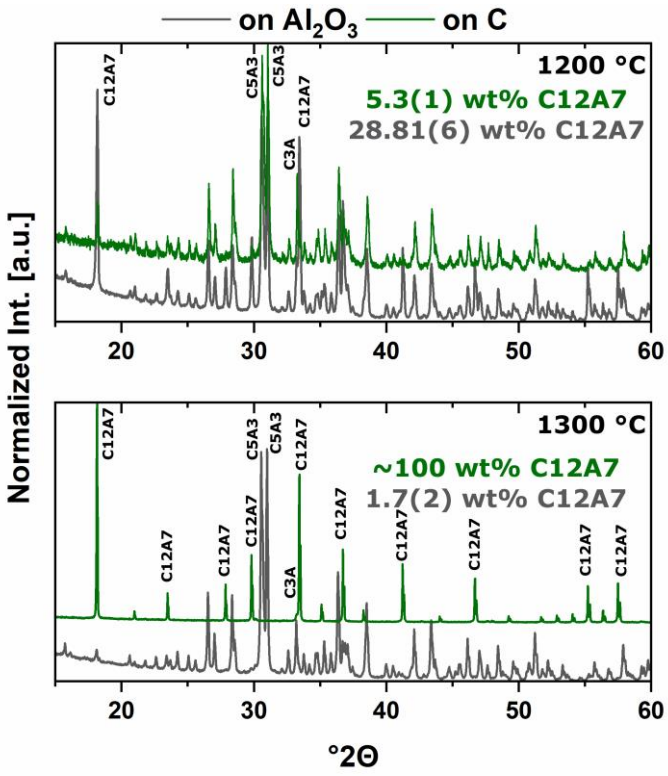

Figure 48 Comparison between as-synthesized C12A7 processed on Al2O3 (gray) vs carbon (green). The C5A3 and C3A decomposition pathway was observed in both scenarios.

after 12 h with C3A and CA making up the remaining 12 wt. %. The surface and bulk color of the consolidated sample remains white through 1300 °C for a processing time of 0 h; a process time of 0 h indicates a fast cooling once the process temperature is achieved. A gray and black color is observed as process time is increased from 2 h to above 6 h, respectively. When ground to a powder the observed color is white through processing at 1300 °C for 2 h after which the color turns to a dark green for longer processing times indicating electride formation.

The phase evolution of the PVA precursor has a different path than the SSS reactants resembling the process observed when reducing converting oxy-C12A7 to electride-C12A7, Figure 49. An amorphous product is observed through 900 °C with the observed peak being characteristic of residual carbon impurities on the surface of the sample. At 1000 °C, only ~0.25 h after the 900 °C sample due to the fast ramp rate, a white powder is characterized with C12A7 as the majority phase indicating rapid phase formation kinetics for C12A7. As the process temperature is raised above 1050 °C, the decomposition of the C12A7 phase to C5A3 and C3A is observed. At 1300 °C formation and stability of C12A7 is observed and C12A7 phase purity is found after processing for

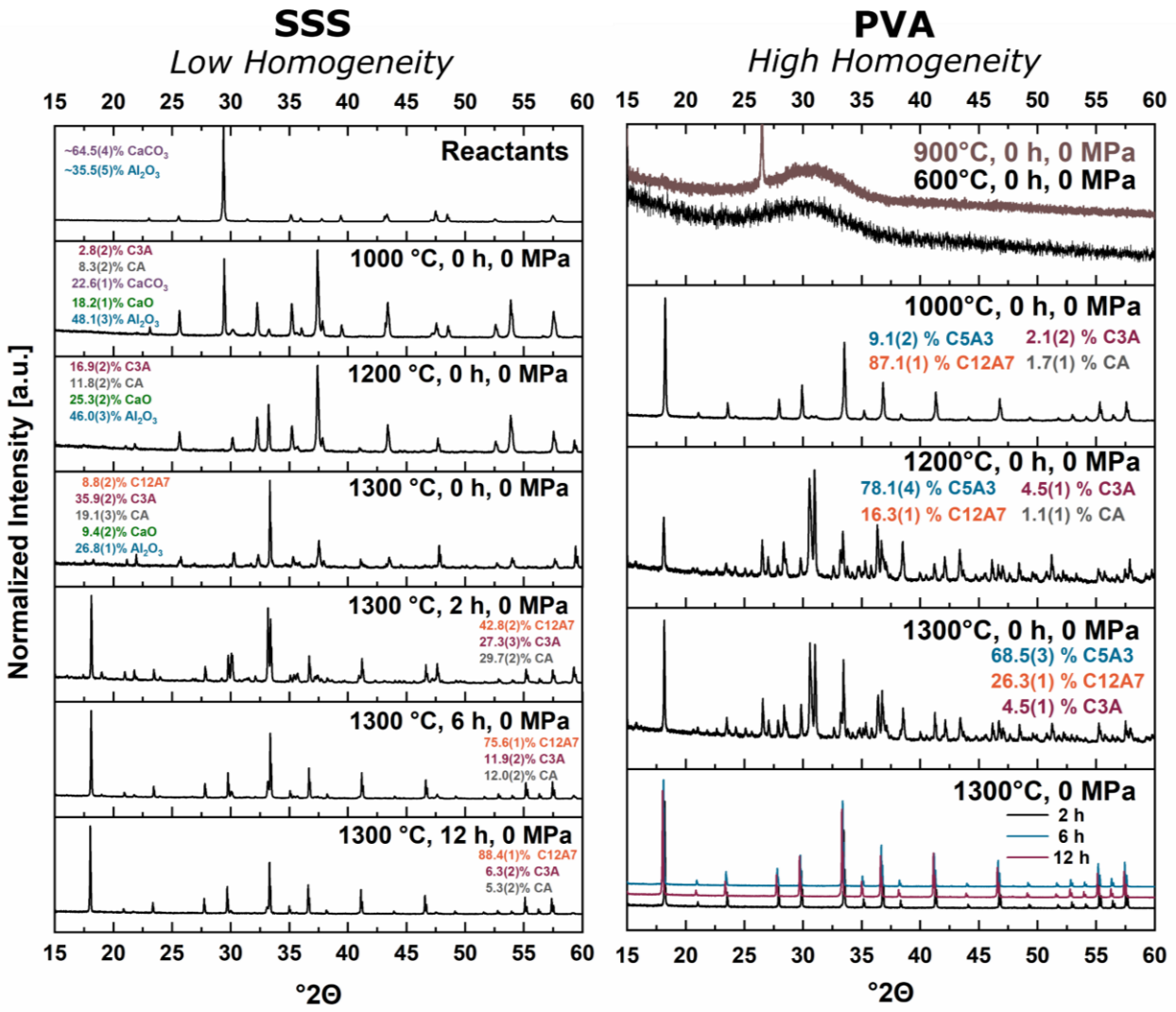

Figure 49 [Left] Kinetic phase evolution behavior of the SSS reactants with processing temperatures of 1000, 1200, and 1300 °C and a 0 h processing time and for processing times of 2, 6, and 12 h for samples with a processing temperature of 1300 °C. [Right] Kinetic phase evolution of calcined PVA precursor with processing temperatures of 600, 900, 1000, 1200, and 1300 °C and a processing time of 0 h and for processing times of 2, 6, and 12 h for samples with a processing temperature of 1300 °C.

2 h at 1300 °C. Phase purity is likely to be reached earlier based on the quick kinetics observed during decomposition and formation characterized at lower temperatures. Sample color remains white through 1300 °C for a processing time of 0 h, however, as the processing time is increased the sample color changes to black. When the consolidated samples are ground a white powder is observed through 1300 °C for a processing time of 2 h after which a change to green is observed as process time increases.

Rietveld refinements were performed to quantitatively analyze the structural changes during the electride formation process. Analysis as a function of process temperature and time shows the initial room temperature lattice parameters of C12A7, crystalized in both processes at 1300 °C, to be close to 11.993 with a relatively small increase as process time is increased, Table 12.

Table 12 Comparison of C12A7 lattice parameter after undergoing processing with a carbonaceous die in a vacuum furnace from a variety of starting points; Previously synthesized oxy-C12A7, high heterogenous solid state reactant mixture, and atomic homogenous calcined PVA sol-gel reactant mixture are the various starting points. Errors are represented as 3σ.

Temp. [°C]	Time [h]	Solid State Reaction		Wet-Chemistry
		Synth. C12A7	SSS Reactants (Al_2O_3 + $CaCO_3$)	Amorphous PVA Precursor (Calcined 600 °C)
As-Synth.	**-**	11.9808(2)	-	-
1000	**-**	11.9849(2)	-	11.9936(3)
1300	**0**	-	11.992(1)	11.9920(3)
	2	11.9889(2)	11.9923(3)	11.9918(3)
	6	11.9915(2)	11.9933(2)	11.9925(3)
	12	11.9924(1)	11.9937(3)	11.9928(2)
	72	11.9933(2)	-	-

Resistivity measurements demonstrate that the structure and color observation is correlated to a change in electrical conductivity and that direct synthesis of the electride-C12A7 from common reactant mixtures is observed. Directly synthesized pure C12A7 electrides from the PVA reactant reach a conductivity value of 3 and 5 $S \cdot cm^{-1}$ after 6 and 12 h, respectively. The sample processed at 1300 °C for 2 h was resistive with a conductivity of 4.0×10^{-3} $S \cdot cm^{-1}$. Samples synthesized from SSS reactants only achieve a high C12A7 phase purity after long process duration and the conductivity value after processing for 12 h at 1300 °C is 16 $S \cdot cm^{-1}$.

4.5 Discussion

The electride-C12A7 phase was achieved through conversion of oxy-C12A7 and through direct synthesis from heterogenous SSS and homogeneous sol-gel reactants. The degree of electron concentration agrees well with other reports and the structural evolution as a function of process time and temperature elucidate three key points for discussion; what is responsible for the change in phase equilibria at 1300 °C leading to C12A7 phase stability, what is the mechanism for electride formation, and what leads to the plateau in the degree of reduction?

4.5.1 High Temperature C12A7 Stability

The thermodynamic phase equilibria changes as a function of process temperature and time. The as-synthesized oxy-C12A7 starting phase is stable up to 1000 °C followed by instability and decomposition as process temperature is raised to 1200 °C. This decomposition is well documented in the C12A7 literature and coupled to the instability of the 'free' occluded O^{2-} anion and activation of Ca diffusion above 1050 °C leading to a change in thermodynamic equilibria [10]. This thermodynamic equilibrium is also observed from reactant mixtures. For solid state reactants no C12A7 formation is observed as the temperature is raised to 1200 °C with C3A and CA being favorable. Sol-gel reactants lead to C12A7 formation at low temperatures (≤1000 °C) due to kinetic favorability, but at higher temperature C12A7 decomposition is observed and C5A3 becomes the thermodynamic favorable phases. A shift in phase equilibria comes when the process temperature is increased to 1300 °C. C12A7 phase purity is observed as processing time is increased regardless of the starting point.

During the furnace ramp the decomposition of previously synthesized oxy-C12A7 to C5A3 and C3A does not occur instantaneously and as the temperature is rapidly increased to 1300 °C, at a ramp rate of 480 °C/h, full decomposition will not occur before 1300 °C. Once at 1300 °C the oxy-C12A7 structure is mostly retained but actively decomposing. The secondary phases of C3A and CA are observed, indicating a change in the decomposition kinetics brought on by higher cationic diffusion, but after 6 h C12A7 phase purity is achieved correlated with approaching the asymptotic values of conductivity, lattice parameter, and occupied cages. This suggests that a decomposition of oxy-C12A7 and reformation back to C12A7 is fundamental to achieving the electride phase.

This reformation process is corroborated for the oxy-C12A7 conversion process through a multi-step processing experiment. The sample is initially fired isothermally at 1200 °C for 2 h before increasing the process temperature to 1300 °C for 2 h. Full decomposition to C5A3 will occur at the lower temperature and the presence of the C12A7 structure at the higher temperature corroborates the recrystallization process. The atomic structure lattice parameter and sample conductivity are greater than that when directly processing at 1300 °C for 2 h, but slightly less than that of a sample processed at 1300 °C for 6 h. This suggests that the rate of approaching the asymptotic

atomic and electron structure is not dependent on the time spent at 1300 °C, but on the total time spent at a temperature where decomposition can occur and the degree of off stoichiometry from C12A7 of the decomposed products; the more off stoichiometric the intermediary calcium aluminate phases the more diffusion is necessary to form C12A7.

The exact transformation dynamics are obscured by the presence of oxy-C12A7 and the approach to the asymptotic values could be related to an average of the oxy-C12A7 and the newly formed electride-C12A7 phase. The direct synthesis of electride-C12A7 from reactant mixtures is not obscured by the presence of previously synthesized oxy-C12A7. The fact that there is no approach to the asymptotic values suggests that the electride forms from a direction crystallization process. Structural characterization shows that the asymptotic structural values observed in the conversion of oxy-C12A7 to electride-C12A7 are the intrinsic starting values of the electride-C12A7 formed through the direct synthesis process. These structural observations lead to the question of “What thermodynamic change or activated kinetic process leads to this change in equilibria?” Oxy-C12A7, full electride-C12A7, or a mixed oxy/electride-C12A7 structure would all be unstable under these experimental conditions (>1050 °C in a dry reducing atmosphere) indicating that a high temperature stable anionic species must be aiding in phase stability [10,48,73].

As the processing temperature is raised from 1200 to 1300 °C, the formation and stability of C12A7 is observed from all three starting points. The rise in temperature is correlated to a visible color change of samples from the as-synthesized white to a black, however, when the consolidated samples are ground the powder color is dark green; The ultimate conductivity achieved is too low for the change to black to be correlated to an increase in free Drude carriers indicating that the change to black results for another reason. This observation coupled with the observance of C in the microstructure indicates the increase in system energy activates the diffusion of C whose availability as an anionic species leads to high temperature C12A7 stability; the diffusion of C into hot-pressed materials is well documented with the carbonaceous source of the die [164,165].

To evaluate this theory the carbon source was removed and replaced with alumina and no observed stabilization occurs; Phase equilibria consists of C5A3 and C3A at 1300 °C. At 1200 °C the kinetics of decomposition to C5A3 and C3A are sluggish compared to when the sample is directly in contact with C indicating that the presence of sample-die interfacial carbon plays a role in the instability of the oxygen anion. This correlates well to the observation that decomposition increases with a shift toward more reducing environments from a dry oxidizing, to vacuum, ultimately to a carbonaceous vacuum environment [10,83]. The activation of carbon diffusion and phase equilibria achieved when removing the carbon source clearly indicates that a solid-state interaction of C leads to the C12A7 phase.

The structural observations from this solid state experimentation match well with the equilibria theory proposed in characterizing electride-C12A7 synthesized from high temperature melts [30]**.** No inference can be made on the species of carbon, but in the

solid state process the diffusion of carbide species in C12A7 is unlikely. The cages may act like nano-reactors forming the carbide anion, but diffusional processes likely require the disassociation and interstitial diffusion of individual carbon species. This is a similar process to that proposed for hydroxide diffusion [7].

4.5.2 Electride Formation Mechanism

The structural investigation provides strong experimental evidence for the necessity of C for high temperature C12A7 crystallization, but the mechanism behind electride conversion and the asymptotic behavior in electride conversion are still difficult to elucidate with a high degree of confidence. The theory for electride conversion put forth from melt formed electride-C12A7 is that the C_2^{2-}anion is responsible for C12A7 crystallization and anion instability is observed during cooling or instantaneously after nucleating the cages [30]. In this study anion instability would require a diffusionless phase transformation as the temperature is quickly quenched to below 600 °C; This is further limited due to the slow dissociative diffusion process proposed for carbon diffusion. Instantaneous instability after nucleating the cages does not explain the retained phase stability of electride-C12A7 for extended time durations in a thermodynamic regime where decomposition would occur. The electron is not capable of sustaining the C12A7 framework and decomposition is observed in non-carbonaceous environments [48,73]. The second consideration is the electride conversion process does not continue to full electron concentration, resulting in semi-conducting behavior reported in other carbonaceous reduction studies [31,60,158]. The aforementioned model does not accurately characterize the structural behavior reported here and another model is needed to characterize the electride formation observed in this report.

An alternative model proposed by Jiang et al. assumes that carbide anion diffusion into the C12A7 particles will not occur and that the reduction process occurs through the interfacial reaction of occluded O and microstructural carbon. Two issues that remain unresolved by this model are (1) the formation of oxy-C12A7 at higher temperature, where it is thermodynamically unstable and (2) the long duration of phase stability under conditions where neither oxy-C12A7 nor electride-C12A7 are thermodynamically favored.

We propose a new theory which builds upon the two current theories where C12A7 formation occurs with mixed C and O occluded anions and the electride conversion occurs through interaction of these occluded species and interfacial carbon species. Previously, the theory that carbide was responsible for the crystallization of C12A7 from a high temperature melt assumed no other templating anions besides C are available. A reasonable assumption in the sense that even if there was excess oxygen in the melt it is not thermodynamically favorable to form oxy-C12A7, but in the solid-state system extra-framework oxygen is accounted for in the chemical equilibria. The main formation pathways observed for C12A7 formation occur through the interaction of off stoichiometry calcium aluminate phases:

$$5\ Ca_3Al_2O_6\ (C3A) + 9\ CaAl_2O_4(CA) \leftrightarrow 2\ [Ca_{12}Al_{14}O_{32}]^{2+}:O^{2-}(C12A7)$$

$$Ca_3Al_2O_6(C3A) + 9\ Ca_5Al_6O_{14}(C5A3) \leftrightarrow 4\ [Ca_{12}Al_{14}O_{32}]^{2+}:O^{2-}(C12A7)$$

$$12\ CaO(C) + 7\ Al_2O_3(A) \leftrightarrow [Ca_{12}Al_{14}O_{32}]^{2+}:O^{2-}(C12A7)$$

If stoichiometrically balanced utilizing the framework stoichiometry ($Ca_{12}Al_{14}O_{32}$) an excess of oxygen is needed. Support of this theory is observed during the direct synthesis of the homogeneous sol-gel reactants where C12A7 formation occurs between 900-1000 °C where carbon diffusion has yet to be activated and the energy for oxy-C12A7 thermodynamic instability has yet to be reached; the only available anion for C12A7 formation is oxygen contained within the reactants. The presence of oxygen in the second theory by Jiang is plausible with a realized oxygen source and interfacial reduction can occur, however, the stability of the oxy/electride-C12A7 structure is not explained if we assume a single anion model.

It was previously assumed that carbide diffusion into the C12A7 particle is unlikely, but the diffusion of mono-atomic carbon species is likely. Structural analysis shows that the cage “windows” are 3.7 Å in diameter and carbon diffusion is readily observed interstitially in Fe where nearest neighbor bond distances are <3 Å [28,166]. The idea of mixed anion stability is observed elsewhere in the C12A7 phase space. Under humid conditions a mixture of oxygen and hydroxide occupied cages leads to phase stability above 1050 °C where oxy-C12A7 instability is observed under dry conditions [10]. With the presence of oxygen and carbon species phase stability is understood and there is a clear electride formation process. The negative enthalpy of formation for the reaction of oxygen and C drives the formation of anion vacancies and electron injections; This may occur through the interaction of occluded species as well as interfacial species as proposed by Jiang et al. [160].

4.5.3 Plateau in Electride Formation

The final point for consideration is the driving factor behind the ultimate level of reduction only reaching a semi-conducting state rather than the metallic type conductivity state achieved with other techniques. The driving factor behind electride conversion is thermodynamic equilibria and the presence of a negative enthalpy chemical reaction. In order to reach this thermodynamic equilibria, the diffusion of occluded anions from the C12A7 phase to the oxygen getter needs to occur resulting in anionic vacancies. The plateau in conductivity is either limited by the intrinsic reduction process, the kinetic diffusion of anionic species, or the thermodynamic driving factor. An example of the intrinsic reduction process limiting electron concentration is observed in the hydrogen gas reduction process [78]. However, the same equilibrium observed in this study is observed when treating oxy-C12A7 in a CO^- reducing atmosphere; in this case there are no carbon species occupying the cage and only O^{2-} suggesting that another limiting factor should be considered [60].

The Ca metal reduction method only achieves moderate conductivity (~100 $S \cdot cm^{-1}$) due to the blockage of the kinetic pathway responsible for anionic vacancy

injection [43]. In the mixed oxygen and carbon occluded anion C12A7 high oxygen mobility toward the occluded carbon species would be observed. The formation of CO would take place inside of the cage, similar to the hydration of C12A7 and hydroxide diffusion, and once the new polyatomic anion has formed its diffusion and mobility will be dramatically hindered relative to monoatomic species; A diffusion method similar to OH^- diffusion may occur with the dissociation of CO, interstitial diffusion of C, and then recombination in the adjacent cages [7]. The large diatomic anion will act as a blocking agent for future oxygen, carbon, and electron diffusion limiting further formation of anion vacancies and limiting mobility of localized carriers. There is a significant difference between the blocked kinetic pathways in the Ca metal reduction method versus this method. In the former the kinetic pathway blockage is due to a layer of CaO encasing the material where this discussion suggests a blocking of diffusion pathways by molecules within the cages. This is unlikely due to the high interconnectivity of the cages where each cage has 12 nearest neighbor cages. Application of a percolation theory, Equation 14 and Equation 15, of a system with 12 neighbor connectivity demonstrates that while diffusion would decrease with an increase in the number of occupied cages it would not cease completely until 10 cages are occupied, Figure 50 [167].

Equation 14 $$\frac{D_m}{D_0} = \frac{1}{2}\left\{A + \left[A^2 + \frac{4f}{\left(\left(\frac{z}{2}\right)-1\right)}\right]^{\frac{1}{2}}\right\}$$

Equation 15 $$A = 1 - p + fp - \frac{f+p-fp}{\left(\frac{z}{2}-1\right)}$$

$\frac{D_m}{D_0}$ is the normalized average diffusivity, p is the fraction of blocked cages, *f* is the diffusivity through blocked pathways which was set to zero, and *z* is the average coordination number to nearest neighbor diffusion sites, 12 in this case [167]. The Fourier difference maps demonstrate a decrease in occluded position electron density corresponding to cage occupancy making the equilibria observed unlikely due to a blocking of diffusion kinetic pathways in the cage structure. Therefore, another process should be considered.

The reduction of C12A7, in all techniques, is driven by the negative enthalpy of oxidation of an external chemical species. Oxidation of Ca and Ti have large negative enthalpies of formation, -635 and -940 kJ/mol, respectively [168,169]. The enthalpy of formation for CO and CO_2 is relatively lower at -110.53 and -393.52 kJ/mol, respectively [168]. While C12A7 is an oxidizing agent with oxygen in the cage, the full electride has a positive enthalpy of formation, indicating that the full oxygen occupation is thermodynamically preferred and oxidation of the fully converted electride has an enthalpy of formation between -425 and -600 kJ/mol [60,170]. This makes the electride a reducing agent (the ability for C12A7 to be both an oxidizing and a reducing agent as a function of processing is part of what leads to the observed high functionality.)

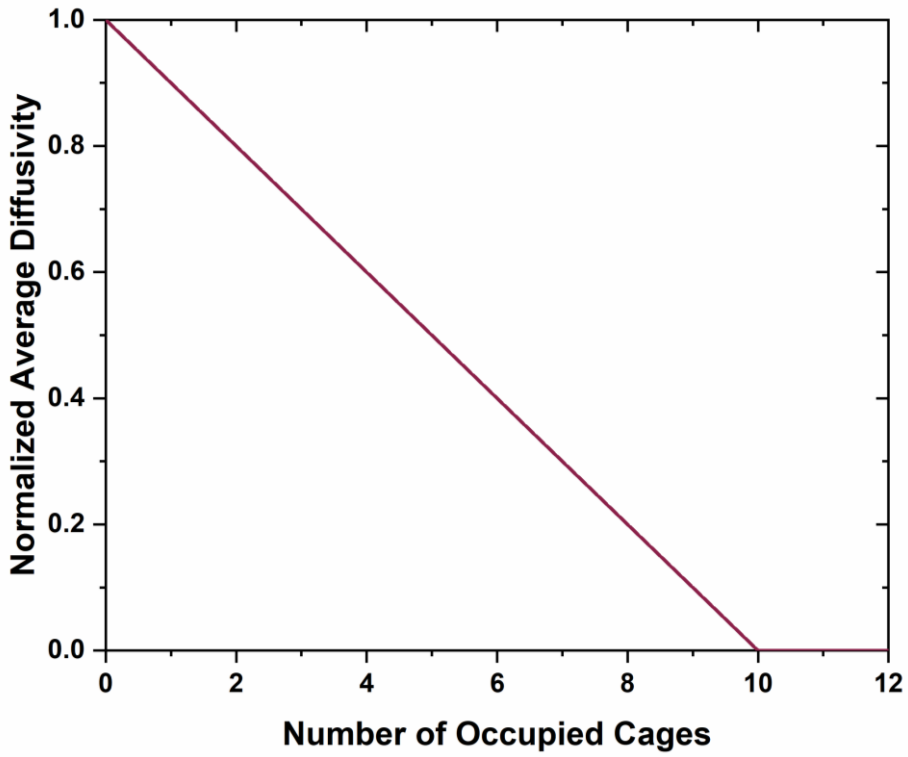

Figure 50 Normalized calculated average diffusivity as a function of the number of occupied cages. A linear decrease is observed as the occupation of diffusional sites increases leading to a diffusion of zero once 83 % of the cages are occupied.

Figure 51 compares the enthalpy of oxidation as a function of electride conversion with the enthalpy of oxidation for C, Ca, and Ti super imposed; The enthalpy of oxidation for electride-C12A7 decreases as the degree of electron concentration decreases and the slope of this line is -580 kJ/mol [170]. This representation assumes that these values are comparable at elevated temperatures, that the enthalpy of formation from elemental species is a good approximation for that observed in the complex C12A7 system, and that the linear decrease in enthalpy as a function of electron concentration is valid under the carbonaceous vacuum conditions. TiO_2 and CaO have enthalpies of formation with magnitudes higher than that of the full electride indicating that oxidation of these cations

The reduction of C12A7, in all techniques, is driven by the negative enthalpy of oxidation of an external chemical species. Oxidation of Ca and Ti have large negative enthalpies of formation, -635 and -940 kJ/mol, respectively [168,169]. The enthalpy of formation for CO and CO_2 is relatively lower at -110.53 and -393.52 kJ/mol, respectively [168]. While C12A7 is an oxidizing agent with oxygen in the cage, the full electride has a positive enthalpy of formation, indicating that the full oxygen occupation is thermodynamically preferred and oxidation of the fully converted electride has an enthalpy of formation between -425 and -600 kJ/mol [60,170]. This makes the electride a

reducing agent (the ability for C12A7 to be both an oxidizing and a reducing agent as a function of processing is part of what leads to the observed high functionality.) Figure 51 compares the enthalpy of oxidation as a function of electride conversion with the enthalpy of oxidation for C, Ca, and Ti super imposed; The enthalpy of oxidation for electride-C12A7 decreases as the degree of electron concentration decreases and the slope of this line is -580 kJ/mol [170]. This representation assumes that these values are comparable at elevated temperatures, that the enthalpy of formation from elemental species is a good approximation for that observed in the complex C12A7 system, and that the linear decrease in enthalpy as a function of electron concentration is valid under the carbonaceous vacuum conditions. TiO_2 and CaO have enthalpies of formation with magnitudes higher than that of the full electride indicating that oxidation of these cations will occur in favor of oxidation of the electride-C12A7 with the highest possible electron occupation. However, for the oxidation of C both the oxidation to CO_2 and CO have lower enthalpies of formation with magnitudes less than that of the full electride. This makes the formed electride-C12A7 a competing reduction agent and equilibrium will occur where the enthalpy of oxidation of electride-C12A7 is equal to the enthalpy of oxidation for C. At this point the electride conversion process will cease and an equilibrium will be observed irrespective of further processing. Based on our structural observations this coincides with one cage occupied and an electrical conductivity of ~15 $S \cdot cm^{-1}$; the exact ratio of O:C species and valence of these remaining species is unable to be determined in this study. The presence of the remaining C species leads to the high temperature stability at the electride-conversion equilibrium.

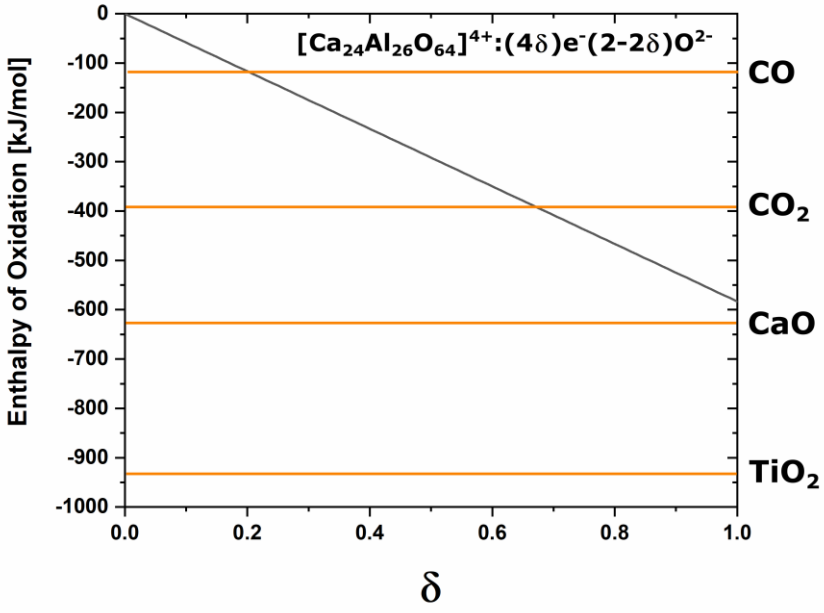

Figure 51 Enthalpy of oxidation of C12A7 as a function of electron conversion (δ) compared to the enthalpies of oxidation of C, Ca, and Ti [60,168–170].

This model is supported by the observed structural characterization. However, future work is needed to fully identify the type and presence of occluded C species. Such a task is challenging due to the occluded position disorder, low occupation, and low Z of anions of interest. The kinetic processes during reduction involve changes in local short-range order while retaining the long-range order of the framework. In-situ diffraction techniques as a function of temperature, atmosphere, and time, probing both local and long-range order, could provide the experimental verification of the proposed reduction methods with higher resolution than the limited process data points able to be analyzed in ex-situ techniques. Atomistic modelling can be employed utilizing reactive force field potentials to determine thermodynamic properties and confirm the nano-reactor theory responsible for electride C12A7 formation.

4.6 Conclusion

Successful electride-C12A7 formation was observed in a high vacuum carbonaceous environment not only from the conversion of pre-synthesized oxy-C12A7, but also the direct synthesis through heterogenous solid state and homogeneous non-carbonaceous polymer assisted sol-gel reactants. This is the first report of direct electride formation from $CaCO_3$ + Al_2O_3 and a non-carbonaceous sol-gel reactant.

1) Direct contact with a carbon source, at 1300 °C to activate carbon diffusion, and decomposition of the oxy-C12A7 phase, is suggested for the reformation to a new thermodynamically favorable phase in a dry reducing condition. The presence of other calcium aluminates compounds preserves the oxygen availability needed to form oxygen occupied C12A7 and the incorporation of C as an occluded anion leads to a mixed occupancy high temperature phase stability much like the incorporation of OH^- does in high temperature humid environments.
2) The reduction method is proposed to be an interaction between the occluded C and O anions as well as interfacial C and O with an observed plateau in atomic structural parameters and electronic conductivity regardless of extended processing time. This represents a new electride formation model.
3) The most plausible theory for the plateau in electrical conductivity involves the competing thermodynamics of oxidation where the reducing power of the electride-C12A7 phase and the C species become equal in strength.

Further experimentation combining in-situ and total scattering diffraction as well as atomistic modeling is necessary for further validation and clarification of anionic species ratios, reduction thermodynamic information, and short-range order in C12A7. This presents a shift in theory behind the carbonaceous C12A7 electride formation derived from a structural characterization of the electride-C12A7 formation.

CONCLUSION

The direction and culmination of this investigation is the development of direct electride synthesis. Successful direct electride synthesis was achieved from both heterogenous and homogeneous solid state and polymer assisted sol-gel reactants, respectively, at 1300 °C in a vacuum carbonaceous environment. During the path to this final success many other insights, successes, and scientific findings were acquired.

The application of the amorphous citrate method was utilized in the literature without consideration for the underlying process. This led to the synthesis of many doped compounds which may appear to be XRD pure, but it reality have the dopants segregated and not incorporated into the C12A7 structure. A first principles approach to the synthesis of Cu-C12A7 was taken to highlight the difficulties and demonstrate that consideration of the chemistry is needed for success in this technique. Theoretical complex vs. pH diagrams were calculated to ensure that gel formation consists of only metal citrate complexes; the diagrams predicted a raise in process pH from its intrinsic value of <1 to 4 was necessary for proper citrate gel formation. The adaptation of the rapid solvent extraction method was performed to control the initial stage of decomposition ensuring that combustion-based decomposition occurred systematically and not locally. These process modification lead to a decrease in synthesis temperature and time, reduction in grain size and grain growth kinetics, and avoided the formation of $CaCO_3$ during heating which resulted inhomogeneous phase formation.

The amorphous citrate method gives the desired result but requires significant consideration of reaction chemistry whenever the cationic system changes. If a researcher wishes to utilize that method the proper procedure has been derived, however, a new polymer assisted C12A7 synthesis was developed. This process combats the intrinsic limitations of the amorphous citrate process by circumventing the formation of individual metal ligand complexes to ensure homogeneous gel formation and crosslinked polymers provide steric entrapment to retain homogeneity during decomposition. The polymer assisted process utilizes a common industrial polymer, polyvinyl alcohol (PVA), and suggests decreasing the organics:cation ratio for a higher oxide yield. This results in a reduction in process cost and ecological impact. For the synthesis of Cu-C12A7 the resultant material was robust with change process variables with all samples showing >90 wt% of the desired phase. The intrinsic nature of the process allows for application to diverse cationic systems without extensive consideration to process chemistry, and the addition of ethylenediaminetetraacetic acid (EDTA) can ensure success with nearly all cationic systems. For these reasons the polymer assisted sol-gel route is the desired process to develop a homogenous reactant for direct electride synthesis and kinetic formation studies

The kinetic study of the C12A7 formation has the highest impact after the development of direct synthesis as it characterizes a process which has previously only been observed through thermodynamic techniques. Ca diffusion limits the rate of phase

formation during the kinetic transformation to C12A7, however, the pathways are generally unchanged when utilizing heterogenous solid state reactants. When atomically homogeneous reactants are use direct formation of C12A7 is observed from an amorphous reactant mixture. This identified the low temperature formation pathway to not include C5A3 or C3A. C5A3 was never observed as a reactant for C12A7 formation and the only time it was observed in the characterization was during the decomposition of C12A7 under dry or vacuum environments. When atomic homogeneity is achieved C12A7 is the predominant phase to form in ambient, dry, or vacuum environments. The vacuum environment formation represents a shift in historical thinking where a templating anion was required to be present in the atmosphere for C12A7 formation.

The structural characterization of the carbonaceous reduction process on oxy-C12A7 demonstrated that the electride conversion process requires direct contact with a carbon source, reaches a clear equilibrium conversion, and requires decomposition and recrystallization of the C12A7 phase. The decomposition of the oxy-C12A7 was observed at temperature above 1050 °C due to the change in thermodynamic equilibria characterized in the kinetic formation studies. Stability of the C12A7 structure was observed as the process temperature was raised to 1300 °C only when in direct contact with a carbon source; this stability is attributed due to the activation of solid state diffusion of carbonaceous species into the calcium aluminate bulk. This suggests a C based anion is incorporated into the clathrate structure leading to high temperature stability. This has been hypothesized before when crystallizing from a liquid state, but this is the first robust characterization from the solid state; the species of the carbon anion was attempted but was not determined from these investigations. A new model for electride formation was presented and derived from observation in the kinetic studies under a vacuum environment. The high temperature stable C12A7 structure is predicted to be a mixed O and C species stabilized structure; the presence of other calcium aluminates compounds preserves the oxygen stoichiometry need to form oxygen occupied C12A7 and the incorporation of C as an occluded anion leads to phase stability much like the incorporation of OH^-does in high temperature humid environments. It is then an interaction of these species to form CO or CO2 which drives the formation of anion vacancies and electron injection. The observed plateau in conductivity could either be due to a blocking of the kinetic pathways by CO/CO2 anions occluded in the cages or a change in the thermodynamic driving factors. The latter is more plausible; the electride C12A7 is a reducing agent and the reducing power increases as a function of electron injection with the ultimate enthalpy of oxidation being higher than the oxidation of C. Ergo the electride equilibrium observed is tied to the equilibration of these thermodynamic enthalpies of oxidation and intrinsic to the carbonaceous reduction method; metallic type conduction is not possible as observed when utilizing strong reducing agents such as Ca and Ti metal. The characterization of the carbonaceous reduction process identified the appearance of high temperature electride-C12A7 solid state formation which is the exact mechanism needed for direct electride synthesis.

The development of reactant mixtures required the use of a new synthesis procedure to create a robust doped synthesis process. The characterization of phase formation kinetics yielded insights into the mechanisms behind electride formation. Finally, the characterization of the carbonaceous reduction process revealed the direct synthesis possibility. Without the synthesis to make the reactants, the kinetic studies to observe C12A7 formation in a vacuum environment, or the characterization of the carbonaceous process the direct synthesis of the C12A7 electride would not have been a reality. With the process well defined further investigations into the synthesis of doped C12A7 can be performed and future research can focus on determining the structure property relationships of doped-C12A7 electrides.

REFERENCES

1 J. Huang, L. Valenzano and G. Sant, *Chem. Mater.*, 2015, **27**, 4731–4741.

2 H. Boysen, M. Lerch, A. Stys and A. Senyshyn, *Acta Crystallogr. Sect. B Struct. Sci.*, 2007, **B63**, 675–682.

3 S. W. Kim and H. Hosono, *Philos. Mag.*, 2012, **92**, 2596–2628.

4 P. V Sushko, A. L. Shluger, M. Hirano and H. Hosono, *J. Am. C*, 2007, **129**, 942–951.

5 G. I. Zhmoidin and A. K. Chatterjee, *Cem. Concr. Res.*, 1984, **14**, 386–396.

6 M. Teusner, R. A. De Souza, H. Krause, S. G. Ebbinghaus, B. Belghoul and M. Martin, *J. Phys. Chem. C*, 2015, **119**, 9721–9727.

7 K. Hayashi, M. Hirano and H. Hosono, *J. Phys. Chem. B*, 2005, **109**, 11900–11906.

8 R. N. Edmonds and A. J. Majumdar, *Cem. Concr. Res.*, 1988, **18**, 473–478.

9 K. Hayashi, P. V Sushko, D. M. Ramo, A. L. Shluger, S. Watauchi, I. Tanaka, S. Matsuishi, M. Hirano and H. Hosono, *J. Phys. Chem. B*, 2007, **111**, 1946–1956.

10 J. Eufinger, A. Schmidt, M. Lerch and J. Janek, *Phys. Chem. Chem. Phys.*, 2015, **17**, 6844–6857.

11 K. Hayashi, M. Hirano, S. Matsuishi and H. Hosono, *J. Am. Chem. Soc.*, 2002, **124**, 738–739.

12 K. Hayashi, M. Hirano, Q.-X. Li, M. Nishioka, M. Sadakata, Y. Torimoto, S. Matsuishi and H. Hosono, *Electrochem. Solid-State Lett.*, 2002, **5**, J13–J16.

13 K. Hayashi, S. Matsuishi, N. Ueda, M. Hirano and H. Hosono, *Chem. Mater.*, 2003, **15**, 1851–1854.

14 K. Hayashi, N. Ueda, M. Hirano and H. Hosono, *J. Phys. Chem. B*, 2004, **108**, 8920–8925.

15 S. Yang, J. N. Kondo, K. Hayashi, M. Hirano, K. Domen and H. Hosono, *Chem. Mater.*, 2004, **16**, 104–110.

16 R. Stober, M. Nofz, W. Gesner and G. Kranz, *J. Solid State Chem.*, 1989, **81**, 152–164.

17 S. Fujita, K. Suzuki, M. Ohkawa, T. Mori, Y. Iida, M. Youhei, M. Hideki and S. Shimada, *Chem. Mater.*, 2003, **15**, 255–263.

18 K. Hayashi, M. Hirano and H. Hosono, *Chem. Lett.*, 2005, **34**, 586–587.

19 P. V. Sushko, A. L. Shluger, K. Hayashi, M. Hirano and H. Hosono, *Phys. Rev. B*, 2006, **73**, 045120.

20 K. Hayashi, M. Hirano and H. Hosono, *Bull. Chem. Soc. Jpn.*, 2007, **80**, 872–884.

21 K. Hayashi, *J. Phys. Chem. C*, 2011, **115**, 11003–11009.

22 K. Hayashi, S. Matsuishi, T. Kamiya, M. Hirano and H. Hosono, *Nature*, 2002, **419**, 462–465.

23 J. Jeevaratnam, F. P. Glasser and L. S. D. Glasser, *J. Am. Ceram. Soc.*, 1964, **47**, 105–106.

24 P. P. Williams, *Acta. Cryst.*, 1973, **B29**, 1550–1551.

25 C. Song, J. Sun, J. Li, S. Ning, M. Yamamoto, J. Tu, Y. Torimoto and Q. Li, *J. Phys. Chem. C*, 2008, **112**, 19061–19068.

26 Q. L. Feng, F. P. Glasser, R. a. Howie and E. E. Lachowski, *Acta Cryst.*, 1988, **C44**, 589–592.

27 A. Schmidt, M. Lerch, J. P. Eufinger, J. Janek, R. Dolle, H. D. Wiemhöfer, I. Tranca, M. M. Islam, T. Bredow, H. Boysen and M. Hoelzel, *Solid State Sci.*, 2014, **38**, 69–78.

28 A. Schmidt, H. Boysen, A. Senyshyn and M. Lerch, *Zeitschrift fur Krist.*, 2014, **229**, 427–434.

29 J. M. Polfus, K. Toyoura, C. H. Hervoches, M. F. Sunding, I. Tanaka and R. Haugsrud, *J. Mater. Chem*, 2012, **22**, 15828–15835.

30 S. Kim, M. Miyakawa, K. Hayashi, T. Sakai, M. Hirano and H. Hosono, *J. Am. Chem. Soc.*, 2005, **127**, 1370–1371.

31 J. H. Chung, J. H. Ryu, J. W. Eun, B. G. Choi and K. B. Shim, *Electrochem. Solid-State Lett.*, 2011, **14**, E41–E43.

32 A. M. Volodin, V. I. Zaikovskii, R. M. Kenzhin, A. F. Bedilo, I. V. Mishakov and A. A. Vedyagin, *Mater. Lett.*, 2017, **189**, 210–212.

33 H. Boysen, I. Kaiser-Bishoff and M. Lerch, *Diffus. Fundam.*, 2008, **8**, 2.1-2.8.

34 M. Miyakawa, H. Kamioka, M. Hirano, T. Kamiya, P. V. Sushko, A. L. Shluger, N. Matsunami and H. Hosono, *Phys. Rev. B*, 2006, **73**, 205108.

35 F. Bridges, G. Davies, J. Robertson and A. M. Stoneham, *J. Phys. Condens. Matter*, 1990, **2**, 2875–2928.

36 J. L. Dye, *Acc. Chem. Res.*, 2009, **42**, 1564–1572.

37 S. Matsuishi, Y. Toda, M. Miyakawa, K. Hayashi, T. Kamiya, M. Hirano, I. Tanaka and H. Hosono, *Science (80-.).*, 2003, **301**, 626–629.

38 X. Zhang, Z. Xiao, H. Lei, Y. Toda, S. Matsuishi, T. Kamiya, S. Ueda and H. Hosono, *Chem. Mater.*, 2014, **26**, 6638–6643.

39 K. Lee, S. W. Kim, Y. Toda, S. Matsuishi and H. Hosono, *Nature*, 2013, **494**, 336–341.

40 T. Inoshita, S. Jeong, N. Hamada and H. Hosono, *Phys. Rev. X*, , DOI:10.1103/PhysRevX.4.031023.

41 S. Zhao, E. Kan and Z. Li, *WIREs Comput. Mol. Sci.*, 2016, **6**, 430–440.

42 S. Liao, R. Yao, X. Chen, G. Wang and F. Zheng, *Int. J. Appl. Ceram. Technol.*, 2016, **13**, 844–855.

43 S.-W. Kim, S. Matsuishi, M. Miyakawa, K. Hayashi, M. Hirano and H. Hosono, *J. Mater. Sci. Mater Electron*, 2007, **18**, S5–S14.

44 F. Gfellar, *Highlights in Mineralogical Crystallography: Mayenite Ca12Al14O33: From Minerals to the first stable electride crystals*, Walter de Gruyter GmbH & Co KG, 2016.

45 E. Feizi and A. K. Ray, *J. Disp. Technol.*, 2016, **12**, 451–459.

46 T. Sakakura, K. Tanaka, Y. Takenaka, S. Matsuishi, H. Hosono and S. Kishimoto, *Acta Crystallogr. Sect. B Struct. Sci.*, 2011, **67**, 193–204.

47 L. Palacios, A. Cabeza, S. Bruque, S. Garcia-Granda and M. A. G. Aranda, *Inorg. Chem.*, 2008, **47**, 2661–2667.

48 L. Palacios, Á. G. De La Torre, S. Bruque, J. L. García-Muñoz, S. García-Granda, D. Sheptyakov and M. a G. Aranda, *Inorg. Chem.*, 2007, **46**, 4167–4176.

49 T. Nomura, K. Hayashi, Y. Kubota, T. Kamiya, M. Hirano, M. Takata and H. Hosono, *Chem. Lett.*, 2007, **36**, 902–903.

50 H. Boysen, I. Kaiser-Bischoff, M. Lerch, S. Berendts, A. Börger, D. M. Trots, M. Hoelzel and A. Senyshyn, *Zeitschrift fur Krist. Suppl.*, 2009, **30**, 323–328.

51 S. Matsuishi, S. W. Kim, T. Kamiya, M. Hirano and H. Hosono, *J. Phys. Chem. C*, 2008, **112**, 4753–4760.

52 K. Hayashi, H. Muramatsu, S. Matsuishi and T. Kamiya, *Curr. Appl. Phys.*, 2009, **17**, 2008–2010.

53 J. E. Medvedeva and a. J. Freeman, *Europhys. Lett.*, 2005, **69**, 1–3.

54 M. I. Bertoni, T. O. Mason, J. E. Medvedeva, Y. Wang, A. J. Freeman and K. R. Poeppelmeier, *J. Appl. Phys.*

55 R. P. S M Lobo, N. Bontemps, M. I. Bertoni, T. O. Mason, K. R. Poeppelmeier, A. J. Freeman, M. S. Park and J. E. Medvedeva, *J. Phys. Chem. C*, 2015, **119**, 8849–8856.

56 Z. Li, J. Yang, J. G. Hou and Q. Zhu, *Angew. Chemie - Int. Ed.*, 2004, **43**, 6479–6482.

57 S. W. Kim, Y. Toda, K. Hayashi, M. Hirano and H. Hosono, *Chem. Mater.*, 2006, **18**, 1938–1944.

58 S. W. Kim, S. Matsuishi, T. Nomura, Y. Kubota, M. Takata, K. Hayashi, T. Kamiya, M. Hirano and H. Hosono, *Nano Lett.*, 2007, **7**, 1138–1143.

59 S. W. Kim, M. Miyakawa, M. Hirano, Y. Kohama, H. Kawaji, T. Atake, H. Ikegami, K. Kono and H. Hosono, *Mater. Trans.*, 2008, **49**, 1748–1752.

60 S. W. Kim, K. Hayashi, M. Hirano, H. Hosono and I. Tanaka, *J. Am. Ceram. Soc.*, 2006, **89**, 3294–3298.

61 H. Hosono, S.-W. Kim, S. Matsuishi, S. Tanaka, A. Miyake, T. Kagayama and K. Shimizu, *Philos. Trans. A*.

62 S. G. Ebbinghaus, H. Krause and F. Syrowatka, *Cryst. Growth Des.*, 2013, **13**, 2990–2994.

63 K. Kurashige, Y. Toda, S. Matstuishi, K. Hayashi, M. Hirano and H. Hosono, *Cryst. Growth Des.*, 2006, **6**, 1602–1605.

64 *Am. Ceram. Soc. Natl. Inst. Stand. Technol.*, 2017, **Phase Eq.**, Figure Numbers 12337.

65 Y. Tian, X. Pan, H. Yu and G. Tu, *J. Alloys Compd.*, 2016, **670**, 96–104.

66 M. Ruszak, S. Witkowski, P. Pietrzyk, A. Kotarba and Z. Sojka, *Funct. Mater. Lett.*, 2011, **04**, 183–186.

67 M. M. Rashad, A. G. Mostafa and D. A. Rayan, *J. Mater. Sci. Mater Electron*, 2016, **27**, 2614–2623.

68 S. Matsuishi, T. Nomura, M. Hirano, K. Kodama, S. ichi Shamoto and H. Hosono, *Chem. Mater.*, 2009, **21**, 2589–2591.

69 Y. Inoue, M. Kitano, S.-W. Kim, T. Yokoyama, M. Hara and H. Hosono, *ACS Catal.*, 2014, **4**, 674–680.

70 S. G. Yoon, S. W. Kim, D. H. Yoon, M. Hirano and H. Hosono, *J. Nanosci. Nanotechnol.*, 2009, **9**, 7345–7349.

71 P. Kofstad, *J. Phys. Chem. Solids*, 1962, **23**, 1579–1586.

72 K. T. Jacob and G. Rajitha, *J. Phase Equilibria Diffus.*, 2012, **33**, 293–302.

73 M. M. Ali, M. Nagao, S. Watauchi and I. Tanaka, *ACS Omega*, 2016, **1**, 1157–1163.

74 M. Miyakawa, M. Hirano, T. Kamiya and H. Hosono, *Appl. Phys. Lett.*, , DOI:10.1063/1.2735280.

75 M. Miyakawa, N. Ueda, T. Kamiya, M. Hirano and H. Hosono, *J. Ceram. Soc. Japan*, 2007, **115**, 567–570.

76 S. G. Ebbinghaus, H. Krause, D.-K. Lee and J. Janek, *Cryst. Growth Des.*, 2014, **14**, 2240–2245.

77 P. V Sushko, A. L. Shluger, K. Hayashi, M. Hirano and H. Hosono, *Appl. Phys. Lett.* , , DOI:10.1063/1.1871359.

78 K. Hayashi, *J. Solid State Chem.*, 2011, **184**, 1428–1432.

79 M. I. Bertoni, T. O. Mason, J. E. Medvedeva, A. J. Freeman, K. R. Poeppelmeier and B. Delley, *J. Appl. Phys.*, , DOI:10.1063/1.1899246.

80 Y. Dong, K. Hayashi, H. Nozoe, Y. Shinoda and H. Hosono, *J. Am. Ceram. Soc.*, 2014, **97**, 4037–4044.

81 E. V. Galuskin, F. Gfeller, I. O. Galuskina, T. Armbruster, R. Bailau and V. V. Sharygin, *Eur. J. Mineral.*, 2015, **27**, 99–111.

82 M. Miyakawa, H. Hiramatsu, T. Kamiya, M. Hirano and H. Hosono, *J. Solid State Chem.*, 2010, **183**, 385–391.

83 L. Palacios, S. Bruque and M. a G. Aranda, *Phys. Status Solidi*, 2008, **245**, 666–672.

84 O. Yamaguchi, A. Narai and K. Shimizu, *J. Am. Ceram. Soc.*, 1986, **69**, C36–C37.

85 K. Hayashi, N. Ueda, S. Matsuishi, M. Hirano, T. Kamiya and H. Hosono, *Chem. Mater.*, 2008, **20**, 5987–5996.

86 M. Miyakawa, K. Kobayashi and T. Taniguchi, *J. Am. Ceram. Soc.*, 2017, 1–5.

87 K. Hayashi, P. V Sushko, Y. Hashimoto, A. L. Shluger and H. Hosono, *Nat. Commun.*, 2014, **5**, 3515.

88 M. Teusner, R. A. De Souza, H. Krause, S. G. Ebbinghaus and M. Martin, *Solid State Ionics*, 2016, **284**, 25–27.

89 D. A. Schmidt, Technischen Universitat Berlin, 2014.

90 S. Maurelli, M. Ruszak, S. Witkowski, P. Pietrzyk, M. Chiesa and Z. Sojka, *Phys. Chem. Chem. Phys.*, 2010, **12**, 10933–10941.

91 W. Lv, W. Lü, N. Guo, Y. Jia, Q. Zhao, M. Jiao, B. Shao and H. You, *RSC Adv.*, 2013, **3**, 16034–16039.

92 J. T. S. Irvine and A. R. West, *Solid State Ionics*, 1990, **40**–**41**, 896–899.

93 H. Zhu, Y. Liu, D. Yan, H. Bian, H. Li, C. Liu, C. Xu and X. Wang, *Opt. Mater. (Amst).*, 2014, **36**, 1771–1775.

94 J. Zhang, Z. Zhang, T. Wang and W. Hao, *Mater. Lett.*, 2003, **57**, 4315–4318.

95 R. Wang, Y. Zhang, J. Sun, L. Liu and Y. Xu, *J. Rare Earths*, 2011, **29**, 826–829.

96 Y. X. Liu, L. Ma, D. T. Yan, H. C. Zhu, X. L. Liu, H. Y. Bian, H. Zhang and X. J. Wang, *J. Lumin.*, 2014, **152**, 28–32.

97 D. Wang, Y. Liu, C. Xu, Y. Liu, U. Wang and X. Li, *J. Rare Earths*, 2008, **26**, 433–

438.

98 S.-Y. Liao, R. Yao, X.-Y. Chen, G.-R. Wang and F. Zheng, *Mater. Des.*, 2016, **108**, 93–105.

99 E. Tõldsepp, T. Avarmaa, V. Denks, E. Feldbach, M. Kirm, A. Maaroos, H. Mändar and S. Vielhauer, *Opt. Mater. (Amst).*, 2010, **32**, 784–788.

100 X. Liu, Y. Liu, D. Yan, H. Zhu, C. Liu, W. Liu, C. Xu, Y. Liu, H. Zhang and X. Wang, *Dalt. Trans.*, 2013, **42**, 16311–16317.

101 X. Liu, Y. Liu, D. Yan, M. Zhang, J. Yang, H. Zhu, C. Liu, C. Xu and X. Wang, *Mater. Des.*, 2016, **107**, 139–143.

102 H. Zhu, Y. Liu, D. Yan, X. Yan, C. Liu and C. Xu, *J. Nanosci. Nanotechnol.*, 2011, **11**, 9958–9963.

103 X. Liu, Y. Liu, D. Yan, H. Zhu, C. Liu, C. Xu, Y. Liu and X. Wang, *J. Mater. Chem.*, 2012, **22**, 16839–16843.

104 M. Zhang, Y. Liu, H. Zhu, D. Yan, J. Yang, X. Zhang, C. Liu and C. Xu, *Phys. Chem. Chem. Phys.*, **18**, 18697–18704.

105 S. Liao, R. Yao, Y. Liu, X. Chen, X. Hu and F. Zheng, *J. Alloys Compd.*, 2015, **642**, 7–14.

106 Y.-Q. Mao, Y.-P. Pu and J.-F. Wei, *Mater. Res. Innov.*, 2011, **15**, 260–263.

107 X. Zhang, Y. Liu, M. Zhang, J. Yang, H. Zhu, D. Yan, C. Liu and C. Xu, *Mater. Res. Bull.*, 2017, **86**, 51–56.

108 K. Sato, M. Yamaguchi, S. Fujita, K. Suzuki and T. Mori, *Catal. Commun.*, 2006, **7**, 132–135.

109 S. Iimura, Y. Tomota, S. Matsuishi, R. Masuda, M. Seto, H. Hiraka, K. Ikeda, T. Otomo and H. Hosono, *Inorg. Chem.*, 2017, **56**, 566–572.

110 K. Sato, J. Iritani, R. Miyamoto, S. Fujita, K. Suzuki, M. Ohkawa and T. Mori, *Stud. Surf. Sci. Catal.*, 2005, **158**, 2001–2008.

111 S. Fujita, K. Suzuki and T. Mori, *Catal. Letters*, 2003, **86**, 139–144.

112 B. Y. R. D. Shannon, *Acta Cryst.*, 1976, **A 32**, 751–767.

113 I. Gonzalo-Juan and R. Riedel, *ChemTexts*, 2016, **2**, 6.

114 A. E. Danks, S. R. Hall and Z. Schnepp, *Mater. Horiz.*, 2016, **3**, 91–112.

115 M. Kakihana, *J. Sol-Gel Sci. Technol.*, 1996, **6**, 7–55.

116 P. Pramanik and A. Pathak, *Bull. Mater. Sci.*, 1994, **17**, 967–975.

117 S.-J. Lee, E. a Benson and W. M. Kriven, *J. Am. Ceram. Soc.*, 1999, **82**, 2049–2055.

118 G. V. Reserach, 2017, 76.

119 A. E. Martell and R. M. Smith, *Critical stability constants.*, 1977, vol. 5.

120 G. H. Nancollas and M. B. Tomson, *Pure Appl.Chem*, 1982, **354**, 2675–2692.

121 Y. Narendar and G. L. Messing, *J. Mater. Res.*, 1999, **14**, 3921–3931.

122 E. Herdtweck, T. Kornprobst, R. Sieber, L. Straver and J. Plank, *Zeitschrift für Anorg. und Allg. Chemie*, 2011, **637**, 655–659.

123 P. Karen and A. Kjekshus, *J. Am Ceram. Soc.*, 1994, **77**, 547–52.

124 Y. Narendar and G. L. Messing, *Catal. Today*, 1997, **35**, 247–268.

125 D. Wyrzykowski, E. Hebanowska, G. Nowak-Wiczk, M. Makowski and L. Chmurzyński, *J. Therm. Anal. Calorim.*, 2011, **104**, 731–735.

126 G. Maino, J. D'Haen, F. Mattelaer, C. Detavernier, A. Hardy and M. K. Van Bael, *J. Mater. Chem. A*, 2016, **4**, 18457–18469.

127 A. Hardy, S. Gielis, H. Van den Rul, J. D'Haen, M. K. Van Bael and J. Mullens, *J. Eur. Ceram. Soc.*, 2009, **29**, 3007–3013.

128 M. K. Van Bael, A. Hardy and J. Mullens, in *Chemical Solution Deposition of Functional Oxide Thin Films*, eds. T. Schneller, R. Waser, M. Kosec and D. Payne, Springer Vienna, 2013, pp. 93–140.

129 T. Schneller, R. Waser, M. Kosec and D. Payne, *Chemical Solution Deposition of Functional Oxide Thin Films*, 2013.

130 S. N. Ude, C. J. Rawn, R. A. Peascoe, M. J. Kirkham, G. L. Jones and E. Andrew Payzant, *Ceram. Int.*, 2014, **40**, 1117–1123.

131 W. J. Lee and T. T. Fang, *J. Mater. Sci.*, 1995, **30**, 4349–4354.

132 Z. Haijun, J. Xiaolin, Y. Yongjie, L. Zhanjie, Y. Daoyuan and L. Zhenzhen, *Mater. Res. Bull.*, 2004, **39**, 839–850.

133 A. E. Martell and R. M. Smith, *Other Organic Ligands*, 1977.

134 R. Smith and A. Martell, *Critical Stability Constants Volume 4: Inorganic Complexes*, 1976, vol. 4.

135 B. Martin, *Inorg. Biochem.*, 1986, **28**, 181–187.

136 R. B. Martin, *Clin. Chem.*, 1986, **3210**, 1797–1806.

137 H. E. Swanson and R. K. Fuyat, *Standard X-ray Diffraction Powder Patterns*, National Bureau of Standards, 539 I., 1953.

138 H. E. Swanson, N. T. Gilfrich and G. M. Ugrinic, *Standard X-ray Diffraction Powder Patterns*, National Bureau of Standards, 539 V., 1955.

139 S. Maurelli, M. Ruszak, S. Witkowski, P. Pietrzyk, M. Chiesa and Z. Sojka, *Phys.*

Chem. Chem. Phys., 2010, **12**, 10933–10941.

140 M. A. Gülgün, O. O. Popoola and W. M. Kriven, *J. Am. Ceram. Soc.*, 1994, **77**, 531–539.

141 N. N. Eremin, A. E. Grechanovsky and E. I. Marchenko, *ISSN Crystallogr. Reports*, 2016, **61**, 1063–7745.

142 P. Mondal and A. J. W. Jeffery, *Acta Cryst*, 1975, **B31**, 31–689.

143 R. A. Andrievski, *J. Mater. Sci.*, 2014, **49**, 1449–1460.

144 Y. Dong and I. W. Chen, University of Pennsylvania, 2017.

145 A. K. Burrell, T. M. Mccleskey and Q. Jia, in *Chemical Solution Deposition of Functional Oxide Thin Films*, eds. T. Schneller, R. Waser, M. Kosec and D. Payne, Springer Vienna, 2013, pp. 141–158.

146 M. H. Nguyen, S.-J. Lee and W. M. Kriven, *J. Mater. Res.*, 1999, **14**, 3417–3426.

147 R. V. Kumar, Y. Koltypin, Y. S. Cohen, Y. Cohen, D. Aurbach, O. Palchik, I. Felner and A. Gedanken, *J. Mater. Chem.*, 2000, **10**, 1125–1129.

148 M. Stoia, M. Barbu, M. Ştefanescu, P. Barvinschi and L. Barbu-Tudoran, *J. Therm. Anal. Calorim.*, 2012, **110**, 85–92.

149 F. J. Gotor, J. M. Criado, J. Malek and N. Koga, *J. Phys. Chem. A*, 2000, **104**, 10777–10782.

150 H. E. Kissinger, *J. Res. Natl. Bur. Stand. (1934).*

151 T. Ozawa, *Polymer (Guildf).*, 1971, **12**, 150–158.

152 A. K. Jena and M. C. Chaturvedi, *Phase Transformations in Materials*, Prentice Hall, 1991.

153 E. R. Fotsing, Technische Universitat Clausthal, 2005.

154 A. Khawam and D. R. Flanagan, *J. Phys. Chem. B*, 2006, **110**, 17315–17328.

155 T. Degen, M. Sadki, U. K. E. Bron and G. Nénert, *Powder Diffr.*, 2014, **29**, S13–S18.

156 J. R. Salasin and C. J. Rawn, *Crystals*, 2017, **7**, 1–25.

157 J. R. Salasin and C. J. Rawn, *In-Situ Kinet. Investig. Calcium Aluminate Form.*

158 S. W. Kim and H. Hosono, *Philos. Mag.*, 2012, **92**, 2596–2628.

159 R. D. Shannon and C. T. Prewitt, *Acta Cryst.*, 1969, **B25**, 925–946.

160 D. Jiang, Z. Zhao, S. Mu, V. Phaneuf and J. Tong, *Inorg. Chem.*, 2017, **56**, 11702–11709.

161 K. Khan, A. Khan Tareen, S. Elshahat, A. Yadav, U. Khan, M. Yang, L. Bibbò and Z. Ouyang, *Dalt. Trans.*, 2018, **47**, 3819–3830.

162 B. H. Toby and R. B. Von Dreele, *J. Appl. Crystallogr.*, 2013, **46**, 544–549.

163 H. Boysen, I. Kaiser-Bischoff, M. Lerch, S. Berendts, M. Hoelzel and a. Senyshyn, *Acta Phys. Pol. A*, 2010, **117**, 38–41.

164 M. T. Hernandez, M. González and A. De Pablos, *Acta Mater.*, 2003, **51**, 217–228.

165 P. Barnier, C. Brodhag and F. Thevenot, *J. Mater. Sci.*, 1986, **21**, 2547–2552.

166 E. . Owen and E. . Yates, *Philos. Mag.*, 1933, **Series 7**, 472–488.

167 D. Keffer, A. V. McCormick and H. T. Davis, *J. Phys. Chem.*, 1996, **100**, 967–973.

168 M. W. J. Chase, *J. Phys. Chem. Ref. Data*, 1998, 1–1951.

169 Masterton, Slowinkski and Stanitski, *Chemical Principles*, CBS College Publishing, 1983.

170 O. Trofymluk, Y. Toda, H. Hosono and A. Navrotsky, *Chem. Mater.*, 2005, **17**, 5574–5579.

VITA

Dr. John Robert Salasin was born in Delaware to the parents of John and Roseann Salasin. He is the middle of 5 siblings with two older sisters Terri Gallagher and Beverley Zook and two younger sisters Rian and Devon Salasin. He received his bachelor's degree in physics with a nano-manufacturing concentration from Shippensburg University. Dr. Salasin also completed a certification in nano-manufacturing and fabrication from the Penn State University in 2012. In May of 2018 he graduated with his masters in Materials Science and Engineering. In August of 2018 he graduated with his Ph.D. in Materials Science and Engineering writing a dissertation focused on the synthesis, processing, and characterization of $Ca_{12}Al_{14}O_{33}$.

Dr. Salasin became acquainted with the University of Tennessee Materials Science and Engineering department during the summer of 2013 while participating in a Research Experience for Undergraduates (REU) site funded by the National Science Foundation (NSF) and hosted by the MSE department. The REU site was directed towards projects fitting within the areas related to the synthesis and characterization of advanced functional materials, and Dr. Salasin's research focused on synthesizing layered double hydroxides for magnetic applications. The next summer, Dr. Salasin participated in the Higher Education Research Experience (HERE) at Oak Ridge National Laboratory (ORNL) learning how to collect and analyze low temperature single crystal neutron and x-ray data for determining structural details of thermoelectric materials derived from natural analogs. Data were collected on instruments at the Spallation Neutron Source (SNS) and the High Flux Isotope Reactor (HFIR).

Dr. Salasin's broad research interests include energy materials focusing on synthesis and processing of novel thermoelectrics, battery materials, and anion-exchange media. He actively served as a mentor for some of the Research and Instructional Strategies in Engineering Retention (RISER) program's Undergraduate Research Assistants (URAs) and MSE undergraduate students doing research supported by the Center for Materials Processing (CMP). Dr. Salasin culminated his Ph.D. with three first authors peer reviewed papers which are currently under review as well as a published first author review paper. In addition to his research and mentoring responsibilities, Dr. Salasin operated as the CMP laboratory manager where he designed and implemented a materials process and synthesis laboratory in the Joint Institute for Advance Materials (JIAM). He has also worked to procure, install, and train students on equipment in the CMP processing laboratory.

Dr. Salasin is pursuing a career in industry and has accepted a position at BWX Technologies in Lynchburg, VA.